Non-contact control of a partially submerged monopile subjected to wave loads

An effective magnetic control strategy for monopile during post-upending lowering under wave loads

CIEM0500: Thesis

Federico Raimondi

Delft University of Technology

TU Delft

Non-contact control of a partially submerged monopile subjected to wave loads

An effective magnetic control strategy for monopile during post-upending lowering under wave loads

by

Federico Raimondi

Student number: 6079297

Thesis committee:	Assistant Prof. dr. Peter C. Meijers,	TU Delft, Chair
	Prof. dr. Andrei V. Metrikine,	TU Delft, Supervisor
	Ir. Panagiota Atzampou,	TU Delft, Supervisor
	Assistant Prof. dr. Alessandro Cabboi,	TU Delft, Supervisor

TU Delft

Acknowledgments

This thesis marks the conclusion of my Master's degree in Civil Engineering at TU Delft. The past two years have been a rollercoaster of emotions. Moving to a new country for a new challenge was not easy. At first, the Netherlands felt cold and rainy, but the incredible people I met and the unforgettable moments I experienced here quickly made me feel at home. I am also grateful to the Dutch culture and all my Dutch friends for teaching me to appreciate the small joys we often take for granted, such as a simple bike ride on a sunny day. For all these reasons, I would like to thank everyone who made this journey so special.

First and foremost, I sincerely thank the chair of my committee and my daily supervisor, Dr.ir. Peter Meijers. His lectures first inspired me to choose this thesis topic, and after that he has been a constant presence in my academic journey: from the Wave Load Dynamics course and MDP experience through to this thesis. I am deeply grateful for his availability, guidance, and encouragement throughout the process, as well as for the opportunity to learn from his extensive knowledge on topics I never imagined I would have the skills to include in my work.

My thanks also go to my other supervisor, Ir. Panagiota Atzampou. Her previous work and expertise on magnetic control proved invaluable to my research and to my understanding of the topic. I also owe my gratitude to Prof.dr. Andrei Metrikine, whose expertise and insightful suggestions during our meetings pushed me to think more critically about my results. His lectures on dynamics were among the first to spark my curiosity for this fascinating field. Finally, I would like to thank Dr.ir. Alessandro Cabboi for joining the committee during the final stages of my thesis. It has been a privilege to work with such a knowledgeable and supportive committee, whose feedback and guidance have been invaluable from the very beginning.

I am also grateful to the many friends who shared this journey with me. To all my friends in Delft (including those who came only for Erasmus), thank you for being my family away from home and for standing by me every day. We shared the stress of exam periods but also quite a few beers and adventures as well. A special thanks goes to my friends back in Italy, who have always supported me and made me feel as if I never left whenever I returned home. In particular, I want to thank Katia, my "partner in crime" during these two years, who pushed me to be my best and reminded me daily of the value of hard work in achieving our goals.

Finally, my deepest gratitude goes to my family: my brother, my aunt, my grandparents, and above all my parents. Their love and support have been a constant source of strength, encouraging me through difficult times and celebrating every achievement. A special thanks and hug go to my parents, whose advice and support have guided not only my academic journey but also my personal growth. And finally, to my grandmother, who has been sitting next to me since I was a child, teaching me and helping me become the best version of myself, thank you. Without the unwavering support of all my family, I would not be who I am today, nor would I have reached this milestone.

Federico Raimondi
Delft, September 2025

Summary

In response to the transition toward sustainable energy production, offshore wind farms are increasingly being developed in deeper and more challenging marine environments. This shift necessitates larger and heavier turbine structures. To address these challenges, innovative installation approaches are being explored that aim to enhance efficiency, improve positioning accuracy, and maintain high safety standards.

This thesis explores the development and application of magnetic, non-contact control strategies for monopile installation during offshore wind turbine deployment. In particular, the research focuses on designing an effective control method that utilizes dipoles magnetic forces to regulate the motion of a partially submerged monopile during its lowering phase.

To achieve this, a dynamic model of the crane-monopile system was developed based on a double pendulum configuration. This model incorporated both wave-induced loads and the progressive submersion of the monopile, with hydrodynamic forces calculated using Airy wave theory and Morison's equation. This setup enabled a realistic assessment of how magnetic interaction behaves under typical and realistic environmental and operational conditions.

The system's dynamic behavior was investigated both analytically, where feasible, via eigenvalue analysis, and numerically through time-domain simulations. These analyses considered the combined effects of wave loading and submersion depth on the response of the system. A proportional-derivative (PD) controller was implemented to govern dipole-dipole magnetic interactions, enabling active control of the monopile's motion. The model also accounted for nonlinearities present in magnetic forces and hydrodynamic drag.

Through this control framework, the magnetic moment required to maintain system stability was quantified. However, it became evident that force magnitude alone does not fully determine control effectiveness. Therefore, different design parameters, particularly the horizontal spacing between magnets, their vertical positioning along the monopile and the dipole moments, were systematically evaluated to identify configurations that optimize control performance.

Compared to conventional installation methods, the proposed non-contact magnetic control strategy offers several distinct advantages. It does not depend on mechanical attachment to the monopile or active human intervention, which reduces potential damage and improves operational safety. Furthermore, it enables more precise and distributed control, as magnetic actuators can be placed at multiple locations along the monopile, enhancing the system's ability to counteract dynamic responses.

Overall, this research contributes to the broader understanding of magnetically controlled systems and supports the development of more advanced methods for offshore wind turbine foundation installation.

Contents

List of Figures

List of Tables

1

Introduction

1.1. Research Context

The impact of climate change has led to global efforts to prevent irreversible consequences. Among the steps towards a greener future is the transition from fossil fuels to renewable energy. As one of the most significant contributors to greenhouse gas emissions, the energy sector plays a critical role in climate change mitigation. Therefore, advancement in sustainable energy technologies is of extreme importance [1].

Wind energy has seen significant growth in recent years because of its cost, its energy production efficiency, and the increasing demand for renewable energy sources [2]. Due to more stable wind conditions and the scarcity of onshore locations, wind farms have progressively moved farther offshore [3].

To meet the European shift toward the future sustainable energy goals [4], the offshore wind industry is expanding farther into deeper waters. However, as turbines are placed in these deeper and more hostile marine environments, they require larger, heavier designs, making the installation process more complex and technically demanding [5]. As a result, new installation methods are being studied to improve efficiency, facilitate a more accurate positioning, and ensure higher standards of operational safety.

1.2. Research Problem

Monopiles are the most commonly used support structures for bottom-fixed offshore wind turbines (OWTs). However, there is limited research focused on their installation. Traditionally, monopiles are installed using jack-up vessels; however, the industry has been shifting toward the use of floating heavy-lift vessels (HLVs) which offer greater efficiency and flexibility [6].

During installation, both the vessel and the monopile are subject to external forces from wind and waves, which disturb the system and thus, compromise the installation precision. Therefore, for a correct control during positioning and lowering phase, a prediction of the system's response to these disturbances is essential [7].

The successful deployment of offshore wind turbines depends heavily on the installation stage. External disturbances or unbalanced control forces can induce vibrations and instability, highlighting the importance of a precise and safe control of the monopile during positioning and lowering phase. Currently, fixed and motion compensation gripper frames are the most commonly used control methods for bottom-founded OWT installations [6]. In addition, techniques involving tugger lines, either manually operated or actively controlled, are also employed to stabilize the payload through constant tension [8]. However, tugger lines can only exert attractive forces, limiting their effectiveness in certain dynamic scenarios where repulsive or bidirectional control could be beneficial. Other methods introduce mo-

tion compensation indirectly via crane control strategies, such as motion-compensated platforms [9] or crane parameter optimization [10].

These installation methods rely on either mechanical contact with the monopile or active human intervention [6]. These limitations, combined with the delicate nature of positioning turbine components, have led to research into non-contact magnetic position control techniques for OWTs. Such methods could enhance safety by reducing the risks associated with human intervention and improve the efficiency of the installation process, which is critical for minimizing operational costs [11].

This technique includes at least a fixed permanent magnet, attached to the monopile, and an actively controlled external magnet, positioned theoretically on the vessel and opposite to the permanent one (see Fig.1.1).

A key advantage of magnetic control systems is their ability to apply both attractive and repulsive forces [11]. This bidirectional capability allows for more precise and flexible manipulation of the payload without requiring physical contact.

To assess the feasibility and reliability of the non-contact magnetic control in offshore conditions, the influence of submersion level and wave-induced forces on magnetic control performance during monopile installation must be taken into consideration. These factors can significantly affect the dynamic behavior of the system and may impact the effectiveness of non-contact control strategies [5].

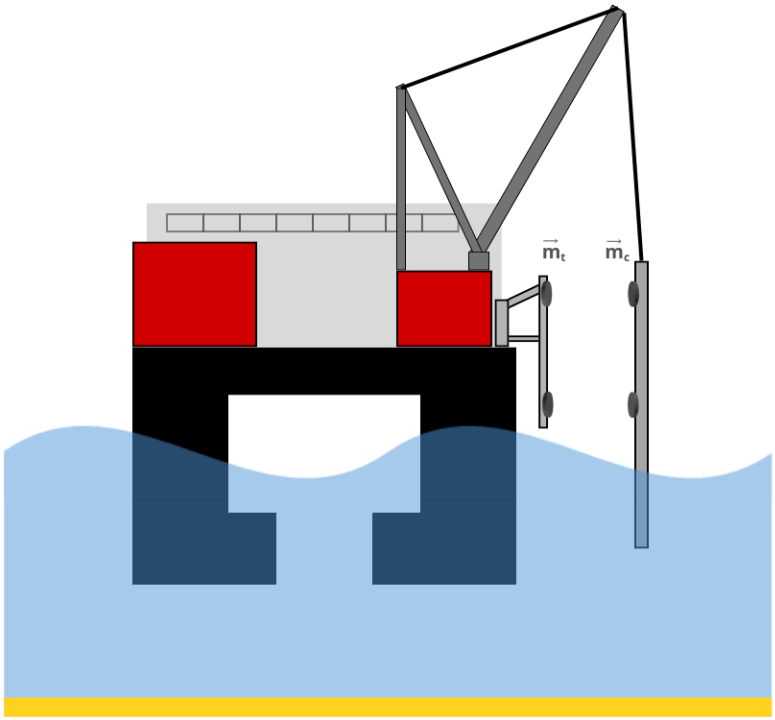

Figure 1.1: Schematic diagram of monopile installation with non-contact control.

1.3. Research Objectives

This research aims to develop an effective non-contact control strategy for a partially submerged monopile during offshore installation using magnetic forces. To achieve this, a dynamic model of the crane–monopile system is constructed, incorporating wave-induced loads and the effect of gradual submersion during the lowering stage. This model will help analyze the behavior of the magnetic interaction throughout different stages of the operation.

A key objective is to determine the submersion depths at which active control becomes most necessary, thereby improving the understanding of how submersion level influences the performance of non-contact control systems. This will be achieved by evaluating the combined effect of wave forces and submersion level on the system dynamics.

Furthermore, the study aims to quantify the magnitude of the magnetic forces of the external magnets required to maintain control throughout the installation. Based on this, the optimal arrangement and positioning of magnets along the monopile will be explored to enable effective and stable control. Overall, this research will contribute to advancing knowledge in the use of magnetic, non-contact control strategies for OWTs installation.

1.4. Research Scope

The scope of this research is limited to the lowering phase of the monopile after upending, and aims to develop a numerical model to predict the system's dynamic response with and without magnetic control. The model represents the system as a simplified planar double pendulum. More specifically, effects from vessel motion, such as tip displacement or lifting hook dynamics, are neglected by assuming a fixed pivot point, thereby focusing on the pendular dynamics of the system.

The model considers wave loading as the dominant disturbance, in line with findings in literature where wave forces account for up to 96% of dynamic effects during offshore wind turbine installation [5]. For this reason, wind and current loads are not included in the present analysis.

Offshore wind turbine farms are located in diverse atmospheric and marine environments worldwide, each presenting unique challenges in terms of environmental loadings. This research will specifically focus on the conditions prevalent in the North Sea, using data [12] from this region to model and analyze the wave-induced loads affecting monopile installation.

Magnetic stabilization is explored through dipole–dipole interaction models, where the external magnetic field is set to control the motion of the submerged monopile.

1.5. Research Theory and Methods

The system is modeled as a planar double pendulum, where the first component is a cable, and the other is a hollow cylinder (the monopile) with small thickness relative to its length. Both bodies are assumed to be rigid. In addition, the equations of motion are derived using Lagrangian mechanics, under a small-angle approximation. A harmonic solution is applied to the linearized system for frequency domain insights, while a numerical solver is used to simulate time-domain responses. Thus, the approach is considered semi-analytical.

For the representation of offshore conditions, linear wave theory is used together with a JONSWAP spectrum to define the characteristics of the irregular sea state. Furthermore, wave loading on the submerged part of the monopile is modeled using the Morison equation, under the assumption of slender-body theory and neglecting diffraction effects. The effects of diffraction would be more relevant for larger monopile diameters.

On the other end, the magnetic control is based on dipole–dipole interactions, assuming that the magnetic dipole moment is aligned with the horizontal axis, such that only the horizontal component of the magnetic force is considered. As illustrated in Fig.1.1 the fixed permanent magnets on the monopile interact horizontally with the actively controlled external magnets on the vessel. The external magnets are modeled as a controllable dipole whose moment is regulated via a Proportional-Derivative (PD) controller. While in practice the magnetic field is generated by an electromagnet with variable current, the model abstracts this behavior without explicitly modeling the current in the electromagnetic coil. This simplification allows the model to neglect the full electromagnetic field theory, while still capturing the key effects of controllable magnetic interaction on the system dynamics.

As mentioned, a Proportional-Derivative (PD) controller regulates the magnetic dipole moment of the external magnet. This approach allows the PD controller to remain linear, as the non-linearity of the magnetic force is handled separately. The Integral component of the controller is omitted, since in

systems with sinusoidal responses, the integral of the error tends to cancel out over time. If a magnetic force of great magnitude is needed, the system can be extended to include multiple magnets, allowing for a superposition of dipole effects.

Due to nonlinearities in both the drag force and magnetic force, the time-domain response requires numerical integration. To reduce computational complexity, linearization may be applied to the drag force, however, linearizing the magnetic force is not ideal. The linearization of the magnetic interaction would be of limited validity and may significantly misrepresent the force's behavior over the system dynamics. Thus, the full non-linear system will be considered.

1.6. Research Questions

Based on the research objectives and scope, the main research question guiding this study is:

What is an efficient non-contact magnetic control strategy of a partially submerged monopile subjected to wave loads?

To address the main research question, the investigation is divided into two key thematic categories: the effect of submersion and the magnetic control. Each category is explored through sub-questions as outlined below:

Submersion Effect

- How does partial submersion affect the dynamic properties of a monopile during installation?
- How does variation in submersion level influence the control of the monopile throughout the installation stage?

Magnetic Control

- What magnitude of magnetic forces is necessary to control the monopile during installation offshore?
- What number and spatial arrangement of magnets ensures a reliable and efficient control performance?

1.7. Report Structure

This thesis is organized into four main chapters, presenting the non-contact control strategy for monopile installation under wave loading, from its theoretical foundations to its development, application, and assessment.

Chapter 2 provides a comprehensive literature review that establishes the theoretical background for this work. It introduces the fundamental principles of pendulum dynamics, irregular wave theory, and the JONSWAP wave spectrum, which together form the basis for analyzing wave-induced loads. Furthermore, one section is dedicated to the application of the Morison Equation for modeling hydrodynamic forces. The chapter also reviews existing approaches to magnetic control in pendulum systems. Finally, it discusses the fundamentals of magnetic dipole–dipole interaction and the principles of Proportional–Derivative (PD) control, both of which are of extreme importance for the proposed non-contact control strategy.

Building on this foundation, Chapter 3 presents the model formulation. It derives the equations of motion for the double pendulum using Lagrange's method and defines the wave characteristics considered in the study. The chapter then describes the integration of the Morison Equation along the submerged length of the monopile, followed by a frequency-domain analysis to investigate the modal properties of the linearized system. A sensitivity analysis is also included to evaluate how variations in system parameters affect the pendulum's behavior and to identify the optimal geometries for the subsequent time-domain analyses, which investigate the dynamic response under Morison-based wave loading.

Once the response of the pendulum is quantified, Chapter 4 addresses the control strategy. First the implementation of the magnetic control system is explained, emphasizing the interaction between the

fixed permanent magnets on the monopile and the actively controlled external magnets on the vessel. Then, the PD control gains, K_p and K_d, are tuned to achieve effective control under a simplified load of similar magnitude, without wave effects, and the performance of single and double magnet configurations is compared under these conditions. Following this, wave loading and submersion effects are introduced, and a parametric study is conducted to assess system performance under varying conditions, including different submersion lengths, magnet positions, and horizontal spacing between magnets.

The concluding chapter summarize the key findings and identifies the most effective control strategy for managing the dynamics of a partially submerged double pendulum under wave loading. It also discusses practical engineering implications and offers recommendations for future work, highlighting opportunities to refine the model and extend the applicability of the control approach in real-world offshore installation operations.

2

Literature Review

2.1. Pendulum Dynamics

The dynamical behavior of a monopile during offshore installation can be approximated using pendulum models. Depending on the desired level of accuracy, the system may be treated as a single, double, or even triple pendulum. Pendulum systems are classical representations of nonlinear dynamics and can exhibit complex behavior ranging from periodic motion to deterministic chaos. In particular, even a single pendulum with a driving force or a double pendulum with a slight perturbation in initial conditions can result in unpredictable, exponentially diverging responses over time.

The equation of motion for a single pendulum of length l and mass m, in the absence of damping and external forcing, is given by:

$$ml^2\ddot{\theta} + mgl\sin(\theta) = 0 \tag{2.1}$$

The motion of the monopile during installation remains relatively small, both in displacement and in rotation due to the large dimensions of the system [13]. For this reason, the chaotic behavior of the pendulum system is not considered in the current research. More in detail, this assumption allows to adopt the small-angle approximation using the Taylor series expansions around the stable equilibrium position of the dynamic system at $\theta = 0$:

$$\sin(\theta) \approx \theta - \frac{\theta^3}{3!} + \frac{\theta^5}{5!} - \cdots \quad \text{and} \quad \cos(\theta) \approx 1 - \frac{\theta^2}{2!} + \frac{\theta^4}{4!} - \cdots \tag{2.2}$$

This linearization of the trigonometric terms, simplifies the equations of motion reducing the system to a linear form that is easier to analyze and integrate numerically.

For angles less than approximately $10^\circ \sim 15^\circ$ (or $0.17 \sim 0.26$ rad), the approximation

$$\sin(\theta) \approx \theta \quad \text{and} \quad \cos(\theta) \approx 1 - \frac{\theta^2}{2} \tag{2.3}$$

is considered sufficiently accurate. The second-order expansion for $\cos(\theta)$ is particularly useful, as it ensures that potential energy terms remain non-constant in the linearized system. It is worth noting, however, that the small-angle approximation becomes increasingly inaccurate for larger oscillations, where higher-order terms may need to be retained to preserve physical realism.

Applying the small-angle approximation to the single pendulum, results in:

$$\ddot{\theta} + \omega^2 \theta = 0, \quad \text{where} \quad \omega = \sqrt{\frac{g}{l}}. \tag{2.4}$$

This equation of motion describes a simple harmonic oscillator with angular frequency ω. The solution leads to elliptical phase portraits, indicating conservation of mechanical energy and periodic motion [14]. In the research by Atzampou et al. [11], a single pendulum is adopted as the dynamical model. In their experimental setup, an aluminum rod simulates the crane cable, and the suspended load, representing the monopile, is modeled as a solid aluminium cube.

More complex dynamics are captured using a double pendulum model, which adds an additional degree of freedom by introducing an interaction between the crane cable and the monopile. In the current research, the system is treated as a double pendulum, allowing for a more realistic representation of the suspended monopile, which is modeled as a hollow cylinder rather than a point mass.

A more elaborate configuration is presented in the work of Domingos et al. [5], where a triple pendulum is used to simulate a crane–load–tugger system. In their research, the model includes the crane cable, a block hook, and a sling rope that connects to the suspended monopile. The monopile itself is represented as a cylinder of uniform diameter. The block hook is modeled as a point mass at the end of a pendulum, and is connected to the monopile by a rigid rod. This forms a triple pendulum system that Domingos et al. [5] study in two planes. However, to reduce complexity, the current research restrict motion to a planar motion.

The present study focuses on the rotational dynamics of the system, assuming all components to behave as rigid bodies. This assumption is justified by the fact that the dimensions and stiffness of the monopile are large compared to the expected loads during installation. As a result, structural deformation is negligible, and the primary interest lies in capturing angular displacements rather than elastic deflections. The rigid body approximation not only simplifies the equations of motion but also enables an efficient preliminary analysis for control.

In addition to the gravitational restoring force, the system dynamics are influenced by external wave loading (see Chapter 2.2) and magnetic forces (see Chapter 2.3), which introduce significant nonlinearities. The wave-induced forces alter the free vibration characteristics through added mass on the submerged portion of the monopile and introduce natural damping via the hydrodynamic drag. Simultaneously, the magnetic interaction, which depends nonlinearly on the distance between dipoles, adds further complexity and potential instability. These effects can lead to phenomena such as mode shape coupling, where vibrational modes interact due to geometric or force-field nonlinearities, as well as chaotic behavior, even though small angle approximation is applied.

Thus, adopting a double pendulum model provides a good compromise between capturing the essential physics of the system and maintaining analytical simplicity, making it suitable for early-stage control investigations.

2.2. Wave Load on Cylinder

To accurately describe and model the installation procedure of a monopile with non-contact control offshore, the equation of motions have to be extended to include various loading conditions and constraints. These include the effects of wave loading, hydrodynamic effects and the varying level of submersion of the monopile during installation.

Wave characteristics and wave-structure interaction are modeled using Morison's equation [15, 16], applied together with linear wave theory [16] and the JONSWAP [17] spectrum to represent realistic sea states.

The resulting distributed hydrodynamic loads are integrated over the surface of the cylinder to predict its dynamic behavior at different submersion levels [15]. It is important to mention that vertical hydrodynamic forces can be omitted due to the monopile's thin walls [18].

2.2.1. Linear Irregular Waves

In this research, linear irregular wave theory is employed to determine the wave kinematics that describe the wave loading on the system. Unlike regular waves, which are described by a single frequency and amplitude, irregular waves capture the natural variability of ocean surface conditions by modeling the sea state as a superposition of multiple linear sinusoidal wave components (harmonics). This approach allows for a more realistic and comprehensive representation of complex sea states, where multiple wave frequencies interact simultaneously [15].

This theory is rooted in Airy wave theory, also known as linear wave theory, and therefore inherits its assumptions and limitations. Specifically, linear irregular wave theory assumes a linear relationship between wave-induced particle kinematics and the wave surface elevation. This assumption is valid for waves with small steepness ($H/\lambda \ll 1$, where H is the wave height and λ is the wavelength). As such, the theory is well-suited for deep water and moderate sea conditions.

The wave kinematics are derived from the potential flow theory, which assumes inviscid, incompressible, and irrotational flow. In this context, the velocity field is derived from a scalar potential function Φ, where the velocity components in any direction are the spatial derivatives of this potential.

Applying the Cauchy-Poisson boundary condition at the free surface and the governing Laplace equation for the velocity potential, a key relation in linear wave theory is obtained: the dispersion relation. This equation links the wave angular frequency ω to the wave number k and water depth d:

$$\omega^2 = gk \tanh(kd) \tag{2.5}$$

Since the equation is implicit in k, it must be solved numerically for a given frequency and depth.

For a single regular wave component with free surface elevation in the following form:

$$\zeta(z,t) = \zeta_a \cos(kz - \omega t) \ , \tag{2.6}$$

the horizontal particle velocity at depth z and time t is given by:

$$u(z,t) = \zeta_a \omega \frac{\cosh(k(d+z))}{\sinh(kd)} \cos(kx - \omega t) \tag{2.7}$$

where ζ_a is the wave amplitude. The angular frequency is defined as $\omega = 2\pi/T$, and k denotes the wave number. The total water depth is given by d, while the vertical coordinate z is defined as positive upward from the still water level. The horizontal coordinate x corresponds to the location of the cylinder and, in this study, it is chosen such that it corresponds with its central axis ($x = 0$) as shown in Fig.2.1.

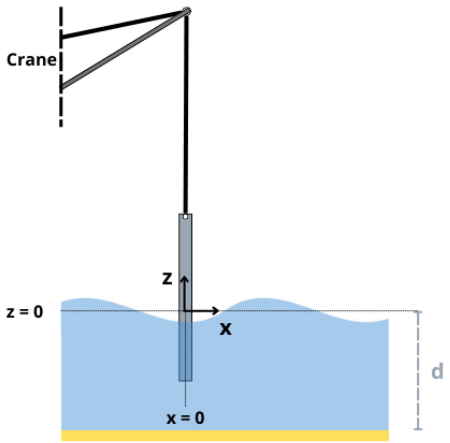

Figure 2.1: Schematic diagram of monopile installation coordinates.

In the case of irregular waves, by breaking down the sea surface into a spectrum of linear harmonics and applying the principles of linear wave theory, the particle velocities and accelerations at any point in the water column can be obtained by summing the contributions of all wave components. Therefore, the surface elevation is represented as a sum of N harmonic components:

$$\zeta(t) = \sum_{n=0}^{N-1} A_n \cos(\omega_n t + \phi_n) \tag{2.8}$$

Each component is characterized by its amplitude, frequency, and phase. The amplitude of the n-th component is given by

$$A_n = \sqrt{2S_{xx}(f_n)\Delta f} \tag{2.9}$$

where $S_{xx}(f_n)$ is the wave energy spectrum at frequency f_n, and Δf is the frequency interval between components. The corresponding angular frequency is $\omega_n = 2\pi f_n$, and the phase angle ϕ_n is randomly chosen, typically following a uniform distribution over the interval $[0, 2\pi]$.

To accurately describe the particle kinematics induced by such an irregular sea state, each wave component must be treated separately. The horizontal particle velocity at depth z is then given by the superposition of the velocities associated with each harmonic:

$$u(z,t) = \sum_{n=0}^{N-1} A_n \omega_n \frac{\cosh(k_n(d+z))}{\sinh(k_n d)} \cos(\omega_n t + \phi_n) = \sum_{n=0}^{N-1} \zeta_n(t)\omega_n \frac{\cosh(k_n(d+z))}{\sinh(k_n d)} \tag{2.10}$$

where k_n is the wave number corresponding to the frequency f_n and $\zeta_n(t)$ represents the surface elevation component of the n-th wave.

$$\zeta_n(t) = A_n \cos(\omega_n t + \phi_n) \tag{2.11}$$

2.2.2. JONSWAP Spectrum

For the analysis of wave-induced loads, it is important to define a representative wave spectrum. This spectrum is essential for identifying the frequency content of the sea state and understanding the possible associated loading conditions. In particular, the spectrum describes how the wave energy is distributed over frequencies, allowing the estimation of wave kinematics (see Chapter 2.2.1) and resulting hydrodynamic forces (see Chapter 2.2.3).

Considering the study conducted by Hasselmann et al. [17], which is based on wave data from the North Sea, region with a high concentration of offshore wind farms, the most suitable spectrum for this analysis is the JONSWAP spectrum (Joint North Sea Wave Project). This spectrum is specifically designed for fetch-limited seas like the North Sea, where waves are still developing and are affected by: variable wind conditions, finite fetch (distance over which the wind blows), shallow to intermediate water depths.

The JONSWAP spectral density function $S(f)$ describes the energy distribution of waves over frequency f as follows:

$$S_{\text{JONSWAP}}(f) = \alpha g^2 (2\pi)^{-4} f^{-5} \exp\left[-\frac{5}{4}\left(\frac{f}{f_p}\right)^{-4}\right] \gamma^{\exp\left[-\frac{1}{2}\left(\frac{f/f_p - 1}{\sigma}\right)^2\right]} \tag{2.12}$$

In the formula, f denotes the wave frequency, and $f_p = \frac{1}{T_p}$ is the peak frequency corresponding to the most energetic waves. The gravitational acceleration is represented by g, while $\alpha = 0.076\tilde{F}^{-0.22}$ is the

Phillips constant, which serves as the energy scale parameter. The peak enhancement factor is given by $\gamma = 3.3$. The spectral width parameter, σ, is defined conditionally as:

$$\sigma = \begin{cases} 0.07 & \text{if } f \leq f_p \\ 0.09 & \text{if } f > f_p \end{cases}$$

To compute the spectrum, several parameters derived from wind and fetch conditions are required. These include non-dimensional forms of peak frequency $\tilde{f}_p$ and fetch $\tilde{F}$ used to relate wind speed U, fetch length F, and peak frequency f_p:

$$\tilde{f}_p = \frac{U_{10} f_p}{g}, \qquad \tilde{F} = \frac{gF}{U_{10}^2}$$

According to empirical JONSWAP relationships:

$$\tilde{f}_p = 3.5 \tilde{F}^{-0.33} \quad \Longrightarrow \quad \frac{U_{10} f_p}{g} = 3.5 \left(\frac{gF}{U_{10}^2} \right)^{-0.33}$$

From this relationship, one can determine either the peak frequency (f_p) from the wind speed at 10 meters height (U_{10}), or vice versa.

Solving for f_p		Solving for U_{10}	
$f_p = \dfrac{3.5g}{(gFU_{10})^{1/3}}$	(2.13)	$U_{10} = \dfrac{3.5^3 g^2}{F f_p^3}$	(2.14)

Once the wave spectrum is defined, the irregular wave surface elevation can be reconstructed using linear irregular wave theory through Equation 2.8. The corresponding wave kinematics, in particular the horizontal particle velocity at a given depth z and time t, can then be obtained using Equation 2.10. This velocity is essential for computing the wave-induced force on the structure (see Chapter 2.2.3)

2.2.3. Morison Equation

A possible approach to extend our 2-DoF system to account for fluid-structure interaction and wave loading effects is to use Morison's equation.

The application of Morison's equation relies on several key assumptions. First, the monopile is considered a slender cylinder, with a diameter-to-wavelength ratio:

$$\frac{D}{\lambda} < 0.2 \, . \tag{2.15}$$

Additionally, the wave kinematics are assumed to be uniform around the circumference at each unit length of the cylinder. Finally, the hydrodynamic forces are considered to act perpendicular to the axis of the cylinder.

The first assumption ensures that the cylinder does not significantly alter the incident wave pattern. The second allows us to consider the cylinder's central axis ($x = 0$) for load calculations. Finally, the third assumption confirms that only horizontal wave kinematics are relevant in the force analysis.

Morison's equation as presented in Morison et al. [19] has two force components:

- A linear inertia force, derived from potential flow theory and applicable to oscillatory flows.

$$f_I = \frac{1}{4}\pi D^2 \rho_w \dot{u} + \frac{1}{4}\pi D^2 C_a \rho_w (\dot{u} - \ddot{x}) \tag{2.16}$$

- A quadratic drag force, based on real flow effects and influenced by constant currents.

$$f_D = \frac{1}{2} D C_D \rho_w (u - \dot{x}) |u - \dot{x}| \tag{2.17}$$

The Morison force $f_m(t, z)$ is the summation of the two aforementioned expressions:

$$f_m(t,z) = f_I(t,z) + f_D(t,z) = \frac{1}{4}\pi D^2 \rho_w \dot{u} + \frac{1}{4}\pi D^2 C_a \rho_w (\dot{u} - \ddot{x}) + \frac{1}{2} D C_D \rho_w (u - \dot{x}) |u - \dot{x}| \tag{2.18}$$

From the equation above, it is evident that the force depends on two key variables:

- The fluid flow, represented by the horizontal particle velocity u and the corresponding horizontal particle acceleration $\dot{u}$.
- The structural motion, represented by the first and second derivatives of the displacement x (i.e., velocity $\dot{x}$ and acceleration $\ddot{x}$).

Meanwhile, the remaining terms in the equation are physical and empirical constants that characterize the interaction between the structure and the surrounding fluid. The parameter D represents the diameter of the cylindrical structure, while ρ_w denotes the density of seawater. The coefficient C_a accounts for the added mass effect, which reflects the inertia of the fluid that moves with the structure. Lastly, C_D is the drag coefficient, representing viscous effects and flow separation around the structure, which contribute to the total hydrodynamic resistance.

The superposition of the u and $\dot{x}$ components allows us to analyze not only the effects of the fluid flow on the structure but also the coupled interaction between the fluid flow and the oscillatory motion of the monopile. This is particularly relevant when the monopile is submerged but not fixed to the seabed, as its oscillations influence the overall force response [15].

As detailed by Journée and Massie [16], each term is further explained to understand its contribution to the total hydrodynamic force.

Inertia Component

The inertial forces acting on a cylinder in a fluid can be studied using potential flow theory. This analysis reveals that the total inertia force is composed of two main components:

- Froude-Krylov force: the force exerted on the body due to the undisturbed incident flow.
- Disturbance force: the force resulting from the disturbance of the flow field caused by the presence of the body.

The Froude-Krylov force arises from the horizontal pressure gradient in the flow. It can be considered the force generated by the mass of water displaced by the presence of the cylinder with the current acceleration of undisturbed flow.

$$f_{FK} = \frac{1}{4}\pi D^2 \rho_w \dot{u} \tag{2.19}$$

Furthermore, the Disturbance force takes into account the disturbance of the flow due to the inserted cylinder. Thus, the monopile generates a force to separate the flow leading to the change of the local velocities and accelerations. The disturbed flow pattern is taken into account by using the coefficient of added mass C_a. It can be described as the additional force required to accelerate an object in a fluid due to the fluid's resistance to being displaced.

According to the findings presented by Li, Gao, and Moan [18], the hydrodynamic behavior of hollow cylindrical monopiles is affected by the presence of water both inside and outside the structure. Due to their open-bottom geometry, water enters the interior of the monopile, which alters the resulting hydrodynamic forcing. To accurately compute the distributed forces and moments, this internal water

interaction must be considered using strip theory [20]. Their study further shows that as the monopile is gradually submerged, its interaction with the surrounding fluid changes, making it necessary to determine updated hydrodynamic coefficients. In particular, the 2D added mass coefficient C_a is observed to stabilize at an asymptotic value of approximately 1.8 once the submergence exceeds 5 meters. This stabilized value will be adopted for all depths in the current study.

$$f_{Dist} = \frac{1}{4}\pi D^2 C_a \rho_w (\dot{u} - \ddot{x}) \quad \text{where} \quad C_a = 1.8 \tag{2.20}$$

The two terms together give Equation 2.16

Drag Component

Potential flow theory neglects the effects of viscosity, which is an important contributor to drag forces in real fluid flow. Drag is generally composed of two main components:

- Friction drag - caused by shear stresses that develop along the surface of the cylinder due to the fluid's viscosity.
- Pressure drag - arises when the Reynolds number Re increases, leading to flow separation and a pressure difference between the front and rear of the body.

Given a constant current it can be shown experimentally that the drag force is proportional to the diameter of the cylinder taken into consideration and the quadratic of the current U^2 [15]. In a time dependent flow, the current can be replaced by the particle wave velocity as $u(t)|u(t)|$ which guarantee that the force is always in the same direction of the velocity in the oscillating flow. The above term can be adjusted to consider also the relative motion between the structure and the flow resulting in the expression for the drag force presented in Equation 2.17.

The coefficient C_D is known as drag coefficient and varies for every different configurations of the system. Similarly to the added mass coefficient C_a, for a hollow cylinder it can be calculated experimentally. Studies shows that for this shape, a coefficient with a value between $0.6 - 0.7$ can be chosen [15][18]. These values represent a smooth surface with the possibility of marine growth that would effect the roughness of the cylinder. For the model taken into consideration in the research, the smooth surface is chosen resulting in $C_D = 0.6$.

2.3. Non-Contact Magnetic Control

A promising approach to control a monopile during the installation stage involves a contactless method using magnetic fields.

Since the system can be generalized as a pendulum, this section also provides an overview of the state-of-the-art in magnetic interaction and control techniques applied to such systems.

The equations of motion can be extended to incorporate the control forces by introducing a moment term arising from magnetic interactions, which is highly dependent on the distance between the magnets and the field strength they generate. Specifically, control is implemented using a Proportional-Derivative (PD) controller, which adjusts the moment of one of the magnets to achieve desired motion during installation.

2.3.1. Magnetic Interaction and Control of Pendulum

The study of pendulum systems influenced by magnetic fields is documented in literature mainly in two key contexts: magnetic interaction and magnetic control. These concepts, while related, differ in objective and mechanism, and it's important to distinguish between them.

Magnetic interaction has been widely investigated due to its potential for real-world applications such as energy harvesting and vibration damping in engineering systems. The interaction can be either:

- Ferromagnetic, where a permanent magnet interacts with a material capable of being magnetized (e.g. steel)

- Magnetic, where both interacting bodies can be ideal dipoles or real magnets.

In the energy harvesting context, configurations such as a repulsive magnet pair have been used to increase power extraction [21]. Similarly, magnetic pendulum systems have been proposed as vibration dampers in offshore engineering to mitigate wave-induced motions [22]. Various magnetic configurations have been explored, including vertically aligned magnets beneath the pendulum or horizontally opposed magnets. Mann [23] proposed a nonlinear dynamics study with a ferromagnetic pendulum interacting with both a permanent magnet and an electromagnet on the pendulum.

In the present research, the magnetic interaction is modeled using one or more pairs of horizontally aligned and parallel dipoles: a fixed magnet $\vec{m}_c$ attached to the monopile, and one movable guiding magnet $\vec{m}_t$ used to control a submerged body during offshore installation (see Fig. 1.1).

Magnetic control involves actively regulating the pendulum's motion via externally modulated magnetic fields. This approach is less explored and is mostly experimental. Austin and Wagner [24] implements control by toggling electromagnetic fields to sustain or modify the pendulum's oscillation.

Another experimental technique proposed by Ida [25] uses a pulsing coil to generate a repulsive magnetic field with a current-driven coil acting on a permanent magnet at the pendulum's base.

The work by Atzampou et al. [11] presents a more refined contactless control technique, using a time-varying electromagnet to generate both attractive and repulsive forces. The single-pendulum setup achieves precise control by exploiting the relationship between current, voltage, and the generated magnetic field, taking into account self-inductance. A PD controller is employed to minimize the position error of the pendulum mass.

Inspired by this methodology, the current research numerically investigates a two DoFs system under realistic wave loading conditions (see Chapter 2.2). This study introduces a more detailed and realistic submerged geometry and simplifies the control strategy by omitting a detailed electromagnetic modeling, focusing instead on the system's overall dynamic control performance during monopile installation.

2.3.2. Dipole-Dipole Magnetic Interaction

An external control excitation is applied to the pendulum system through the interaction between the two magnets ($\vec{m}_c$) and ($\vec{m}_t$). These magnets are modeled as ideal magnetic dipoles, a fundamental assumption that allows for a simple but effective description of their behavior.

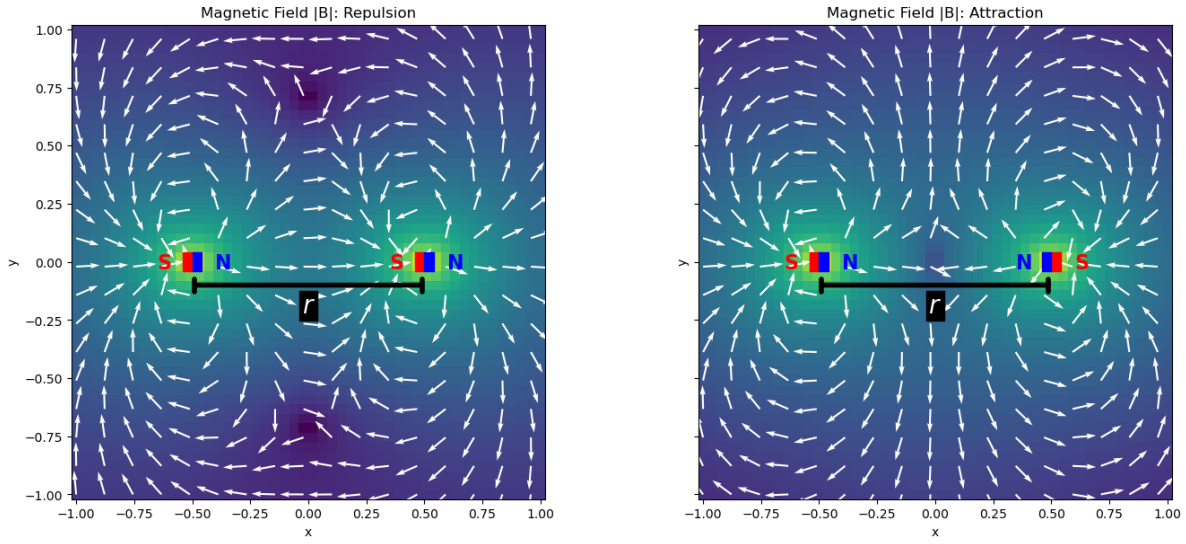

Figure 2.2: Dipole-dipole magnetic field attractive and repulsive interaction.

The dipole-dipole interaction produces a magnetic moment that depends on the relative orientation of the dipole moments and the distance separating them. The movable magnet's polarity can be reversed

in real time by a controller (see Chapter 2.3.3), enabling the system to alternate between attraction and repulsion depending on the desired control strategy. The resulting moment acts as an external excitation moment, designed to counteract the moment generated by the wave loading on the monopile.

The magnetic field $\vec{B}_t$ at the position of the control magnet $\vec{m}_c$, created by the target dipole $\vec{m}_t$, can be computed using the magnetic dipole-dipole interaction formula presented in Equation 2.21 [26].

$$\vec{B}_t(\vec{r}) = \frac{\mu_0}{4\pi} \nabla \left(\frac{\vec{m}_t \cdot \vec{r}}{r^3} \right) = \frac{\mu_0}{4\pi r^3} \left[3(m_t \cdot \hat{r})\hat{r} - m_t \right] \tag{2.21}$$

In the equation, $\mu_0 = 4\pi \times 10^{-7} \, \frac{\mathrm{T \cdot m}}{\mathrm{A}}$ is the magnetic permeability of free space. The vector $\vec{m}_t$ represents the magnetic moment of the target (or fixed) dipole, and $\vec{r}$ is the displacement vector pointing from the target dipole to the control dipole. Its magnitude is given by $r = |\vec{r}|$, and the corresponding unit vector is $\hat{r} = \vec{r}/r$, which indicates the direction of $\vec{r}$. The notation $\vec{m}_t$ refers to the full vector quantity, while m_t denotes its magnitude. The symbol ∇, known as the gradient operator, is defined as $\nabla = \left(\frac{\partial}{\partial x}, \frac{\partial}{\partial y}, \frac{\partial}{\partial z} \right)$. When applied to a scalar field, as in this case, it returns a vector field. The vector fields corresponding to the attractive and repulsive interactions between two dipoles are illustrated in Fig. 2.2.

The potential energy of the control dipole $\vec{m}_c$ in the field $\vec{B}_t$ is given by Equation 2.22.

$$W_m = -\vec{m}_c \cdot \vec{B}_t \tag{2.22}$$

Assuming small angular displacements and planar motion confined to the vertical plane, the system can be simplified by aligning the magnetic dipole moments along the horizontal x-axis. Under this assumption, the magnetic field generated by the target dipole reduces to its horizontal component $B_{t,x}$, as expressed in Equation 2.23. Similarly, the dipole moments $\vec{m}_t$ and $\vec{m}_c$ reduce to their x-components $m_{t,x}$ and $m_{c,x}$, respectively. This leads to a scalar expression for the magnetic potential energy, as shown in Equation 2.24. It is important to mention that the distance r between the dipoles depends on the generalized coordinate vector $\vec{q}$. The vector $\vec{q}$ is introduced in Chapter 3.1.2, while its relationship with r is detailed in Chapter 4.1.

$$B_{t,x} = \frac{\mu_0}{4\pi \cdot r(\vec{q})^3} \left[3m_{t,x} - m_{t,x} \right] = \frac{\mu_0}{4\pi \cdot r(\vec{q})^3} \cdot 2m_{t,x} \tag{2.23}$$

$$W_m = -m_{c,x} B_{t,x} = -\frac{\mu_0}{4\pi \cdot r(\vec{q})^3} \cdot 2m_{c,x} m_{t,x} \tag{2.24}$$

To compute the magnetic moment acting on the pendulum, we differentiate the magnetic potential energy with respect to the components of the generalized vector, as shown in Equation 2.25.

$$M_m = -\frac{\partial W_m}{\partial \vec{q}} \tag{2.25}$$

If multiple magnetic dipoles couples are used, the resulting magnetic field at each control magnet is obtained by superposing the individual contributions from each fixed magnet. The superposition principle holds since the magnetic field is a linear quantity in an ideal environment [27]. In this research, all magnets controlled by the generated field ($\vec{m}_c$) are positioned exclusively along the monopile structure, while the external dipoles ($\vec{m}_t$) are allowed to move but remains always above the water level.

2.3.3. Control Strategy

The objective of the control system is to stabilize the motion of the monopile during installation after upending, by counteracting wave-induced motions using magnetic force. For this purpose, a PID controller (Proportional-Integral-Derivative) is employed, as it is widely used in control applications due to its simplicity and effectiveness as a closed-loop, error-based control algorithm [28].

The controller is defined in the time domain by the following equation:

$$c(t) = K_p e(t) + K_i \int e(t)\, dt + K_d \dot{e}(t) \tag{2.26}$$

where $c(t)$ is the control variable, $e(t) = \xi(t) - x(t)$ is the error between the desired position $\xi(t)$ and the measured position $x(t)$, and K_p, K_i, and K_d are respectively the proportional, integral, and derivative gains.

The proportional gain K_p responds to the current error and plays a key role in adjusting the system's stiffness and reducing settling time. The integral gain K_i, by accounting for the accumulation of past errors, helps eliminate any persistent steady-state offset. Meanwhile, the derivative gain K_d anticipates future behavior by considering the rate of change of the error, enhancing damping and improving the system's transient response [29].

In practice, these gains must be carefully tuned, often through trial and error, to achieve stable and responsive control under varying initial conditions and external forces. In particular, the main study addressing contactless pendulum control employs a PD control approach [11], where the integral term K_i is considered negligible because its contribution tends to cancel out over time due to oscillatory behavior.

In the present application, the magnetic moment of the dipole magnet is chosen as the control variable ($m_{t,x} = c(t)$). Through the feedback loop (see Fig.2.3), this control input is adjusted in real time to minimize the positional error and ensure effective stabilization of the monopile.

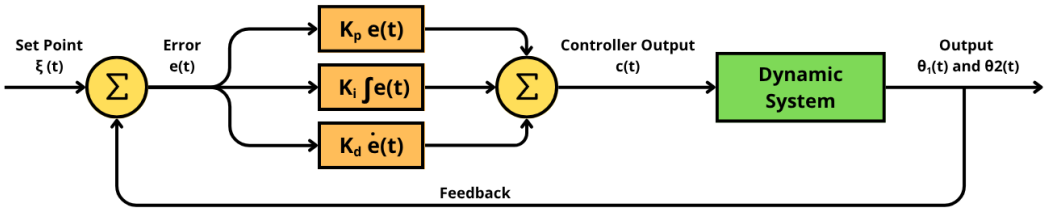

Figure 2.3: PID controller feedback loop.

3

Modeling of Partially Submerged Monopile

3.1. Double Pendulum Model Formulation

Before studying the effect of wave load and develop a control technique, the equation of motion of the system must be derived to describe the free vibration of the system. As presented in the literature review, the crane-load system that characterize the installation of a monopile can be simplified as a pendulum. Specifically, this research describes the system as a double pendulum (see Fig.3.1).

The double pendulum consists of two bodies: a cable of mass m and a hollow cylinder of mass M, representing a monopile of constant diameter. More specifically, the cable is modeled as a rigid rod, while the monopile as a rigid thin shell cylinder. The system can be described with two degrees of freedom: θ_1 and θ_2. These DoFs correspond to the angles of rotation with respect to the z axis of the system. In this study, the system is studied in plane in the z-x axis system.

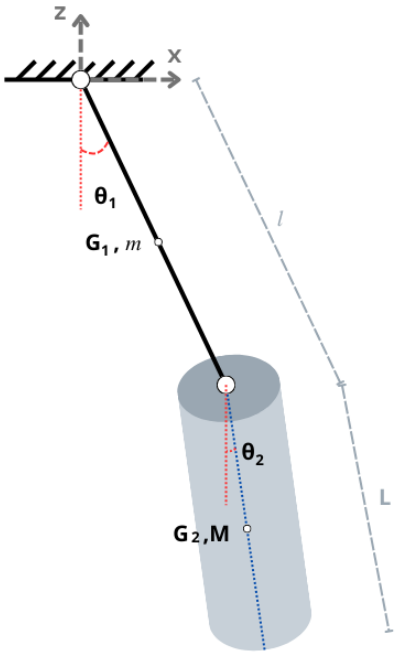

Figure 3.1: Simplified scheme of an upended monopile modeled as a double pendulum

The equation of motion of a simple pendulum (see Equation 2.1) is no longer sufficient to describe the system. With two DoFs, two equations of motion are inherently required. Additionally, the interaction between the two bodies introduces coupling between these equations. To derive them accurately, the system's energy expressions are formulated, and Lagrangian mechanics is applied.

The coordinates that describe the motion of the pendulum are given in terms of the two moving components taken at their respective center of mass:

$$\vec{P}_m = \begin{bmatrix} \frac{l}{2}\sin(\theta_1) \\ -\frac{l}{2}\cos(\theta_1) \end{bmatrix}, \qquad \vec{P}_M = \begin{bmatrix} \frac{L}{2}\sin(\theta_2) + l\sin(\theta_1) \\ -\frac{L}{2}\cos(\theta_2) - l\cos(\theta_1) \end{bmatrix}. \tag{3.1}$$

$\vec{P}_m$ and $\vec{P}_M$ are respectively the position vector of the cable at G_1 and of the monopile at G_2 (see Fig. 3.1).

Another important property of the two rigid bodies is their moment of inertia about the z axis, denoted in this work as I_{CM}. For planar rigid dynamics, this is the only relevant component. The I_{CM} at the center of mass (CM) of the cable and cylinder are:

$$I_{CM,m} = \frac{ml^2}{12} \tag{3.2.a}$$

$$I_{CM,M} = \frac{MR^2}{2} + \frac{ML^2}{12} \tag{3.2.b}$$

In formulating the kinetic energy equations of the system (see Chapter 3.1.1), it is advantageous to exploit the fact that the first body undergoes purely rotational motion about its center of instantaneous rotation (CIR). This point generally does not coincide with its CM.

The Huygens-Steiner theorem allows to determine I_{CIR} at the CIR of a system using Equation 3.1 where M is the mass of the body considered while d is the distance between CM and CIR.

$$I_{CIR} = I_{\text{CM}} + Md^2 \tag{3.3}$$

The CIR of the cable is located at the top of the body. This leads to the following expression for the moment of inertia:

$$I_{CIR,m} = I_{CM,m} + \frac{ml^2}{4} = \frac{ml^2}{3} \tag{3.4}$$

On the other hand, for the cylinder it is best to express the kinetic energy using the center of mass inertia, since the motion of this body includes both rotation and translation. Moreover, due to the complexity of the system, the CIR of the second body does not necessarily coincide with the top of the cylinder, making it less practical in this case to use the Huygens-Steiner theorem.

3.1.1. Energy Formulation

Given the position vectors of the two rigid bodies and their mass moment of inertia, the kinetic energy T and the potential energy U of the dynamical system can be defined as:

$$T = \frac{1}{2}mv_g^2 + \frac{1}{2}I_{CM}\,\omega^2\,, \tag{3.5}$$

$$U = mgh\,. \tag{3.6}$$

Here, m denotes the mass of the rigid body, while v_g represents the velocity of its center of mass. The term I_{CM} refers to the moment of inertia about the z-axis calculated at the center of mass, and ω is the angular velocity of the rigid body. The symbol g refers to the acceleration of gravity, taken as $9.81\frac{\mathrm{m}}{\mathrm{s}^2}$, and h denotes the vertical displacement of the mass m from its equilibrium position.

Note that for planar rigid body motion:

$$\omega = \dot{\theta} \, . \tag{3.7}$$

The total kinetic and potential energy of the double pendulum system are obtained by superimposing the individual contributions from each body:

$$T = T_{\mathsf{rod}} + T_{\mathsf{cyl}} \tag{3.8}$$

$$U = U_{rod} + U_{cyl} \tag{3.9}$$

where:

$$T_{rod} = \frac{1}{2} m v_m^2 + \frac{1}{2} I_{CM_m} \omega_1^2 = \frac{1}{2} I_{CIR_m} \omega_1^2 \tag{3.10.a}$$

$$T_{cyl} = \frac{1}{2} M v_M^2 + \frac{1}{2} I_{CM_M} \omega_2^2 \tag{3.10.b}$$

$$U_{rod} = mg\, P_{m,z} \tag{3.11.a}$$

$$U_{cyl} = Mg\, P_{M,z} \tag{3.11.b}$$

From the moving vectors, it is possible to retrieve the velocity of the center of mass and the vertical component P_z of the cable and of the cylinder, respectively at G_1 and G_2.

$$v_{G_1}(t) = \begin{bmatrix} \dot{\theta}_1 \frac{l}{2} \cos(\theta_1) \\ \dot{\theta}_1 \frac{l}{2} \sin(\theta_1) \end{bmatrix} \, , \qquad v_{G_2}(t) = \begin{bmatrix} \dot{\theta}_2 \frac{L}{2} \cos(\theta_2) + \dot{\theta}_1 l \cos(\theta_1) \\ \dot{\theta}_2 \frac{L}{2} \sin(\theta_2) + \dot{\theta}_1 l \sin(\theta_1) \end{bmatrix} \, . \tag{3.12}$$

$$P_{m,z} = -\frac{l}{2} \cos(\theta_1) \, , \qquad P_{M,z} = -\frac{L}{2} \cos(\theta_2) - l \cos(\theta_1) \, . \tag{3.13}$$

The total kinetic energy of the system T is derived using Equations 3.10 and 3.12, while the total potential energy U is obtained from Equations 3.11 and 3.13. For the complete derivation of Equations 3.14 and 3.15, please refer to Appendix A.

$$T = \frac{1}{6} m l^2 \dot{\theta_1}^2 + \frac{1}{2} M l^2 \dot{\theta_1}^2 + \frac{1}{2} M l L \dot{\theta}_1 \dot{\theta}_2 \cos(\theta_1 - \theta_2) + \frac{1}{2} M \left(\frac{R^2}{2} + \frac{L^2}{3} \right) \dot{\theta_2}^2 \tag{3.14}$$

$$U = -\left(\frac{m}{2} + M \right) l g \cos(\theta_1) - \frac{M}{2} L g \cos(\theta_2) \tag{3.15}$$

3.1.2. Equations of Motion

With the energy equation being derived, one possible way to determine the equations of motion of a system is by using the Lagrangian L and the Euler-Lagrange equation:

$$L = T - U \tag{3.16}$$

$$\frac{d}{dt}\left(\frac{\partial L}{\partial \dot{\vec{q}}}\right) - \frac{\partial L}{\partial \vec{q}} = 0\,, \qquad \vec{q} = \begin{bmatrix}\theta_1\\ \theta_2\end{bmatrix} = \Theta\,. \tag{3.17}$$

where $\vec{q}$ represents the vector of generalized coordinates that describe the system dynamics.

Substituting the previously derived expressions for kinetic and potential energy, it is possible to obtain L and, following Equation 3.17 for each DoF, the non-linear equations of motion of the system are derived:

$$\begin{cases} \left(\frac{m}{3} + M\right) l^2\ddot{\theta}_1 + \frac{1}{2}MlL\ddot{\theta}_2\cos(\theta_1 - \theta_2) + \frac{1}{2}MlL\dot{\theta}_2^2\sin(\theta_1 - \theta_2) + \left(\frac{m}{2} + M\right) lg\sin(\theta_1) = 0 \\ \frac{1}{2}MlL\ddot{\theta}_1\cos(\theta_1 - \theta_2) + M\left(\frac{R^2}{2} + \frac{L^2}{3}\right)\ddot{\theta}_2 - \frac{1}{2}MlL\dot{\theta}_1^2\sin(\theta_1 - \theta_2) + \frac{1}{2}MLg\sin(\theta_2) = 0 \end{cases} \tag{3.18}$$

As discussed in the literature review (see Chapter 2.1), the large geometric dimensions of the system lead to relatively small angular displacements during the monopile installation phase. Consequently, the equations of motion can be linearized around the stable equilibrium position of the pendulum ($\theta = 0$) using the small-angle approximation. By applying Equations 2.3, the following linearized system of equations of motion is obtained:

$$\begin{cases} \left(\frac{m}{3} + M\right) l^2\ddot{\theta}_1 + \frac{1}{2}MLl\ddot{\theta}_2 + \left(\frac{m}{2} + M\right) gl\theta_1 = 0 \\ \frac{1}{2}MLl\ddot{\theta}_1 + M\left(\frac{R^2}{2} + \frac{L^2}{3}\right)\ddot{\theta}_2 + Mg\frac{L}{2}\theta_2 = 0 \end{cases} \tag{3.19}$$

Linearization eliminates the trigonometric terms, resulting in a symmetric set of equations with respect to the two degrees of freedom. Both the linear and nonlinear formulations reveal that the system is coupled, as the motion of one degree of freedom influences the other. Additionally, it becomes evident how the geometry of the cable and of the hollow cylinder influence the governing equations. The full derivation of both the non-linear and linear equations of motion using Lagrangian mechanics is reported in Appendix A.

Following the derivation of the equations of motion, the geometric values presented in Table 3.1 were selected to enable the numerical evaluation based on the configuration used by Domingos et al. [5]. In particular, the mass of the monopile was modified, while the remaining parameters were kept approximately the same. This adjustment better reflects the scale and load conditions expected in offshore installation scenarios under the intended conditions. The motivation for modifying the monopile mass, while preserving the other parameters, is further discussed in Chapter 3.4.2.

Table 3.1: Parameter values used for the numerical model.

Parameter	Symbol	Value	Unit
Monopile's Mass	M	1,000,000	kg
Cable's Mass	m	2,000	kg
Monopile's Length	L	74	m
Cable's Length	l	80	m
Monopile's Radius	R	1.8	m
Gravitational Acceleration	g	9.81	$\frac{\text{m}}{\text{s}^2}$

3.2. Wave Characteristics

Following the theories presented in Ch.2.2, an essential step, before incorporating the submersion effects and the resulting hydrodynamic forces on the monopile model, is the characterization of the wave loading. Since wave-induced forces are the result of a random vibration process, their characteristics must be inferred and described through statistical analysis.

In this study, the required input parameters are obtained from publicly available datasets provided by the website Hersbach et al. [12]. The data is extracted for a location representative of offshore wind farm sites in the North Sea, specifically at Latitude $54°$ N and Longitude $6.2°$ E.

From the formulation of the JONSWAP spectrum in Ch.2.2.2, it is evident that the fetch length F, along with either the peak frequency f_p or the wind speed at 10 meters height U_{10}, are essential input parameters for constructing the wave spectrum. Additionally, another important parameter is the significant wave height H_s, that ensure that the resulting sea surface elevation time series accurately represents the expected wave loading behavior.

Fig. 3.2 presents the time series of wind velocity at a height of 10 meters above the surface. To characterize an extreme yet representative scenario, the mean values of the monthly maxima and minima are calculated. Given the vectorial nature of the data, which may assume negative values due to variations in wind direction, both positive and negative extremes are incorporated in the analysis. The maxima are indicated by red markers, whereas the minima are shown in green.

$$\text{Mean of monthly maxima:} \quad U_{10} = 13.6 \, \frac{\text{m}}{\text{s}}$$
$$\text{Mean of monthly minima:} \quad U_{10} = 10.1 \, \frac{\text{m}}{\text{s}}$$

The wind speed corresponding to the monthly maxima is the highest of the two. Thus, it is selected as the input for the wave spectrum calculation.

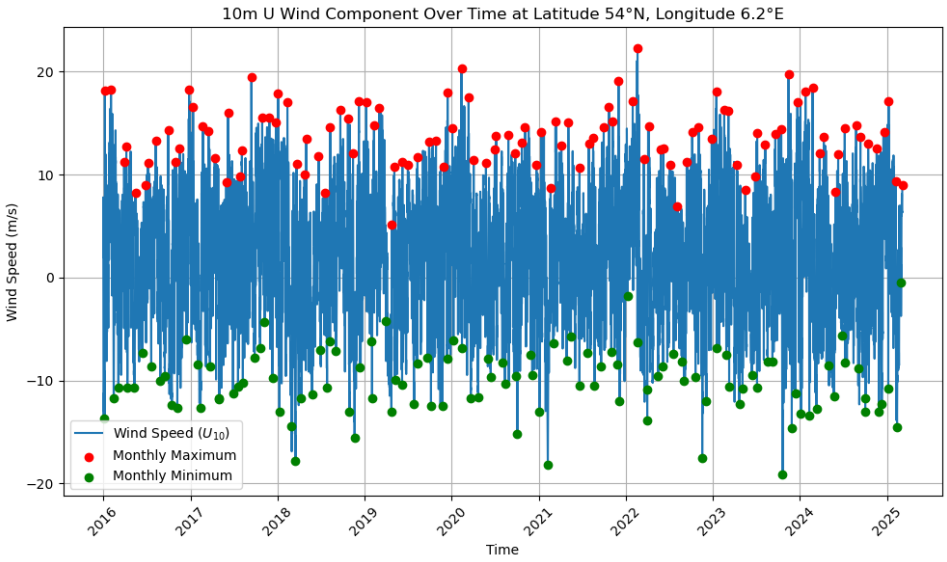

Figure 3.2: Mean wind speed at 10 m height time series in the North Sea

Using both wind direction data [2] and a geographical analysis of the North Sea, the effective fetch length for the selected location is estimated to range between $100 \sim 200$ km. For the purpose of this study, it is adopted a representative fetch of:

$$F = 150 \, \text{km}.$$

With known values for U_{10} and F, the significant wave height can be estimated using the JONSWAP-specific formula Equation 3.20.

$$H_s = 4\sqrt{1.67 \times 10^{-7} \cdot \frac{U_{10}^2}{g} \cdot F} = 2.75\,\text{m} \tag{3.20}$$

As shown in Figure 3.3, this calculated value is representative of an above-average significant wave height over time, supporting its use in further modeling for a preliminary control design.

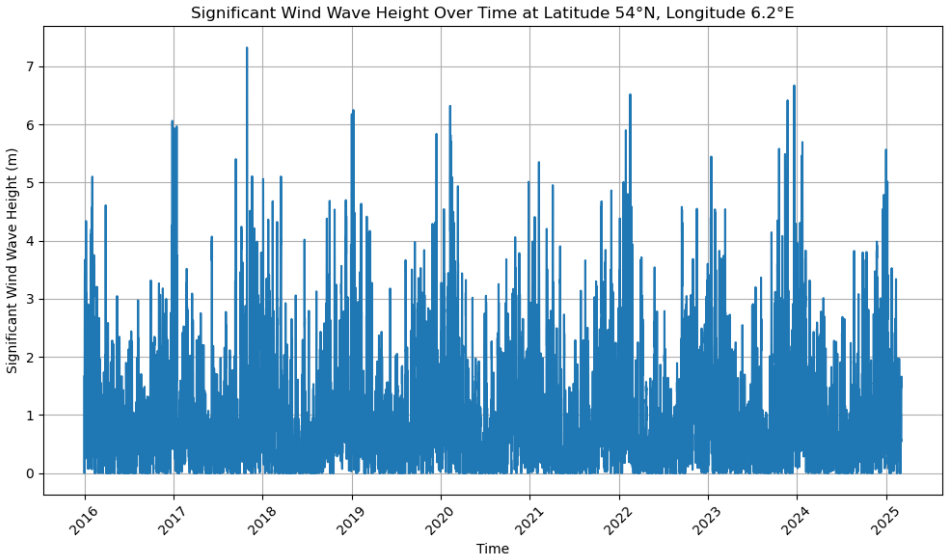

Figure 3.3: Significant wave height time series in the North Sea

The final set of parameters, used for constructing the JONSWAP spectrum, is presented in Table 3.2. These values were derived using U_{10} to derive f_p through Equation 2.13 as presented in Chapter 2.2.2.

Moreover, the study by Li, Gao, and Moan [18], which focuses on a similar region in the North Sea, reports the following representative wave conditions:

$$H_s = 2.5\,\text{m}, \quad T_p = 5 \sim 12\,\text{s}.$$

Thus, literature further support the validity of the parameters selected in this study.

As an additional check, the mean wave period T_s was also used to obtain the mean wave velocity via Equation 2.14 and to compute the other parameters. The results from this alternative method were found to be very similar and they are presented in Appendix B. Using both approaches provides a form of cross-validation, confirming the consistency of the parameters.

Table 3.2: Input parameters for constructing JONSWAP spectrum

H_s (m)	T_p (s)	f_p (Hz)	U_{10} (m/s)	F (km)
2.75	7.67	0.130	13.6	150

With the input parameters listed in Table 3.2, all the unknowns of the Equation 2.12 can be retrieved as shown in Chapter 2.2.2. The resulting JONSWAP spectrum is presented in Fig. 3.4.

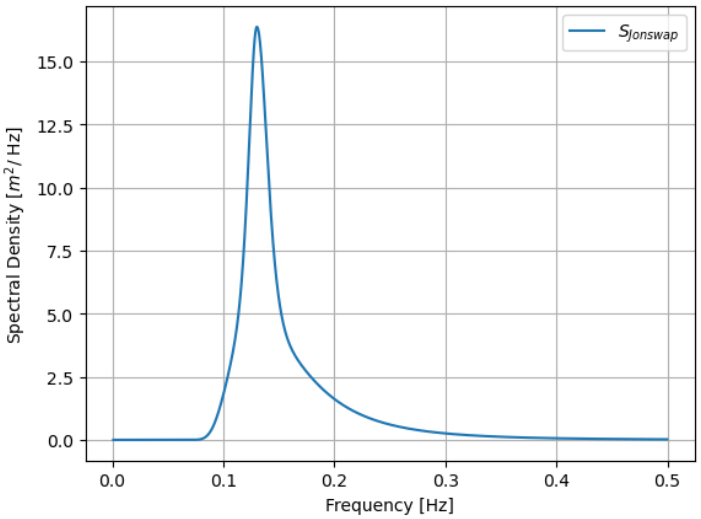

Figure 3.4: JONSWAP spectrum

Through Equation 2.8, using the spectral density energy at each frequency of the spectrum, it is possible to construct an irregular wave surface elevation time series. The time series preserves the stochastic nature of the sea state due to the phase angle ϕ_n. For consistency reason, always the same time series will be taken into account and is shown in Fig. 3.5.

To generate the JONSWAP spectrum and reconstruct the corresponding sea surface elevation time series, specific frequency and time resolution parameters are defined. The frequency range is set between a minimum of $f_{\text{min}} = 0.001$ Hz and a maximum of $f_{\text{max}} = 0.5$ Hz, capturing the relevant range of ocean wave energy. The frequency resolution is specified as $\Delta f = 0.0002$ Hz, which defines the smoothness and accuracy of the spectrum. From this, the total duration of the time series is determined as $t_{\text{max}} = 1/\Delta f = 5000$ s, ensuring compatibility between the time and frequency domains. The time step is set to $\Delta t = 1/f_{\text{max}} = 2$ s, satisfying the Nyquist sampling criterion for the highest frequency in the spectrum. As a result, the number of time steps used for reconstructing the time series is $N = t_{\text{max}}/\Delta t = 2500$, providing a well-resolved time-domain representation of the sea surface elevation.

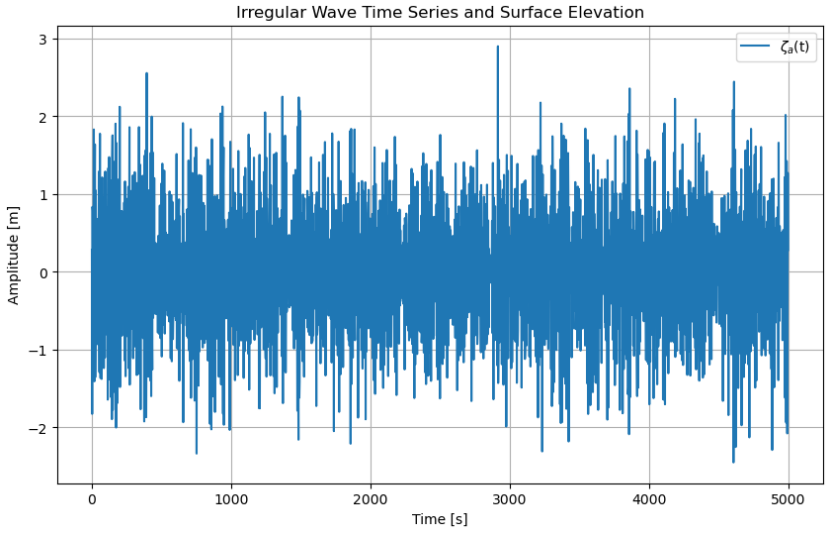

Figure 3.5: Wave height and surface elevation time series

To verify the accuracy of the time series and its representation of the JONSWAP spectrum, a convergence check was performed by comparing the standard deviation of the generated time series to the

theoretical standard deviation calculated from the JONSWAP spectrum. The standard deviation σ is computed, from the area under the JONSWAP spectrum, using Equation 3.21. In addition, also the significant wave height can be checked using Equation 3.22.

$$\sigma = \sqrt{m_0} = \sqrt{\int_0^\infty S(f)\, df} \tag{3.21}$$

$$H_s = 4 \times \sigma \tag{3.22}$$

Table 3.3 compares the standard deviation σ and the significant wave height H_s obtained from the generated time series and the spectrum. The close agreement, especially of σ, confirms that the constructed time series adequately represents the characteristics and behavior of the target spectrum.

Table 3.3: Comparison between results obtained from time series and spectrum.

Parameter	Symbol	Units	Time Series	Spectrum
Standard Deviation	σ	-	0.828	0.827
Significant Wave Height	H_s	m	3.31	2.75

3.3. Morison Equation

To incorporate the effects of submersion and hydrodynamic forcing in the dynamic model, the Morison equation is used. This choice is supported by the assumptions discussed in Ch.2.2.3, particularly the condition regarding the diameter-to-wavelength ratio. As shown in Table 3.1, a small radius is chosen for the monopile to ensure this ratio remains valid. Although this is a simplifying assumption, since it allows to neglect diffraction effects, it is justified by the results of the sensitivity analysis presented in Chapter 3.4.2.

In this study, the Morison equation (see Equation 2.18) incorporates two main variables: the structural motion $x(\theta_1, \theta_2)$, which is related to the rotational degrees of freedom of the double pendulum model, and the horizontal water particle velocity $u(t, z)$, which describes the wave-induced flow at a given depth.

Moreover, introducing hydrodynamic loading into the system requires a new reference frame to account for submersion, as shown in Figure 3.6. This redefinition is essential because the water particle velocity $u(t, z)$ and the hydrodynamic force both depend on time and submersion. For the force, submersion refers to the portion of the monopile below the water surface (hereafter referred to as the submersion length, $\mathscr{L}$), while for $u(t, z)$ it indicates the depth relative to the free surface, ranging from $z = 0$ at the surface down to $z = d$ at the seabed. In other words, both parameters describe vertical position, but z represents the depth level in the water column independent of the monopile, whereas submersion length describes the portion of the monopile that is submerged. Due to the assumptions made in this research, these two quantities are equivalent.

The structural motion at a point along the submerged monopile is described by:

$$x = l\theta_1 + (L + \mathscr{L} - s)\theta_2 \tag{3.23.a}$$

$$\dot{x} = l\dot{\theta}_1 + (L + \mathscr{L} - s)\dot{\theta}_2 \tag{3.23.b}$$

$$\ddot{x} = l\ddot{\theta}_1 + (L + \mathscr{L} - s)\ddot{\theta}_2 \tag{3.23.c}$$

where s is the vertical coordinate along the submerged part of the monopile, and is taken as negative below the water surface. The total submerged length $\mathscr{L}$ is also negative in this convention.

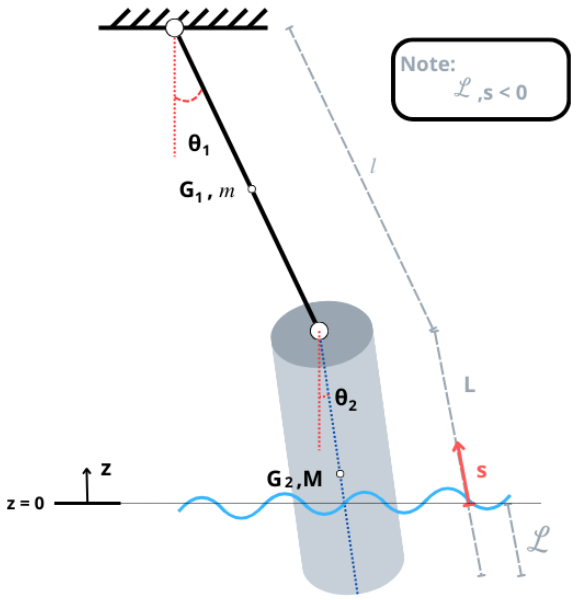

Figure 3.6: Submerged system reference frame

Since hydrodynamic forcing is distributed along the submerged length, it must be integrated across $\mathscr{L}$ to obtain the net forcing acting on the structure. Physically, this represents a continuous load; however, in the equations of motion, which are expressed in terms of angular degrees of freedom, the effect is introduced as a single equivalent moment. This moment is calculated by integrating the local force contributions multiplied by their respective lever arms. The result is a cumulative moment that captures the contribution of each submerged segment s of the monopile.

To clearly describe the hydrodynamic excitation, the force components are separated into drag and inertia terms according to Morison's formulation. These can then be added as either a combined moment or as separate moments in the system of equations 3.24. Although the moments appear only in the second equation of motion, due to the coupling between the cable and monopile, the response of the first body is also indirectly affected. This coupling is evident in Equation 3.23, where the structural motion depends on both θ_1 and θ_2.

Moreover, some components of the Morison's terms influence not only the forcing vector but also the mass matrix and damping characteristics of the system. This arises because the Morison forces depend on both the structural velocity and acceleration, thereby introducing additional damping and inertia effects beyond external forcing.

$$\begin{cases} \left(\frac{m}{3}+M\right) l^2\ddot{\theta}_1 + \frac{1}{2}MLl\ddot{\theta}_2 + \left(\frac{m}{2}+M\right) gl\theta_1 = 0 \\ \frac{1}{2}MLl\ddot{\theta}_1 + M\left(\frac{R^2}{2}+\frac{L^2}{3}\right)\ddot{\theta}_2 + Mg\frac{L}{2}\theta_2 = M_I + M_D \end{cases} \tag{3.24}$$

3.3.1. Inertia Component

The first term in the Morison equation accounts for the inertia force. As detailed in the literature review (see Equation 2.16), this term consists of two contributions: the Froude-Krylov force and the disturbance

force. Both depend on the horizontal water particle acceleration $\dot{u}(t, s)$, but only the second component includes the structural acceleration $\ddot{x}$. Thus, the inertia force can be rewritten as shown in Equation 3.25.

$$f_I = \frac{1}{4}\pi D^2 \rho_w \dot{u} + \frac{1}{4}\pi D^2 C_a \rho_w \dot{u} - \frac{1}{4}\pi D^2 C_a \rho_w \ddot{x} \tag{3.25}$$

The first two terms, on the right-hand side, are proportional to the fluid acceleration and represent external forcing. The third term depends on the system's acceleration and must be included in the system's mass matrix, as it contributes to the added mass effect. As such, this component directly influences the natural frequencies of the structure, particularly it allows to determine the undamped natural frequencies at each submersion length as done in Ch.3.4.3.

The horizontal water particle acceleration used in the forcing terms is:

$$\dot{u}(s,t) = -\sum_{n=0}^{N-1} A_n \omega_n^2 \frac{\cosh(k_n(d+s))}{\sinh(k_n d)} \sin(\omega_n t + \phi_n) \tag{3.26}$$

Figure 3.7 shows how $\dot{u}(s,t)$ evolves across depth for 50 time steps out of a 5000 seconds simulation. On the vertical axis, the submersion depth ranges from 0 to $-40\,\mathrm{m}$, and each color represents a different moment in time. From the plot, it is clear that the particle acceleration is random in nature, due to the stochastic wave spectrum. Stronger accelerations occur near the surface (0 to $-10\,\mathrm{m}$), where wave energy is most concentrated, and then decay exponentially with depth. Beyond approximately $-30\,\mathrm{m}$, the signal becomes nearly constant and significantly weaker. The lower limit of $-40\,\mathrm{m}$ was selected based on the analysis discussed in Chapter 3.4.3.

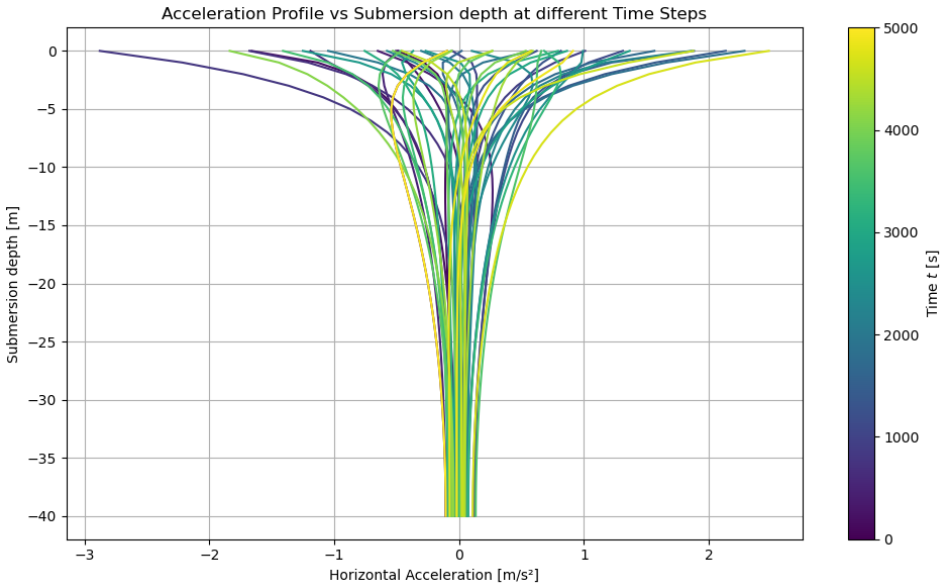

Figure 3.7: Horizontal water particle acceleration profile $\dot{u}(s,t)$ across submersion depths for different time steps.

The distributed force f_I induces a moment on the structure. The total moment is computed by integrating over the submerged length as presented in Equation 3.27. This expression accounts for the moment arms associated with the pendulum geometry and includes both structural and hydrodynamic contributions. Moreover, due to the dependence of the moment equation on θ_1, the first degree of freedom is also indirectly affected by the forcing term through coupling in the second equation of motion.

$$M_I(t) = \int_{\mathscr{L}}^{0} [l + (L + \mathscr{L} - s)]\, f_I(s,t)\, ds = \\ = \int_{\mathscr{L}}^{0} [l + (L + \mathscr{L} - s)] \left[\frac{1}{4}(1 + C_a)\pi D^2 \rho_w \dot{u}(s,t) - \frac{1}{4}\pi D^2 C_a \rho_w \ddot{x} \right] ds \tag{3.27}$$

Figure 3.8 shows a possible evolution of the cumulative inertia moment $M_I(t)$ for 50 time steps. The moment magnitude is on the order of $1 \times 10^7\,\mathrm{Nm}$, peaking at a submersion depth of approximately $12\,\mathrm{m}$, after which it decreases. The initial rise reflects the increasing lever arm and stronger fluid acceleration near the surface, while the decreasing pattern corresponds to the diminishing contribution from deeper layers, where acceleration oscillates between positive and negative values. Despite this trend, the moment profile is irregular, confirming the randomness of the excitation.

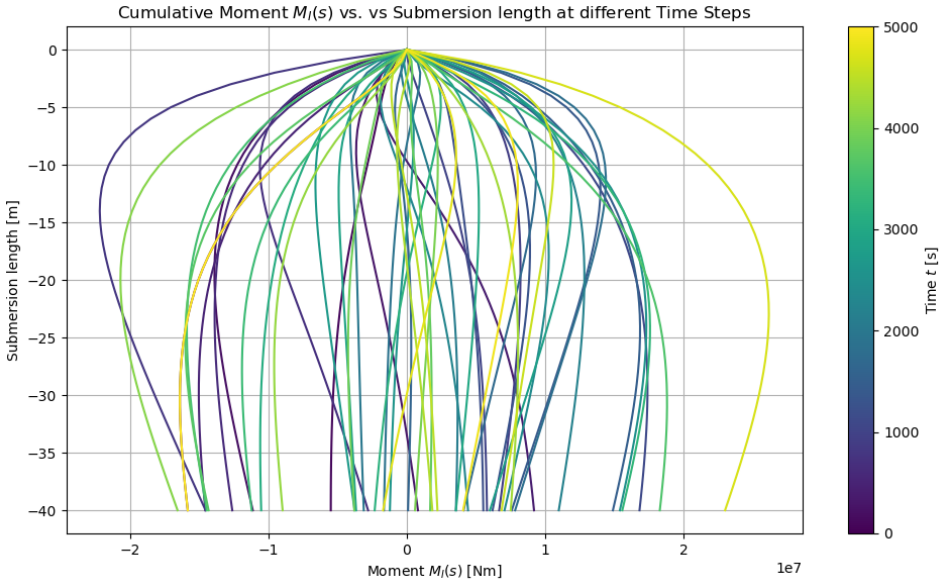

Figure 3.8: Cumulative inertia moment M_I across submersion lengths at different time steps.

In summary, the inertia component contributes to the internal system dynamics through added mass and to time-varying external loading. These effects cannot be approximated as uniform or periodic especially closer to the surface, where wave-induced forces are strongest and most variable.

3.3.2. Drag Component

The drag component of the Morison equation introduces a fundamentally different contribution to the system's dynamics compared to the inertia term. While the inertia force depends linearly on the water particle acceleration and the structural acceleration, the drag force is inherently nonlinear, as it depends on the square of the relative velocity between the fluid and the structure. This term, shown in Equation 2.17, couples the external flow field and structural response in a way that prevents their individual separation.

In this context, the drag term contributes both as a time-varying and depth-dependent forcing effect, due to the external wave field, and as an intrinsic damping effect linked to the structural velocity, which consistently acts to resist motion and dissipate energy.

The nonlinearity is particularly important.The drag force opposes motion and increases quadratically with the relative velocity, meaning it acts as a velocity-squared damping mechanism. Hence, when the structure moves in phase with the wave-induced flow, the relative velocity, and thus drag, is low.

However, when motion is out of phase, the relative velocity increases, and the drag term grows significantly dissipating more energy and amplifying the nonlinear damping effect. The horizontal water particle velocity $u(s,t)$ used in the drag moment term is defined in Equation 2.10.

Figure 3.9 illustrates the temporal evolution of $u(s,t)$ along the submersion depth. As with the acceleration case (Fig. 3.7), the velocity profile is visibly stochastic, reflecting the random nature of the input wave spectrum. Stronger velocities are observed in the upper water column (from 0 to approximately $-15\,\mathrm{m}$), where the wave energy is concentrated, and decay exponentially with submersion depth. Beyond $-30\,\mathrm{m}$, the profile becomes vertical, indicating a minimal contribution from deep water layers.

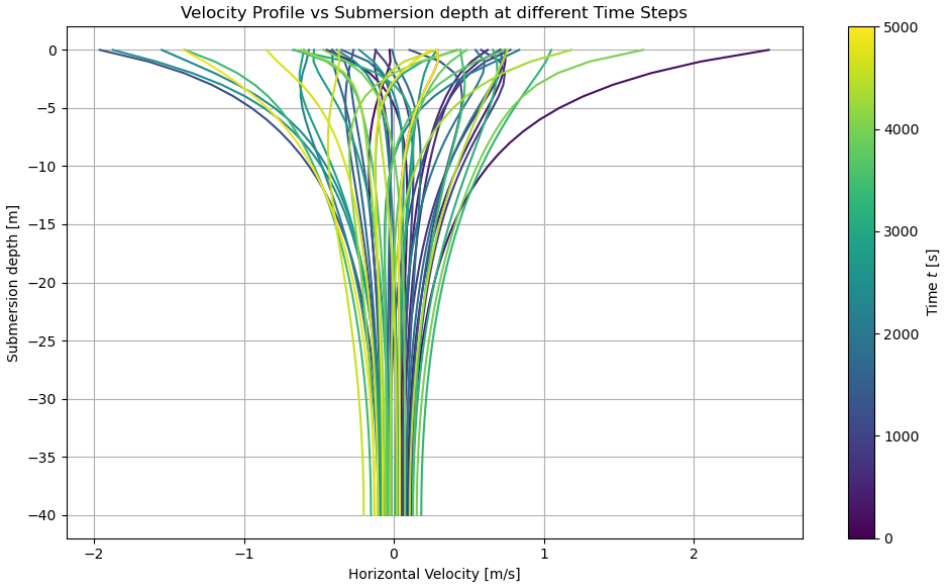

Figure 3.9: Horizontal water particle velocity profile $u(s,t)$ across submersion lengths at different time steps.

The distributed drag force $f_D(s,t)$ generates a moment on the structure, integrated over the submerged portion. The resulting moment is given in Equation 3.28, which combines the geometric moment arms with the nonlinear interaction between the fluid velocity $u(s,t)$ and the structural velocity $\dot{x}(s,t)$. As for the inertia component, the dependence on θ_1, results in the first degree of freedom being indirectly influenced through coupling in the second equation of motion.

$$\begin{aligned} M_D(t) &= \int_{\mathscr{L}}^{0} [l + (L + \mathscr{L} - s)]\, f_D(s,t)\, ds = \\ &= \int_{\mathscr{L}}^{0} [l + (L + \mathscr{L} - s)] \left[\frac{1}{2} D C_D \rho_w (u(s,t) - \dot{x}(s,t)) |u(s,t) - \dot{x}(s,t)| \right] ds \end{aligned} \tag{3.28}$$

Figure 3.10 presents the evolution of the cumulative drag-induced moment $M_D(t)$ over time and submersion length. The magnitude of the moment reaches approximately $1 \times 10^6\,\mathrm{Nm}$, which is lower compared to the inertia-induced moment. This difference suggests that during monopile installation, the hydrodynamic load is primarily inertia-dominated in terms of excitation. However, in this research, the drag contribution is retained as a fundamental component due to the damping it introduces. The velocity-squared term ensures continuous energy dissipation, which plays a central role in enabling a more robust and effective control strategy avoiding resonance.

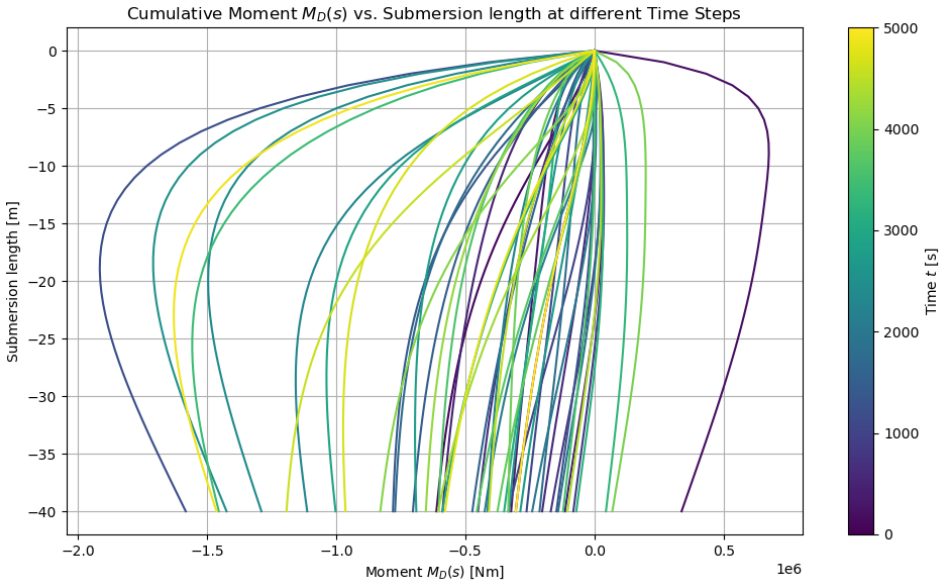

Figure 3.10: Cumulative drag moment M_D across submersion lengths at different time steps.

Therefore, the drag component introduces complex nonlinear coupling between wave excitation and structural response. The velocity-squared nature of the drag effect ensures that damping is always present, reinforcing the importance of its contribution to both excitation and dissipation in the system.

3.4. Free Vibration of the System

To gain insight into the natural dynamic behavior of the double pendulum system, a free vibration analysis is conducted. This involves studying the system in the absence of external forces by solving the homogeneous form of the equations of motion. The initial analysis focuses on the double pendulum without any influence of water or wave loading. This forms the foundation for understanding the intrinsic behavior of the system.

The analysis enables the identification of the system's natural frequencies and mode shapes, which describe how the structure tends to vibrate when disturbed. This information is essential, as resonance can occur when external excitations match one of these natural frequencies, potentially leading to large and unsafe oscillations. This is particularly important in the context of offshore installation, where the natural frequencies of crane–load systems often fall within the range of ocean wind-generated wave frequencies.

To validate the results, two independent methods are employed to analyze the system in the frequency domain:

- The first approach assumes a harmonic solution, enabling the analytical determination of the system's oscillatory behavior. This method is commonly referred to as modal analysis.
- The second approach involves reformulating the second-order system into first-order state-space form, allowing the system's vibrations to be studied through eigenvalue analysis.

In this chapter, only the modal analysis is presented, while the details of the state-space formulation and eigenvalue analysis are provided in Appendix C. This second approach will later serve as the foundation for the numerical integration of the equations of motion once external disturbances and control forces are included.

In Chapter 3.4.3, the influence of the surrounding water is accounted for through the added mass term of the Morison equation, enabling an investigation into how varying submersion depths affect the system's undamped natural frequencies. This analysis offers valuable insight into how the hydrodynamic

environment, and specifically the depth at which the monopile is submerged during installation, modifies the system's intrinsic characteristics.

It is important to highlight that this study focuses exclusively on undamped natural frequencies. The drag force, which introduces nonlinear damping through its dependence on the square of the relative velocity between the structure and the fluid, is not included in this part of the analysis.

3.4.1. Modal Analysis of Double Pendulum

Before applying the modal analysis, the linearized equations of motion are conveniently rewritten in matrix form as:

$$\mathbf{M}\ddot{\Theta} + \mathbf{K}\Theta = 0 \tag{3.29}$$

where:

$$\mathbf{M} = \begin{bmatrix} \left(\frac{m}{3} + M\right) l^2 & \frac{1}{2}MLl \\ \frac{1}{2}MLl & M\left(\frac{R^2}{2} + \frac{L^2}{3}\right) \end{bmatrix}, \quad \mathbf{K} = \begin{bmatrix} \left(\frac{m}{2} + M\right) lg & 0 \\ 0 & \frac{1}{2}MLg \end{bmatrix}, \quad \Theta = \begin{bmatrix} \theta_1 \\ \theta_2 \end{bmatrix}, \quad \ddot{\Theta} = \begin{bmatrix} \ddot{\theta}_1 \\ \ddot{\theta}_2 \end{bmatrix}. \tag{3.30}$$

Modal analysis relies on the assumption of a harmonic solution to determine the natural frequencies and mode shapes of a system. By substituting a sinusoidal time response into the linear equations of motion, the problem is transformed into a generalized eigenvalue problem.

The starting point is the homogeneous system (Equation 3.29). Then a harmonic solution is assumed (Equation 3.31) and differentiated twice with respect to time for substitution in the equations of motion.

$$\Theta(t) = \hat{X}e^{i\omega t} \tag{3.31}$$

$$\ddot{\Theta}(t) = -\omega^2\hat{X}e^{i\omega t} \tag{3.32}$$

Substituting Equation 3.32 in Equation 3.29, gives:

$$(-\omega^2\mathbf{M} + \mathbf{K})\hat{X}e^{i\omega t} = 0 \tag{3.33}$$

In the above equations, $\hat{X}$ represents the vector for the mode shapes while ω denotes the natural frequencies. Since $e^{i\omega t} \neq 0$, it can be factored out, leading to the generalized eigenvalue problem:

$$(\mathbf{K} - \omega^2\mathbf{M})\hat{X} = 0 \tag{3.34}$$

To ensure a nontrivial solution ($\hat{X} \neq 0$), the determinant of the coefficient matrix must be set equal to zero. Solving Equation 3.35 yields the natural frequencies ω_n of the system, where n stands for the degree of freedom considered. For each frequency, the corresponding mode shape $\hat{X}_n$ is found by solving the associated eigenvector equation. These mode shapes describe the deformation patterns of the system at each resonant frequency.

$$\det(\mathbf{K} - \omega_n^2\,\mathbf{M}) = 0 \tag{3.35}$$

Using the values listed in Table 3.1, Equation 3.35 can be numerically solved with respect to ω^2, allowing to determine the natural frequency of the system that are reported in Table 3.4.

Table 3.4: Natural frequencies of the double pendulum system

Modes Natural Frequency	Hz	rad/s
Mode 1	0.045	0.284
Mode 2	0.174	1.095

Once the natural frequencies are identified, the associated mode shapes (eigenvectors) can be determined solving Equation 3.34 for $\hat{X}$. Under the small-angle approximation, these eigenvectors can be interpreted as angular displacements and visualized as linear displacements, facilitating the interpretation of the system's motion at resonance. The normalized mode shapes are reported in Table 3.5. These results can be further visualized in Figure 3.11, which illustrates the relative motion of the components excited at each natural frequency.

Table 3.5: Eigenvectors of the double pendulum system

Modes Natural Frequency	[-]
Mode 1	$\begin{bmatrix} -0.668 \\ -0.744 \end{bmatrix}$
Mode 2	$\begin{bmatrix} -0.458 \\ 0.889 \end{bmatrix}$

The results of the free vibration analysis reveal a large gap between the first and second natural frequencies. Consistent findings were obtained through the eigenvalue analysis of the state-space formulation presented in Appendix C, confirming the free vibration results.

More specifically, the first natural frequency aligns closely with the value reported by Domingos et al. [5]. The second natural frequency is also in good agreement, although slightly higher than that observed in the reference study. This discrepancy may originate from differences in the stiffness and mass matrices. While the geometric parameters in the present model are similar to those used in the reference, they are not identical, especially the mass of the monopile. Additionally, the variation could be attributed to the simplification in the model that includes two degrees of freedom compared to the three considered by Domingos et al. [5].

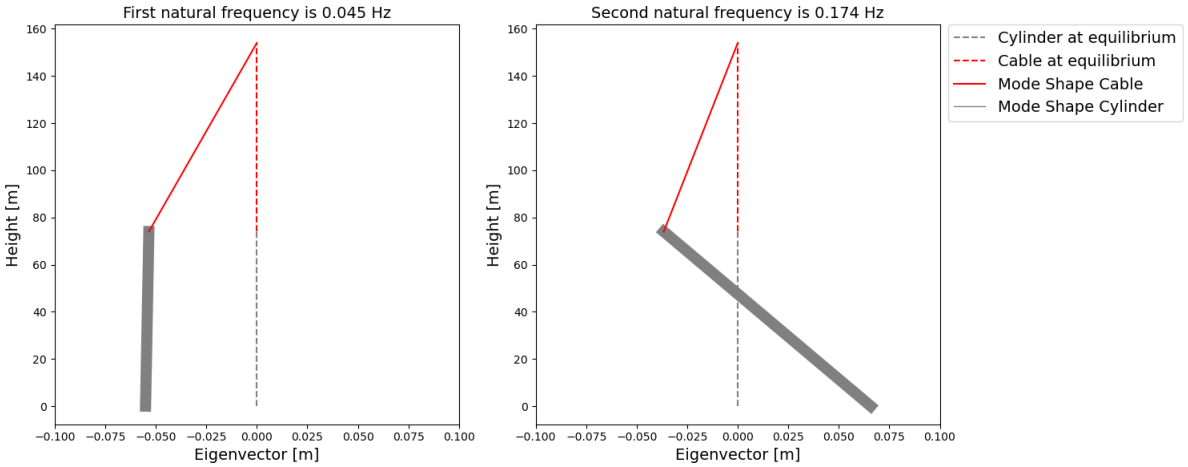

Figure 3.11: Modal Shapes of Double Pendulum

In the following section, the influence of key model parameters on the natural frequencies is investigated, offering deeper insight into the dynamic behavior of the system.

3.4.2. Effect of Model Parameters on Natural Frequencies

To gain a deeper understanding of the behavior of the natural frequencies, a sensitivity analysis was conducted on the key geometrical parameters defining the system. These parameters directly affect both the mass and stiffness matrices, thereby influencing the system's dynamic response.

Starting from the values of Table 3.1, three scaling parameters were introduced to investigate the relationship between the system's geometric properties and its natural frequencies. These parameters allow for systematic variation of the physical dimensions. For both the bodies of the system, the mass, the length, and the radius are assumed to scale proportionally, meaning that an increase in one leads to a corresponding increase in the others.

- Cable length parameter ξ_l - assumes direct proportionality between the cable's mass m and its length l.

$$m = 2000 \cdot \xi_l, \quad l = 80 \cdot \xi_l \tag{3.36}$$

- Monopile length parameter ξ_L - assumes direct proportionality between the monopile's mass M and its length L.

$$M = 1 \times 10^6 \cdot \xi_L, \quad L = 74 \cdot \xi_L \tag{3.37}$$

- Monopile radius parameter ξ_R - assumes direct proportionality between the monopile's mass M and its radius r.

$$M = 1 \times 10^6 \cdot \xi_R, \quad R = 1.8 \cdot \xi_R \tag{3.38}$$

The scale parameters are varied from 0.01 to twice their original values, and the corresponding natural frequencies of the system are computed and plotted against these variations.

$$0.01 < \xi_l, \xi_L, \xi_R < 2$$

The natural frequencies are determined by the interplay between the mass and stiffness matrices, as expressed in Equation 3.39.

$$\omega = \sqrt{\frac{K}{M}} \tag{3.39}$$

This sensitivity analysis therefore enables a comprehensive investigation of the influence of the double pendulum's geometrical properties on its natural frequencies. Moreover, it provides a basis for assessing whether the values listed in Table 3.1 represent reasonable assumptions.

Analysis of the elongation of the cable - ξ_l

First, the sensitivity analysis focuses on the effect of changing the geometry of the first pendulum by varying ξ_l, which affects both the mass m and the length l. More specifically, this is one of the most interesting cases for the research since it also corresponds to the lowering of the monopile through the elongation of the cable.

The results presented in Fig.3.12 show that both the first and second natural frequencies decrease as the parameter increases, indicating that as the geometry of the cable expands, the system's oscillations occur at lower frequencies, meaning the system moves with a higher period.

Increasing ξ_l affects both the mass and the stiffness matrices, but $\mathbf{M}$ is more sensitive to changes in the cable geometry. As a result, from the relation 3.39, the system's inertia increases faster than its stiffness, leading to a reduction in frequency. The first natural frequency decreases from 0.071 Hz to 0.035 Hz as ξ_l increases. Similarly, the second natural frequency decreases from 1.120 Hz to 0.158 Hz, with a particularly sharp drop observed when ξ_l increases from 0.01 to 0.25.

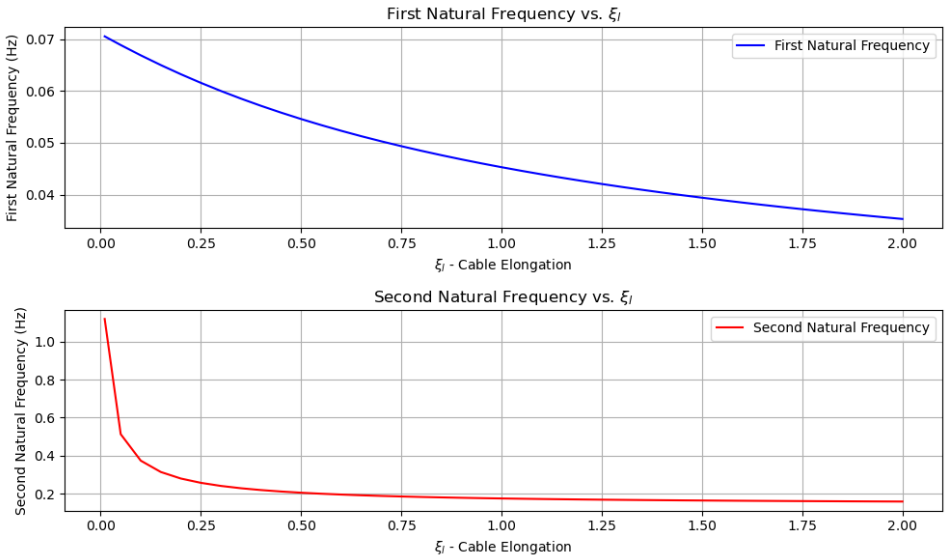

Figure 3.12: Effect of elongation of the cable on the natural frequencies

It can be concluded that the lowering of the monopile influences both natural frequencies of the system in a similar manner. A slight reduction in frequency is observed when the system dimensions are increased. However, when the cable dimensions are reduced to less than half of the reference configuration, the second natural frequency is significantly affected. Furthermore, the variation of the first natural frequency indicates that, for accurately simulating monopile installation, it is essential to account for changes in the cable geometry, as these may have a considerable impact on the results.

Analysis of the elongation of the monopile - ξ_L

The next part of the analysis involves varying the geometry of the second body by adjusting the scale factor ξ_L. Similar to the cable, increasing the values of the parameter leads to a proportional change in both mass M and length L. The variation of the natural frequencies is shown in Fig. 3.13

For the first natural frequency, the trend observed is similar to that of the first body: as ξ_L increases, the first natural frequency decreases. This is because the increase in mass and inertia outweigh the increase in stiffness, leading to lower frequencies and longer periods.

For the first natural frequency, the trend observed is similar to that of the first body: as ξ_L increases, the first natural frequency decreases. This occurs because the increase in mass and inertia outweighs the increase in stiffness, leading to lower frequencies and longer periods. In particular, the first natural frequency decreases from 0.056 Hz to 0.039 Hz as ξ_L increases.

The second natural frequency exhibits a different trend compared to the first. At small values of ξ_L, the frequency initially increases due to the dominant effect of system stiffness and stronger coupling between the two pendulums. However, after a critical point is reached, the influence of the mass matrix outweighs that of the stiffness matrix, and the system's inertia becomes dominant. As a result, the natural frequency decreases as the system grows heavier and more resistant to motion. Specifically, the second natural frequency decreases from 0.41 Hz to 0.145 Hz as ξ_L increases beyond the critical value of approximately $\xi_L = 0.05$.

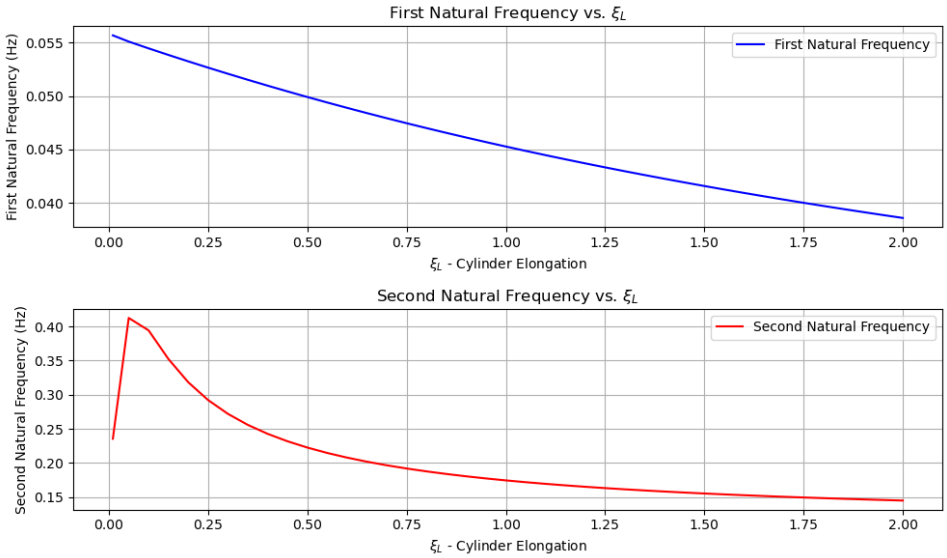

Figure 3.13: Effect of elongation of the monopile on the natural frequencies

The results support the decision to increase the mass of the monopile to a more representative value compared to the one used by Domingos et al. [5], as this parameter has a significant impact on the system's dynamics. Moreover, the analysis highlights the importance of the coupling between the two bodies, showing that changes in the geometry of the second body can significantly influence both natural frequencies, particularly the second one.

Analysis of the radius scaling of the monopile - ξ_R

The monopile is also characterized by its radius, and this geometry is scaled using the parameter ξ_R. As ξ_R increases, both the radius and the mass of the monopile increase leaving the thickness constant, leading to potential changes in the natural frequencies of the system.

The analysis presented in Fig. 3.14 reveals that the impact of the radius scaling on the natural frequencies is relatively minimal. For the first natural frequency, an increase in the radius results in a slight decrease in frequency, similar to the trends observed for other geometric parameters. However, the change in frequency is quite small. The first natural frequency decreases slightly from 0.0454 Hz to 0.0453 Hz as ξ_R increases.

The second natural frequency exhibits a different behavior. Initially, the frequency increases as ξ_R increases, reaching a peak value of approximately 0.175 Hz at $\xi_R \approx 0.3$. Beyond this point, however, the frequency begins to decrease slowly, with the value reducing to around 0.173 Hz as the scaling parameter ξ_R continues to increase.

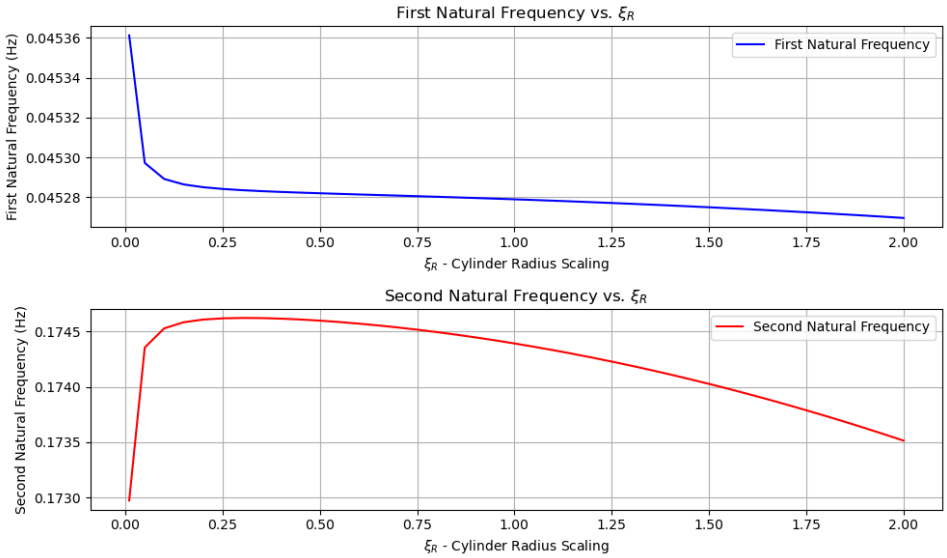

Figure 3.14: Effect of radius of the monopile on the natural frequencies

In comparison to the effects of other geometric parameters, the radius scaling has a relatively small impact on the natural frequencies. This suggests that the radius does not significantly influence the system's behavior as much as other parameters such as length scaling. Consequently, retaining the radius value from Domingos et al. [5] is justified, as its impact on the natural frequencies is minimal. Moreover, the results confirm that the small-radius assumption of the Morison equation is satisfied, ensuring that diffraction effects can be neglected while still providing an accurate representation of the system's dynamic response to wave loading.

3.4.3. Effect of Submersion on Natural Frequencies

Having previously analyzed the free vibration behavior of the double pendulum without external influences, the effect of water submersion is now considered. This step is essential, as during monopile installation, the structure is slowly lowered into the sea after upending until it reaches the seabed. As discussed in Chapter 3.3, the presence of water introduces not only external forcing but also hydrodynamic effects such as added mass and drag. For the study of undamped natural frequencies, drag, which introduces damping, is neglected, while the added mass is incorporated through the mass matrix.

The equations of motion are therefore updated to include the added mass contribution. Specifically, the mass matrix is modified to reflect the additional inertial effects due to water submersion. These effects influence both the degrees of freedom and introduce coupling between them, as seen from Equation 3.27. Moreover, the installation of a monopile requires the cable to elongate as the monopile is brought to the seabed, meaning that both the cable length l and its mass m vary with submersion. The updated mass matrix is presented in Equation 3.41, where the added inertia terms are evaluated through integration along the submerged portion of the monopile, while the cable geometry (l and m) varies as a function of the submersion length $\mathscr{L}$.

$$l(\mathscr{L}) = l - \mathscr{L} \quad , \quad m(\mathscr{L}) = m + \left(\frac{m}{l} \cdot |\mathscr{L}|\right) \ . \tag{3.40}$$

$$\mathbf{M} = \begin{bmatrix} \left(\frac{m(\mathscr{L})}{3} + M\right) l(\mathscr{L})^2 & \frac{1}{2} M L l(\mathscr{L}) \\ \frac{1}{2} M L l(\mathscr{L}) \ + \ M_{\text{Inertia}}(\ddot{\theta}_1, \mathscr{L}) & M\left(\frac{R^2}{2} + \frac{L^2}{3}\right) \ + \ M_{\text{Inertia}}(\ddot{\theta}_2, \mathscr{L}) \end{bmatrix} , \tag{3.41.a}$$

$$M_{\text{Inertia}}(\ddot{\theta}_1) = \int_0^{\mathscr{L}} [l(\mathscr{L}) + (L + \mathscr{L} - s)] \left(\frac{1}{4}\pi D^2 C_a \rho_w l(\mathscr{L}) \ddot{\theta}_1\right) ds \ , \tag{3.41.b}$$

$$M_{\text{Inertia}}(\ddot{\theta}_2) = \int_0^{\mathscr{L}} [l(\mathscr{L}) + (L + \mathscr{L} - s)] \left(\frac{1}{4}\pi D^2 C_a \rho_w (L + \mathscr{L} - s)\ddot{\theta}_2 \right) ds \, . \tag{3.41.c}$$

The effect of submersion is analyzed using modal analysis. This method enables solving the eigenvalue problem in Equation 3.35 for different values of submerged length, giving insight into how natural frequencies evolve as the monopile enters the water.

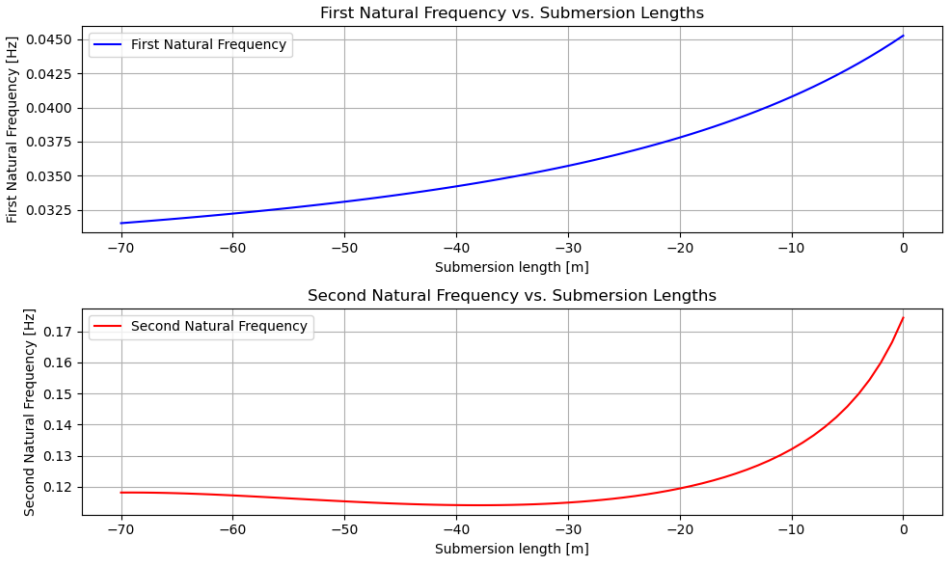

Figure 3.15: Effect of submersion length on natural frequencies of the double pendulum system

Figure 3.15 shows how the natural frequencies decrease with increasing submersion length. This trend is expected, as the added mass increases the overall inertia of the system. Although both the mass and stiffness matrices are affected by the changing cable geometry (length l and mass m), the relative ratio between stiffness and inertia decreases due to the more dominant effect of the added mass. This leads to a lower natural frequency, as reflected in the classical relation presented in Equation 3.39.

This behavior is also consistent with the sensitivity analysis of the non-submerged double pendulum system (see Section 3.4.2), where an increase in m and l resulted in a reduction of the natural frequency.

Both natural frequencies are affected due to coupling in the system, but the second mode exhibits the most significant change. It drops from an initial frequency of 0.174 Hz to approximately 0.114 Hz, with most of the reduction occurring within the first 20 meters of submersion.

Based on this trend, several key submersion lengths are selected for further analysis in the time domain and in the design of the control strategy. The unsubmerged case ($\mathscr{L} = 0$ m) is included to represent the baseline free vibration response without any added mass. To capture the sharp reduction in natural frequencies observed in the early stages of submersion, the cases $\mathscr{L} = -5$ m, -10 m, and -15 m are considered. Additionally, submersion lengths of -20 m and -30 m are included to monitor the gradual approach toward the minimum, which occurs at -40 m. Table 3.6 summarizes the corresponding natural frequencies for each of these selected cases while Table 3.7 does the same but for the mode shapes.

Table 3.6: Variation of natural frequencies [Hz] of the double pendulum system with submersion length

$\mathscr{L}$ [m]	Mode 1 Frequency [Hz]	Mode 2 Frequency [Hz]
0	0.045	0.174
-5	0.043	0.146
-10	0.041	0.132
-15	0.039	0.124
-20	0.038	0.119
-30	0.036	0.115
-40	0.034	0.114

Table 3.7: Normalised amplitude of the mode shapes of the double pendulum system at different submersion lengths

$\mathscr{L}$ [m]	Mode 1 – θ_1	Mode 1 – θ_2	Mode 2 – θ_1	Mode 2 – θ_2
0	-0.0534	-0.0551	-0.0366	0.0658
-5	-0.0501	-0.0598	-0.0383	0.0661
-10	-0.0476	-0.0628	-0.0395	0.0665
-15	-0.0459	-0.0648	-0.0403	0.0670
-20	-0.0448	-0.0662	-0.0409	0.0675
-30	-0.0440	-0.0678	-0.0414	0.0686
-40	-0.0447	-0.0687	-0.0413	0.0695

Figures 3.16 and 3.17 illustrate the mode shapes for the shallowest and deepest submersion depths considered. While the natural frequencies change with submersion, the mode shapes remain qualitatively similar to those of the unsubmerged case shown in Figure 3.11. The first mode shape exhibits the most noticeable variation, especially in the orientation of the second body, which becomes nearly horizontal as submersion decreases and approaches the water surface.

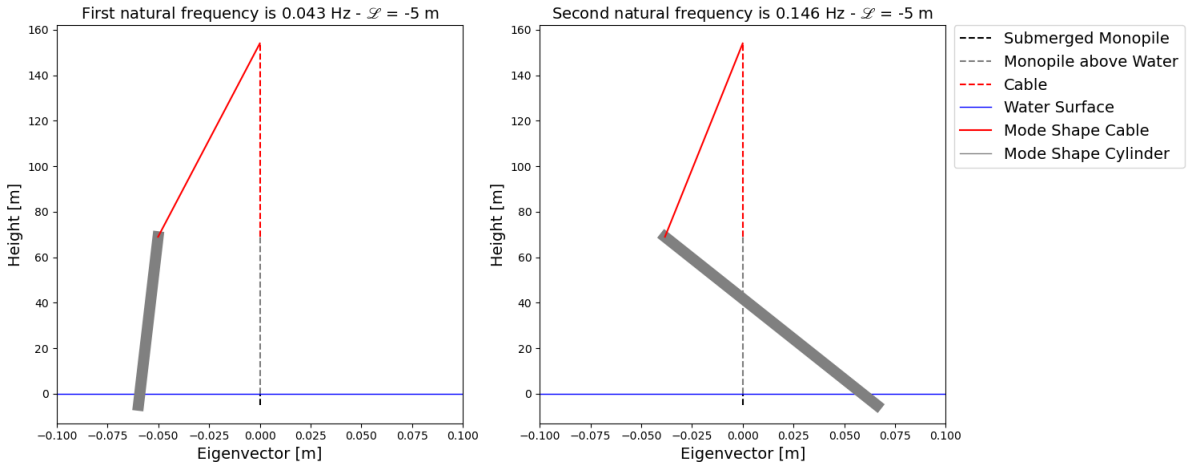

Figure 3.16: Mode shape of the double pendulum system at a submerged length of -5 m

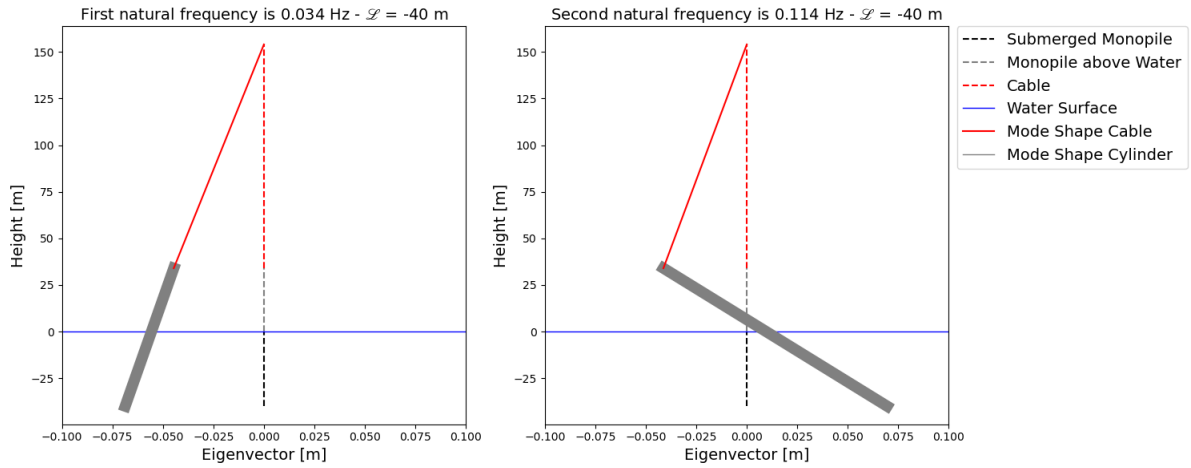

Figure 3.17: Mode shape of the double pendulum system at a submerged length of -40 m

3.5. Time Domain Response

After the frequency domain free vibration analysis, the focus shifts to the system response in the time domain. This is particularly important because it provides the rotational response of the monopile and cable to a given external forcing or initial condition, effectively simulating their possible oscillations during installation. Understanding this response is fundamental for developing an efficient control strategy that adapts over time based on the magnitude of the system's oscillations.

Given the presence of nonlinearities, such as drag forces and, further into the research, magnetic control forces, analytical solutions are not feasible. Consequently, a numerical simulation approach is adopted. The method starts from rewriting the second-order differential equation describing the system dynamics into a first-order state-space form as previously mentioned in Chapter 3.4. This allows the use of standard ordinary differential equation (ODE) solvers.

As seen previously dynamic system is governed by the matrix differential equation

$$\mathbf{M}\,\ddot{\Theta} + \mathbf{K}\,\Theta = F(t), \tag{3.42}$$

where $\Theta = [\,\theta_1,\, \theta_2\,]^T$ contains the generalized coordinates. To numerically integrate this system, the augmented state vector is defined, leading to the state-space formulation (see Appendix C).

$$X = \begin{bmatrix} \Theta \\ \dot{\Theta} \end{bmatrix} = \begin{bmatrix} y_1 \\ y_2 \\ x_1 \\ x_2 \end{bmatrix}$$

$$\frac{d}{dt}X = \begin{bmatrix} 0 & \mathbf{I} \\ -\mathbf{M}^{-1}\mathbf{K} & -\mathbf{M}^{-1}\mathbf{C} \end{bmatrix} X + \begin{bmatrix} 0 \\ \mathbf{M}^{-1}F(t) \end{bmatrix}, \tag{3.43}$$

At each time step, the solver receives the current state vector $X = [y_1, y_2, x_1, x_2]^T$, computes the acceleration $\ddot{\Theta}$, and returns the time derivatives $\dot{X} = [\,\dot{\Theta}, \ddot{\Theta}\,]^T$.

For the numerical integration, the LSODA solver is employed due to its capability to efficiently handle systems with variable stiffness and nonlinearities. LSODA automatically switches between an implicit and an explicit solver based on the detected stiffness of the system. This adaptability is particularly beneficial for the present study where, submerged length changes, fluid-structure interaction effects and nonlinear drag introduce transient stiffness variations. LSODA's adaptive time-stepping ensures stability and accuracy without prior knowledge of the system's stiffness [30].

3.5.1. Time Domain Analysis of the Response without External Forcing

The case without external forcing is first analyzed in the time domain, corresponding to the simulation with a submersion length of $\mathscr{L} = 0\,\mathrm{m}$. The system response is obtained by applying a nonzero initial condition. Figure 3.18 presents the rotational displacements of the two degrees of freedom over time.

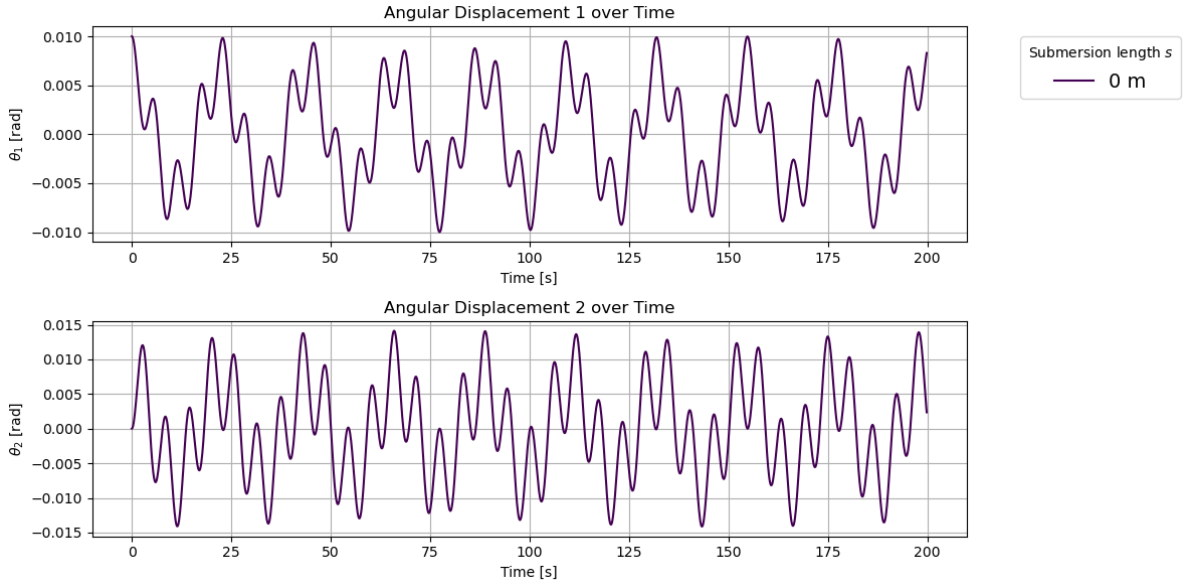

Figure 3.18: Time domain response of the two degrees of freedom at zero submersion length with initial condition applied to the first body.

The response exhibits oscillations governed by the initial condition applied to the first body. The corresponding frequency content, obtained via a fast Fourier transform (FFT) and presented in Figure 3.19, confirms that the frequencies excited coincide with the natural frequencies previously identified in Chapter 3.4.1. The first degree of freedom is mainly dominated by the first natural frequency, reflecting the initial condition being applied to the cable. In contrast, the second degree of freedom displays an increasing influence of the second natural frequency, reaching a comparable magnitude. This behavior highlights the dynamic coupling between the two bodies, where excitation of the cable also activates the second natural frequency in the monopile.

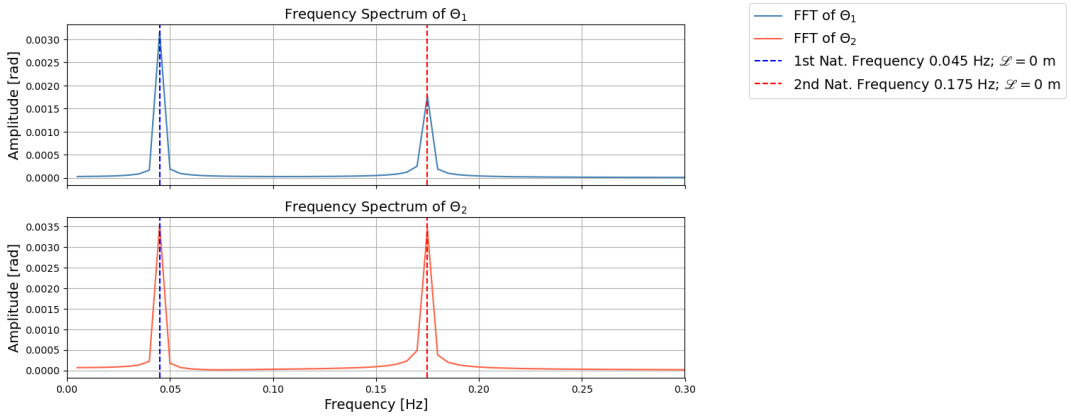

Figure 3.19: Frequency amplitude spectrum of the two degrees of freedom before submersion.

3.5.2. Time Domain Analysis of the Response with Morison Equation Forcing

External forcing is introduced into the system by incorporating the added mass and damping effects arising from the components of Morison's equation, as described in Chapter 3.3. Numerical simulations are then performed for different submersion lengths of the monopile, replicating the installation procedure.

Figures 3.20 illustrates the time domain angular responses for different submersion lengths. The angular displacements for both degrees of freedom remain around 0.2 rad, supporting the validity of the small-angle approximation in this simulation context.

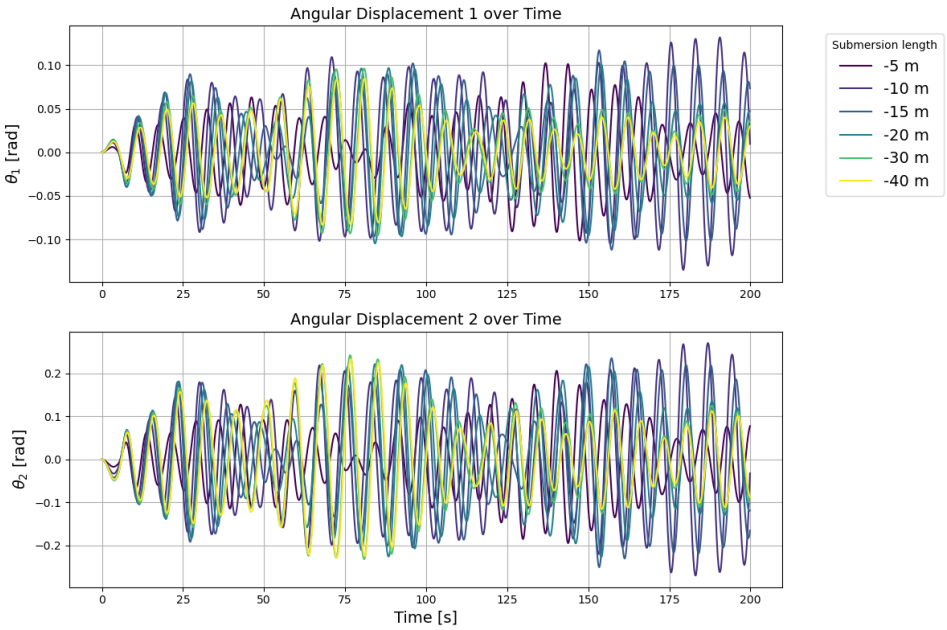

Figure 3.20: Time domain response of the system under full Morison forcing for multiple submersion lengths

As expected, the monopile's angular displacement is generally greater than that of the cable, since the wave load directly acts on the second body while the first is influenced mainly through coupling effects. Notably, the monopile's displacement remains significant and cannot be neglected.

The numerical simulations indicate that the maximum response occurs for submersion lengths between -10 and -15 meters. This finding is in agreement with the cumulative drag and inertia moments shown in Figures 3.10 and 3.8, which demonstrate that the highest excitation arises at these submersion levels. On the contrary, the weakest response corresponds to the -40 meter submersion, where the forcing is weaker. For comparison, Figure 3.22 compares the time domain responses at these two extremes. Given that other responses fall between these bounds, the control strategy developed in Chapter 4 focuses primarily on these submersion lengths.

While these results provide a clear picture of the system response, it should be noted that the added mass coefficient C_a, as discussed in Chapter 2.2.3, varies significantly in shallow submersions, which may affect the accuracy of the results for the smallest depths.

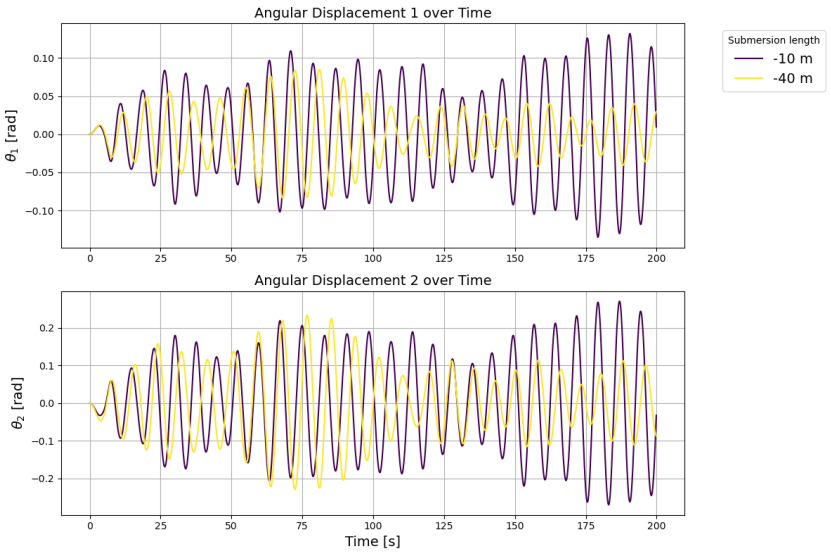

Figure 3.21: Comparison of time domain responses at submersion lengths of -10 m and -40 m

The effect of drag is highlighted by comparing the full Morison forcing response with that obtained considering only the inertia component, shown in Figure 3.22. The drag forces act as an energy dissipation mechanism, preventing unbounded growth of oscillations that would otherwise occur with inertia forcing alone. This damping effect is crucial in containing the response amplitudes and ensuring realistic system behavior. The graph shows that at lower submersion lengths, the angular displacement for both degrees of freedom tends to resonate and reach very high values. However, for submersion lengths around -30 to -40 meters, the response becomes large but does not continue to grow indefinitely. This is likely due to increased energy dissipation from drag forces, which become more effective as the submerged length increases, combined with the reduction in wave-induced forcing magnitude at greater depths.

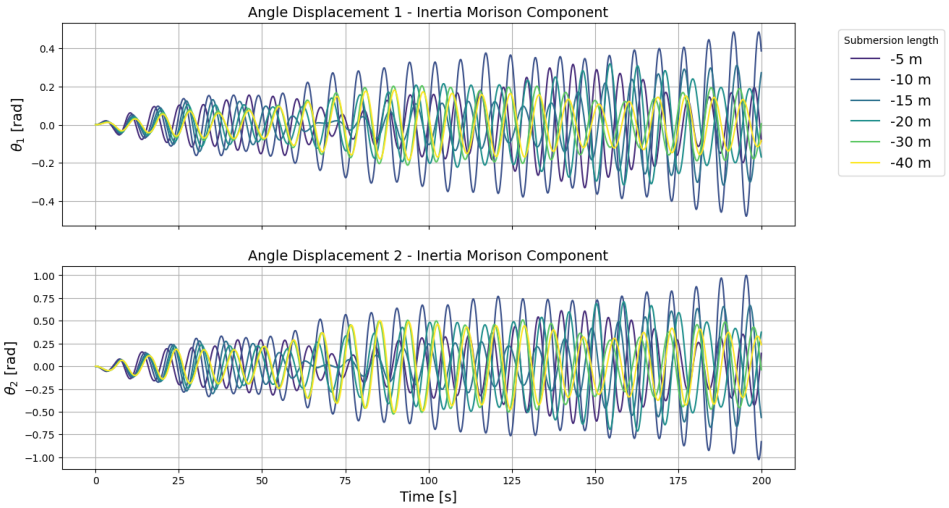

Figure 3.22: Time-domain response of the system under inertia dominant Morison forcing

Furthermore, Figure 3.20 shows that all submersion lengths exhibit clear beating patterns, indicative of the interaction of multiple frequency components. This behavior arises from closely spaced frequencies in the wave forcing, characterized by a spectrum of energy. The beating is particularly pronounced for submersion lengths between -5 and -20 meters, whereas at deeper submersions such as -30 and -40 meters, the forcing is weaker and more broadband, resulting in less noticeable beating.

The amplitude spectrum of the FFT of the response at a submersion of -10 meters, shown in Figure 3.23), indicates that the second natural frequency dominates, while the first natural frequency is only weakly excited. Additional peaks close to the second frequency are also present, consistent with the irregular wave forcing described by the JONSWAP spectrum in Figure 3.4 and the beating pattern observed. Moreover, the JONSWAP spectrum peaks at $f_p = 0.13$ Hz, which lies close to the second natural frequency, explaining the relative prominence of this mode in the response.

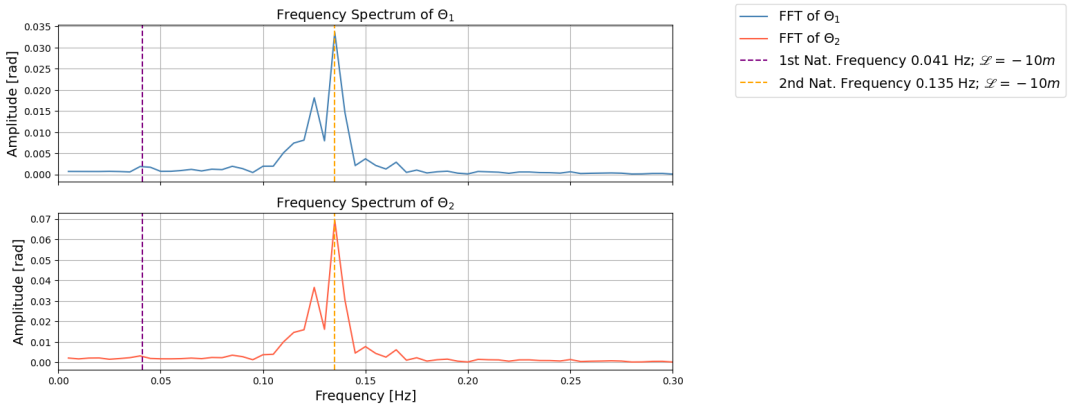

Figure 3.23: Frequency amplitude spectrum at -10 m submersion length

It should be noted that, due to the computational cost of the numerical solver, the time-domain simulation was limited to 200 seconds. This constraint reduces the frequency resolution in the FFT and limits spectral precision.

Fig. **??** shows the system responses at each constant submersion level. However, during installation these levels occur sequentially over time rather than independently. To capture this process more realistically, Fig. **??** presents a simulation with a time-varying submersion length. In this case, $\mathscr{L}$ is progressively lowered of 5 m every 20 seconds, starting from -5 m and reaching -40 m.

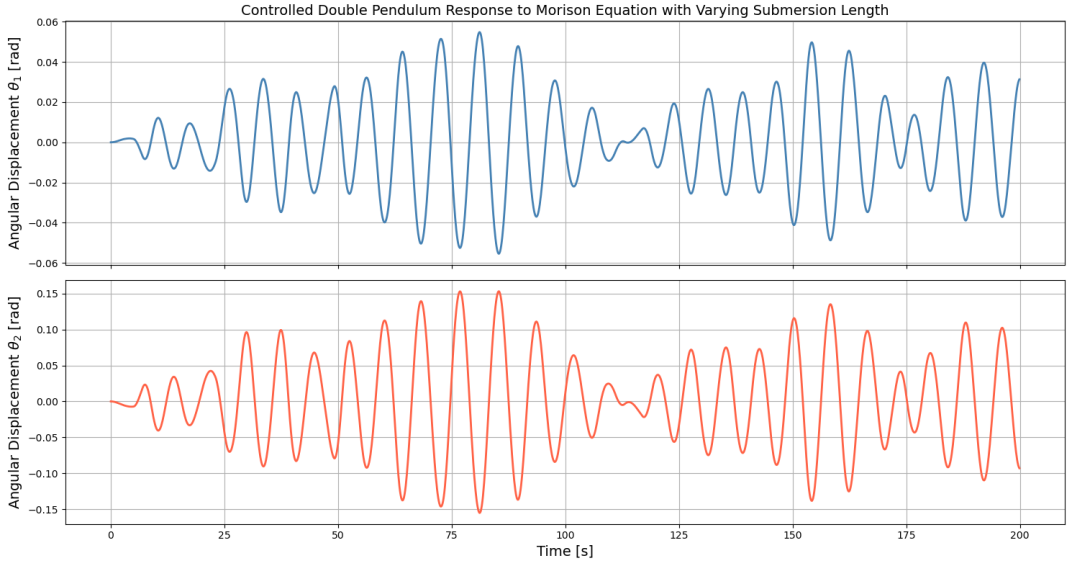

Figure 3.24: Time-domain response of the system under full Morison forcing with varying submersion lengths in time

The angular displacements still exhibit the characteristic beating phenomenon, but the peak responses of both θ_1 and θ_2 are lower than those observed under constant submersion levels. As expected, the response tends to decrease with deeper submersion since the hydrodynamic excitation on the monopile

becomes weaker. Nevertheless, this simulation is relatively short, so these trends should be interpreted with caution given the strong temporal fluctuations of the response.

Overall, the time-domain simulations support the modeling assumptions made and provide key angular response insights that form the foundation for the control strategy developed in the next chapter.

4

Magnetic Control Strategy for Double Pendulum System

4.1. Implementation of Magnetic Control

After determining the system's response during the installation procedure under wave loading, it is now possible to develop an efficient control strategy. This strategy uses dipole-dipole magnetic interaction to counteract the angular displacements by generating an appropriate magnetic moment.

As introduced in Chapter 2.3, this non-contact control method combines the magnetic moment generated between dipoles and a Proportional-Derivative (PD) controller. The double pendulum system derived in Chapter 3 provides the framework for implementing this strategy.

The magnetic moment applied to the system is derived from the magnetic potential energy by differentiating it with respect to the generalized coordinate vector $\Theta = [\theta_1, \theta_2]^T$, using the general formulation introduced in Equation 2.25. Under the small-angle approximation, the distance between the interacting dipoles is defined in Equation 4.1 and illustrated in Fig. 4.1. In the equation, ℓ is the cable length, L_x defines the location of the fixed magnet along the monopile, and d is the distance between the dipoles when the system is at rest.

$$r(\Theta) = \theta_1 \ell + \theta_2 L_x + d \tag{4.1}$$

The magnetic potential energy W_m is expressed in Equation 4.2, while the corresponding magnetic moment $M_m(\Theta)$, derived by taking the partial derivative of W_m with respect to the generalized coordinates Θ, is presented in Equation 4.3.

$$W_m = -\frac{\mu_0}{4\pi \left(\theta_1 \ell + \theta_2 L_x + d\right)^3} (2 m_{c,x} m_{t,x}) \tag{4.2}$$

$$M_m(\boldsymbol{\Theta}) = -\frac{6\mu_0 m_{c,x} m_{t,x}}{4\pi \left(\theta_1 \ell + \theta_2 L_x + d\right)^4} \begin{bmatrix} \ell \\ L_x \end{bmatrix} \tag{4.3}$$

This moment introduces two additional external forcing terms in the system of equations presented in Equation 4.4: one coupling term in the first equation and one direct moment acting on the second equation, reflecting the influence of the magnetic force on the monopile.

$$\begin{cases} \left(\frac{m}{3} + M\right) l^2 \ddot{\theta}_1 + \frac{1}{2} M L l \ddot{\theta}_2 + \left(\frac{m}{2} + M\right) g l \theta_1 = -\frac{6\mu_0 m_{c,x} m_{t,x}}{4\pi(\theta_1 \ell + \theta_2 L_x + d)^4} \ell \\ \frac{1}{2} M L l \ddot{\theta}_1 + M \left(\frac{R^2}{2} + \frac{L^2}{3}\right) \ddot{\theta}_2 + M g \frac{L}{2} \theta_2 = M_I + M_D - \frac{6\mu_0 m_{c,x} m_{t,x}}{4\pi(\theta_1 \ell + \theta_2 L_x + d)^4} L_x \end{cases} \tag{4.4}$$

Control is achieved by dynamically adjusting the external magnetic dipole moment $m_{t,x}$, which characterizes the strength and geometry of the actuating magnet. As outlined in Chapter 2.3.3, a Proportional-Derivative (PD) controller is implemented to provide feedback control based on both position and velocity errors. The error signal $e(t)$, defined in Equation 4.5, captures the difference between the desired displacement $\xi = 0$ and the actual horizontal displacement of the monopile. The resulting control law, which determines the necessary magnetic dipole moment $m_{t,x}$, is given by Equation 4.6.

$$e(t) = \xi - x(t) = \xi - (\theta_1 \ell + \theta_2 L_x) \tag{4.5}$$

$$c(t) = m_{t,x} = K_p(\xi - (\theta_1 \ell + \theta_2 L_x)) + K_d(\dot{\xi} - (\dot{\theta}_1 \ell + \dot{\theta}_2 L_x)) \tag{4.6}$$

The proportional and derivative gains K_p and K_d must be carefully tuned to ensure the desired position is reached while maintaining system stability. Moreover, several other parameters influence the control strategy, such as the distance between the external and monopile magnets d, the positioning L_x of the magnet along the monopile and the submersion length ($\mathscr{L}$).

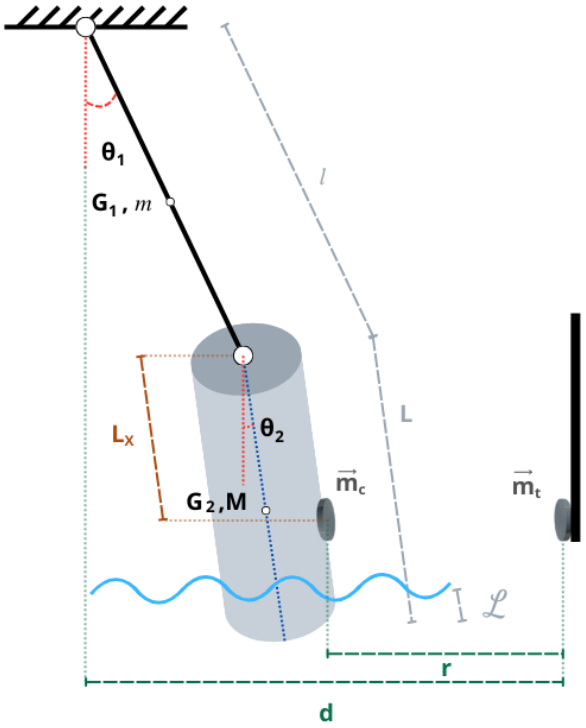

Figure 4.1: Simplified model for monopile installation using magnetic control.

To determine suitable values for K_p and K_d, and an efficient placement of the magnets along the monopile, a simplified wave forcing model is adopted. This simplification is necessary due the computational cost of the full simulation, which includes nonlinear magnetic interactions and wave-induced drag. On the other hand, the influence of the remaining parameters, particularly those related to geometry and submersion, will be assessed using the moment formulation introduced in Chapter 3, where the wave loading is modeled in greater detail.

4.2. Control of the System Subjected to Harmonic Moment

Building on the simplification introduced above, this section presents a trial and error tuning process for the proportional and derivative gains (K_p and K_d) using a simplified version of the forcing. A harmonic moment, chosen to reflect the amplitude of the irregular wave-induced loading, is applied to enable a faster and more efficient evaluation of the controller response across different gain settings. The same setup is also leveraged to explore optimal magnet positions along the monopile, enabling testing without the computational burden of the full non-linear model.

The applied harmonic moment is expressed in Equation 4.7, where M_0 is the amplitude of the torque and f_0 is its frequency. The value of $M_0 = 5 \times 10^7$ Nm is chosen to be slightly higher than the maximum wave moment previously estimated (see Fig. 3.8) to be conservative in the control design. The frequency $f_0 = 0.1$ Hz corresponds to a representative component of the wave spectrum (see Fig. 3.4) and is intentionally selected not to coincide with the natural frequencies of the system identified in Chapter 3.4.

$$M_{harmonic}(t) = M_0 \ \sin(2\pi f_0 \cdot t) \quad \text{where} \quad M_0 = 5 \times 10^7 \text{ Nm}, \quad f_0 = 0.1 \text{ Hz} \tag{4.7}$$

This forcing is added as external moment to the second equation of motion in the coupled system (see Equation 4.4). The subsequent subsections present two control configurations: first, the case with a single magnet; then, the more advanced case with a pair of magnets, which introduces a moment couple. The latter case presents one of the main advantages of using magnetic control that is the ability to apply forces and moments at multiple points along the monopile without any physical contact, something not possible with traditional systems.

In both cases, the parameter values listed in Table 4.1 are used for quantities not yet defined, which contribute to the magnetic moment expression in Equation 4.3.

Table 4.1: Parameters used in the magnetic moment model.

Parameter	Symbol	Value	Unit
Controlled magnet dipole moment	m_c	1	A·m^2
Magnet offset distance	d	0.5	m
Vacuum permeability	μ_0	$4\pi \times 10^{-7}$	N/A^2

The single magnet case is addressed first since this configuration provides a useful baseline for understanding the limitations of a localized control. Moreover, from a modeling and control design perspective, the single magnet scenario is simpler and less computationally demanding, which makes it a suitable starting point for tuning control gains and validating the control strategy.

4.2.1. Single Magnet Control Strategy

In order to facilitate the tuning of the controller gains, a single magnet configuration is first analyzed. The magnet is placed at $L_x = 37$ m, which corresponds to the centroid of the monopile. This configuration also closely resembles the control scheme used in current industrial installation practices where the monopiles are guided during the post-upending phase through a gripper (see Fig. 4.2).

The values of the proportional and derivative gains were determined through trial and error. Multiple combinations of gains were tested to evaluate their influence on the angular displacements, θ_1 and θ_2, as well as the linear displacement, $x(t) = \theta_1 l_1 + \theta_2 L_x$. Note that setting $K_p = 0$ and $K_d = 0$ is equivalent to having no control acting on the system.

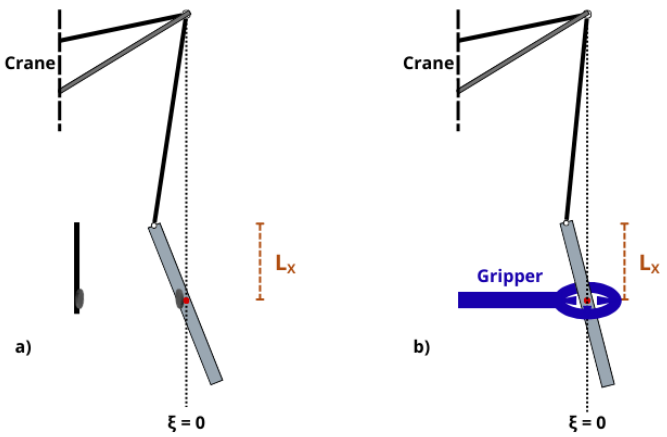

Figure 4.2: Comparison of control strategies: a) single magnet non-contact control strategy; b) gripper control strategy.

Fig. 4.3 shows the response of θ_2 and displacement at L_x, where the control is activated after 100 seconds in the simulation. The angular displacement shows limited improvement across all gain combinations. This outcome is expected because the control is localized at a single point along the monopile. Therefore, it cannot resist rotations effectively. This behavior highlights one of the main limitations of single-point control systems such as grippers, which cannot suppress the full angular motion of the structure.

On the other hand, the control can have a significant impact on the linear displacement response. When the gains reach or exceed $K_p = 10^{12}$ and $K_d = 10^{12}$, the displacement is driven effectively toward the target value $\xi = 0$. Below this threshold, specifically for $K_p = 10^{11}$, the displacement diverges and increases over time. Moreover, in the marginal case of $K_p = 10^{12}$, control is successful only if K_d is also equal to 10^{12}. Any reduction in the derivative gain with this scenario causes instability or uncontrolled behavior (see the legend for case $K_p = 10^{12}$ and $K_d = 10^{11}$ in the figure).

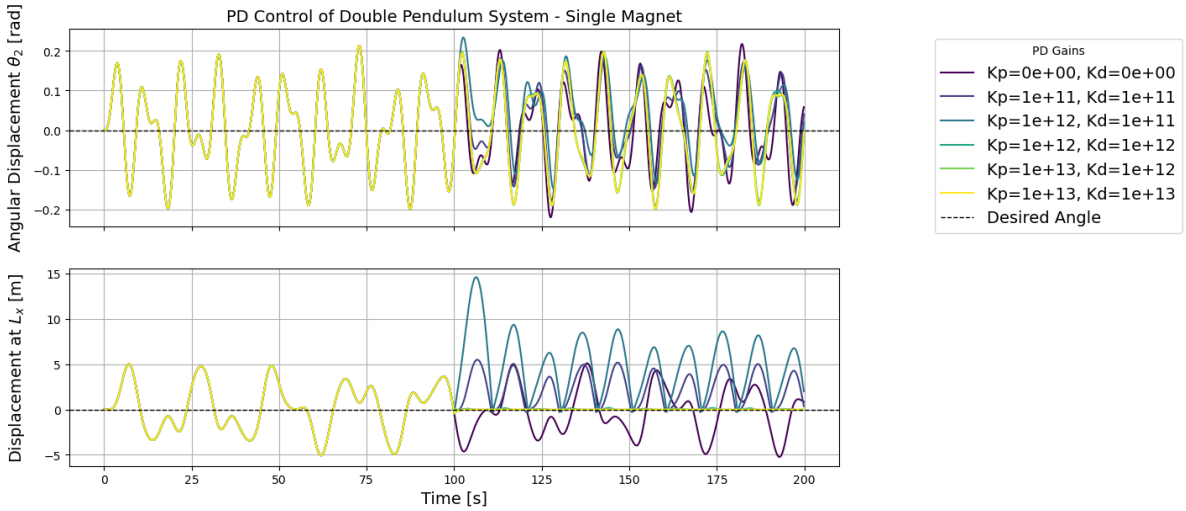

Figure 4.3: Single magnet control - Effect of PD gain values on angular and horizontal displacement under harmonic moment.

Based on these findings, $K_p = 10^{13}$ is selected to ensure stability even in the presence of irregular wave-induced loading, which may produce more abrupt moment fluctuations than the harmonic case. Moreover, while $K_p = 10^{12}$ and $K_d = 10^{12}$ is also an effective combination (see the legend for case $K_p = 10^{12}$ and $K_d = 10^{12}$ in the figure), the sensitivity to K_d in that case suggests a reduced robustness. On the other hand, once $K_p = 10^{13}$, the effect of varying K_d is reduced, indicating the system is

dominated by proportional action. Nevertheless, for consistency and conservatism, $K_d = 10^{13}$ is also adopted. Therefore, the values selected for the proportional and derivative gains after extensive testing are:

$$K_p = 1 \times 10^{13} \quad \text{and} \quad K_d = 1 \times 10^{13}$$

This equal-gain strategy weights position error and velocity error equally, helping avoid overshoot and oscillations in the control response. In particular, as mentioned in Chapter 2.3.3, the K_p gain increases the effective stiffness of the double pendulum, while K_d enhances its damping. Hence, the chosen values dramatically increase both stiffness and damping, enforcing a rigid-like control of the monopile and suppressing undesired oscillations.

During the testing phase, smaller values of K_p and K_d were found to be insufficient: either the system became unstable and diverged or it exhibited large overshoots and prolonged oscillations. The selected values of 10^{13} represent gains for which the control was able to stabilize the system effectively while maintaining accurate tracking.

It is important to note that, since the angular displacement is not directly controlled, the system's displacement is regulated to the target value only at the location of the single magnet, L_x (see Fig. 4.4). Further down the monopile, the displacement increases due to the inclination induced by the uncontrolled angle. This single-magnet analysis therefore serves as a benchmark for evaluating the benefits of extending the control strategy to a moment-couple configuration. By employing a double-magnet setup, it is expected that not only the displacement at specific locations but also the rotational behavior of the system can be influenced, providing a more complete and effective form of control.

4.2.2. Double Magnet Strategy

Following the identification of optimal gain values in the single magnet control strategy, this section investigates the application of those same parameters in a more advanced configuration: the double magnet strategy. As previously mentioned, the advantage of using two magnetic dipoles along the monopile, is the ability to influence both the angular displacement of the structure and the horizontal displacement at multiple control points, thereby enhancing controllability as shown in Fig. 4.4.

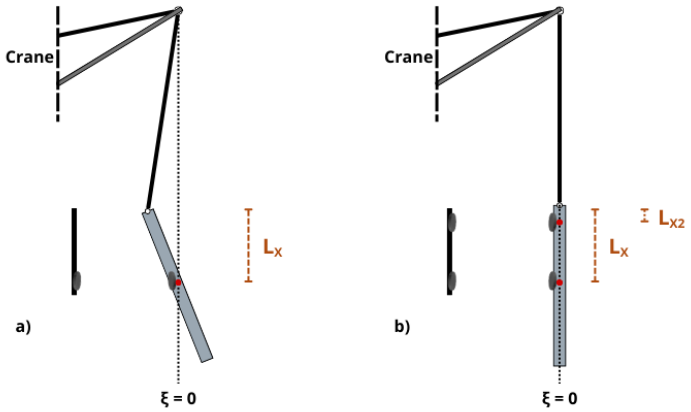

Figure 4.4: Comparison of non-contact control strategies: a) single magnet strategy; b) double magnets strategy.

In this configuration, one magnet is placed at $L_x = 37\,\text{m}$, located at the centroid of the monopile, to allow direct comparison with the single magnet case. The second magnet is positioned at $L_{x2} = 2\,\text{m}$, close to the top of the monopile but with a margin to the edge of the cylinder. This layout enables the generation of a magnetic couple moment that is more suitable for all vibrational mode shapes.

The pair of proportional and derivative gains that showed good performance in the single-magnet analysis is now reassessed for the double-magnet strategy to verify whether it remains effective. The

objective of this configuration is to achieve accurate and efficient control by simultaneously regulating the angular displacements of both degrees of freedom, θ_1 and θ_2, while minimizing the horizontal displacements at the two magnet locations, L_x and L_{x2}.

Figure 4.5 shows the angular responses of the two degrees of freedom under harmonic excitation for different gain combinations. For $K_p = 10^{13}$, both angular displacements are well controlled across derivative gains of $K_d = 10^{12}$ and 10^{13}. This marks a clear improvement compared to the single-magnet case, where rotational control could not be achieved with any pair of gain values.

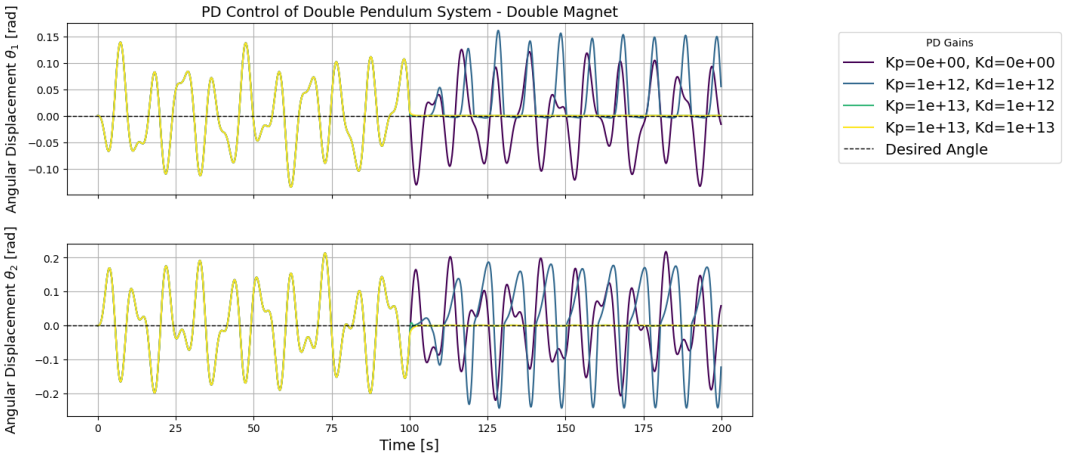

Figure 4.5: Double magnet control — Effect of PD gain values on angular displacements θ_1 and θ_2 under harmonic moment.

The corresponding horizontal displacements at L_x and L_{x2} are presented in Figure 4.6. Effective control is obtained for $K_p = 10^{13}$ combined with either $K_d = 10^{12}$ or 10^{13}, whereas lower proportional gains lead to degraded performance and increased oscillations. In particular, the gain pair $K_p = 10^{12}$ and $K_d = 10^{12}$, which proved effective in the single-magnet strategy, fails to provide sufficient control in the double-magnet setup. This underlines that only higher gain values, such as those selected at the end of Chapter 4.2.1, ensure good performance in the extended strategy.

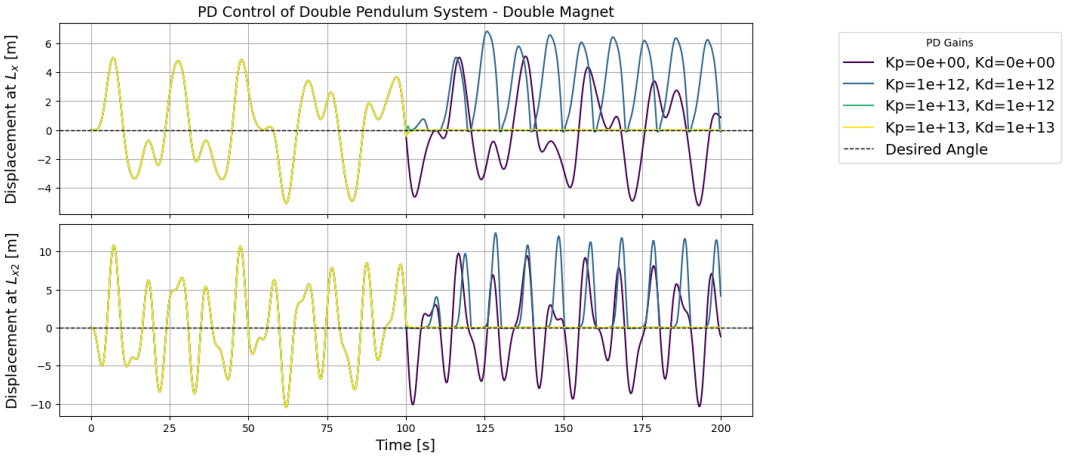

Figure 4.6: Double magnet control — Effect of PD gain values on horizontal displacements at L_x and L_{x2} under harmonic moment.

Overall, the gain pair $K_p = 10^{13}$ and $K_d = 10^{13}$ confirms its suitability for the extended double-magnet strategy and is therefore retained for further analysis. This combination achieves a balance between stability, accuracy, and efficiency, although it does so at the expense of increased system stiffness and damping, as previously discussed in Chapter 4.2.1.

With the control gains fixed, attention shifts to magnet placement, which also influences control performance. According to equations 4.3 and 4.6, both L_x and L_{x2} directly affect the moment arm over which the magnetic forces act, as well as the distance between the internal and external magnets (see Equation 4.1).

To evaluate placement efficiency, a brute-force parameter sweep is conducted across a range of physically feasible positions:

$$L_x \in [37\,\text{m},\ 62\,\text{m}] \quad \text{(lower half of the monopile)}$$
$$L_{x2} \in [2\,\text{m},\ 37\,\text{m}] \quad \text{(upper half of the monopile)}$$

The upper bound for L_x excludes the final meters of the monopile. Placing a magnet in this region would offer little benefit, as submerged external magnets are not considered in this study. Moreover, the strongest response occurs within the first 10 m of submersion, as shown earlier in Fig. 3.20. Hence, setting $L_x = 62$ m (out of a 74 m monopile) allows for control during this initial installation phase while maintaining a safety margin of a few meters from the water surface.

In addition to analyzing the rotational and horizontal displacements, another key indicator of effective control is the total dipole moment magnitude, $m_{\text{ext}}(t)$. A low value reflects reduced magnetic effort. Efficiency can be further assessed through the ratio of forcing moment output to dipole moment input, where higher values indicate a more effective use of the magnets.

To capture this, each configuration is evaluated using a performance index (PI), defined in Equation 4.8. The PI measures the moment delivered per unit of magnetic actuation, providing a direct measure of efficiency. In this formulation, M_{net} denotes the total moment produced by both magnets, while $m_{\text{t,tot}}$ represents the combined absolute magnitudes of the dipole moments generated by the PD controllers.

$$\text{PI}(t) = 100 \times \frac{|M_{\text{net}}(t)|}{|m_{\text{ext}}(t)|} \tag{4.8a}$$
$$M_{\text{net}}(t) = M_{m,1}(t) + M_{m,2}(t) \tag{4.8b}$$
$$m_{\text{t,tot}}(t) = |m_{t,1}(t)| + |m_{t,2}(t)| \tag{4.8c}$$

Figure 4.7 shows the PI evaluated for each magnet location combination. The optimal configuration occurs at $(L_{x2}, L_x) = (2, 62)$ m, maximizing the moment arm between the two magnets. Indeed, placing the magnets farther apart and near the extremes of the monopile enhances the couple effect, allowing higher moment generation with lower dipole effort. In contrast, poor performance is observed when both magnets are near the midpoint of the structure, where moment arm is shortest.

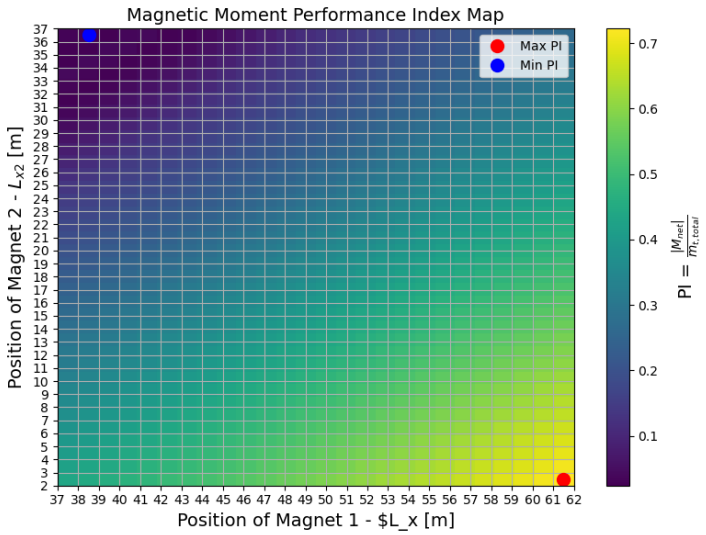

Figure 4.7: Performance index PI across combinations of magnet locations L_x and L_{x2} along the monopile.

The configuration that achieved the highest PI, $(L_{x2}, L_x) = (2, 64)$ m, is selected as a reference case. For comparison, a more conservative yet effective configuration, $(L_{x2}, L_x) = (2, 32,)$ m, is also considered. The choice of $L_x = 32$ m follows from subtracting the maximum submersion depth of 40 m from the monopile length, while leaving a safety margin of a few meters below the water surface. This setup ensures operational feasibility without requiring magnets submersion and allows the system to remain controllable at large depths. Including both configurations in the irregular wave simulations provides a balanced evaluation of efficiency versus practicality, while also enabling the assessment of how magnet positioning along the monopile influences control performance in realistic installation scenarios involving wave loading and varying submersion.

4.3. Control of the System Subjected to Wave Load

In the previous section, the controller gains and two representative placements for the magnets along the monopile were identified. Building on those findings, this section investigates the performance of the control strategy under a realistic irregular wave load. Since a single magnet was shown to be insufficient for controlling both rotation and displacement, the simulations now focus exclusively on a double magnet configuration.

The effectiveness of the magnetic control depends not only on the previously introduced parameters but also on other aspects of the system. In particular, the submersion length $\mathscr{L}$ plays a significant role. As discussed in earlier chapters, the hydrodynamic loading varies considerably during the installation process, and larger responses can demand higher control efforts. Another key geometric factor is the horizontal distance d between the external magnets and the monopile. This distance introduces a physical constraint, avoiding contact between the magnets, but also directly influences the magnetic moment described in Equation 4.3.

Figure 4.8 illustrates the relationship between the magnetic forcing and the dipole separation r, highlighting the nonlinear nature of this dependency. Since the distance d directly affects the separation r between the dipoles, the magnetic forcing, which scales with $1/r^4$, decreases rapidly. As a result, increasing d can reduce the magnetic forcing by more than 99%.

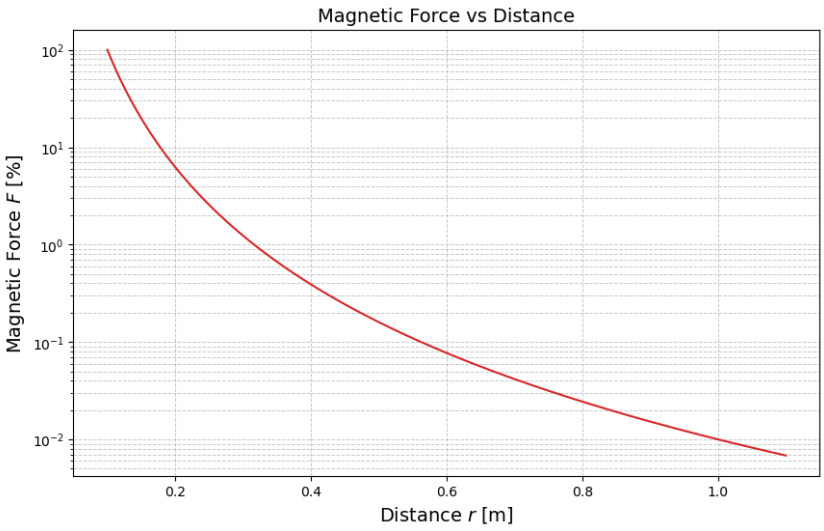

Figure 4.8: Influence of dipole separation d on magnetic interaction forcing

Table 4.2 summarizes the specific values selected for further analysis. These parameters are chosen to allow a comparative investigation of their effect on control performance during the installation process.

Table 4.2: Selected parameters for numerical simulations of double pendulum system subjected to wave load

Parameter	Symbol	Values used	Unit
Submersion length	$\mathscr{L}$	-10, -40	[m]
Magnet positions	$[L_x, L_{x2}]$	$[2, 32]$, $[2, 62]$	[m]
Horizontal magnet distance	d	0.25, 0.5, 1.0	[m]
Controller gains	$[K_p, K_d]$	$[1 \times 10^{13},\ 1 \times 10^{13}]$	[-]

The submersion lengths $\mathscr{L} = -10$ m and -40 m are selected based on the results from Chapter 3, representing the early and late stages of installation. These two conditions produce significantly different responses, making them particularly relevant for evaluating the controller's adaptability.

The magnet placement configurations $(2, 32)$ m and $(2, 62)$ m are introduced in Section 4.2.2. These combinations are designed to assess whether adding a magnet closer to the lower end of the monopile improves control during the initial phase, which typically experiences the highest dynamic response.

The horizontal spacing, d, between the external and monopile magnets was initially set at 0.5 m (see Tab.4.1). To assess its influence, two additional values, 0.25 m and 1 m, are considered. These values span a realistic design range and provide insight into how d affects both moment generation and magnetic stability. The smaller spacing, 0.25 m, is included because, as shown in Fig.4.8, reducing d allows for higher magnetic forcing with the same input. The larger spacing, 1 m, is examined to understand how increased separation impacts control performance while ensuring safety, as 0.25 m may be too close for practical implementation.

Finally, the PD controller gains K_p and K_d are fixed at 1×10^{13}. These values were determined through trial-and-error tuning in the simplified harmonic moment scenario in Chapter 4.2, where they showed satisfactory performance.

As in the harmonic forcing case, the effectiveness of the control is evaluated based on the ability of the angular displacements, θ_1 and θ_2, and the horizontal displacements at the magnet locations (L_{x2}, L_x) to reach the target position, ξ. Additionally, the magnetic dipole moment magnitude, the resulting moment on the monopile, and the magnetic field are examined to assess the feasibility, scalability, and practical implementation of the non-contact strategy. These results help quantify the control effort required and guide design decisions.

Regarding the magnetic field, it should be noted that the monopile's magnet dipole moment, $m_{c,x}$, is fixed at 1 Am^2. Controlling $m_{t,x}$ therefore effectively regulates the product $m_{t,x} \cdot m_{c,x}$ (see Equation 4.3), which dominates the overall magnetic interaction. In this analysis, $m_{c,x}$ is treated as equivalent to $m_{t,x}$ when computing $B_{t,x}$, yielding reasonable magnetic field values that would otherwise be excessively large.

To maintain clarity in the presentation of results, the analysis primarily focuses on the magnet at L_x and its influence on the second body's angular motion, θ_2, as this degree of freedom is directly affected by the applied loading. The remaining responses, particularly those associated with L_{x2} and θ_1, are not presented in this report since very similar results to the analyzed cases were obtained.

Based on the selected parameters, several configuration combinations are possible. These are listed in Table 4.3, which provides an overview of the simulation cases used to evaluate control performance under varying conditions.

Table 4.3: Possible configurations with selected parameters for numerical simulations of double pendulum system subjected to wave load

Cases	d [m]	K_p	K_d	$(L_x 2, L_x)$ [m]	$\mathscr{L}$ [m]
1	0.25	10^{13}	10^{13}	(2, 62)	-10
2	0.25	10^{13}	10^{13}	(2, 32)	-10
3	0.25	10^{13}	10^{13}	(2, 32)	-40
4	0.5	10^{13}	10^{13}	(2, 62)	-10
5	0.5	10^{13}	10^{13}	(2, 32)	-10
6	0.5	10^{13}	10^{13}	(2, 32)	-40
7	1.0	10^{13}	10^{13}	(2, 62)	-10
8	1.0	10^{13}	10^{13}	(2, 32)	-10
9	1.0	10^{13}	10^{13}	(2, 32)	-40

4.3.1. Effect of Submersion Length on Control Performance

The influence of submersion length on control performance is assessed by comparing Cases 5 and 6 in Tab. 4.3, which differ only in the submersion level: $\mathscr{L} = [-10, -40]$ m. These two cases are selected because the magnet positioning $(L_{x2}, L_x) = (2, 32)$ m is feasible at both depths. At a submersion length of -40 m, the alternative configuration $(L_{x2}, L_x) = (2, 62)$ m would require the magnets to be submerged, which falls outside the scope of this research. For consistency with the earlier time-domain simulations (see Tab. 4.1), the chosen cases have horizontal spacing $d = 0.5$ m.

The angular and horizontal displacements of the pendulum system subjected to wave load over time with different $\mathscr{L}$ are presented in Fig. 4.9. As for the previous cases, the control strategy is activated at $t = 100$ s.

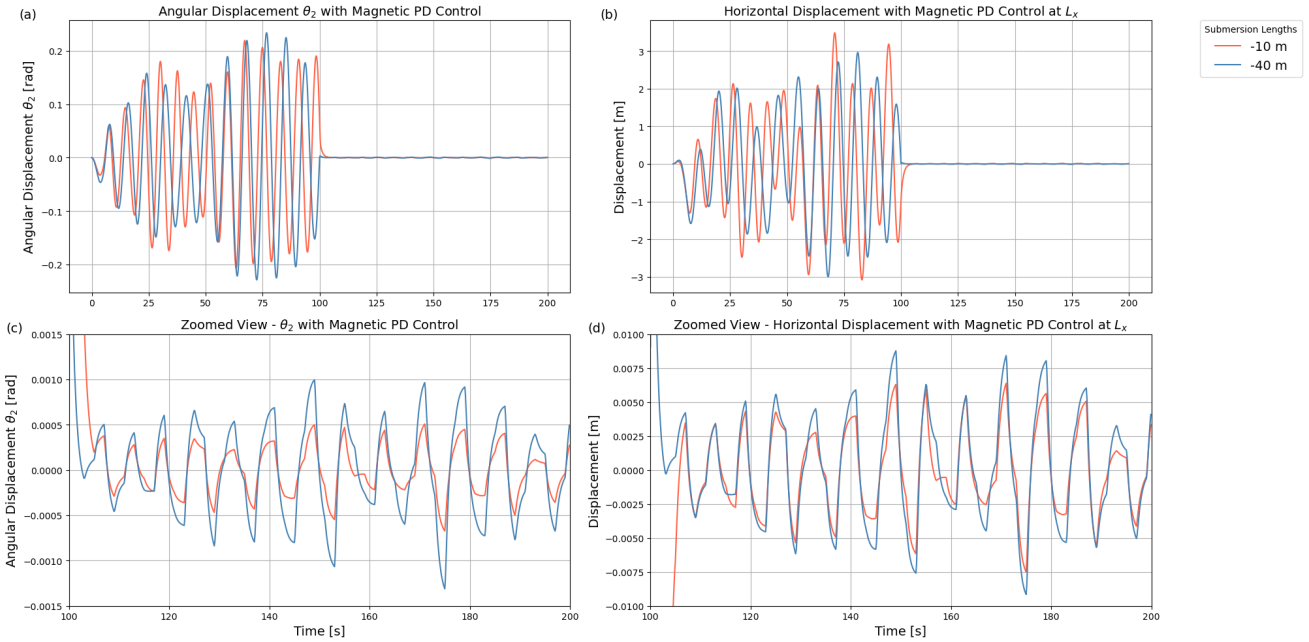

Figure 4.9: Responses of the controlled double pendulum for submersion lengths $\mathscr{L} = -10$ m and $\mathscr{L} = -40$ m: a) angular displacement θ_2; b) horizontal displacement at L_x; c) zoomed-in angular displacement θ_2 controlled response; d) zoomed-in horizontal displacement at L_x controlled response.

Despite the difference in submersion length $\mathscr{L}$, the responses of the system under control are remarkably similar. In both Cases, the system converges toward the desired equilibrium, demonstrating effective suppression of motion. This similarity probably arises from the initial dynamic behavior of the two configurations that are almost identical in the first 100 seconds. This trend can also be observed in the uncontrolled case shown in Figure 3.21 where the response for the -10 m submersion eventually grows larger after the 100 second mark. Overall, looking at the displacements responses, the control performance remains largely unaffected by the variation in submersion length.

Furthermore, these results suggest that the magnet placement $(L_{x2}, L_x) = (2, 32)$ m, is sufficient for effective control across different submersion lengths. This implies that the use of lower magnet placements (higher value of L_x) may not be necessary, at least for this range of depths. Consequently, adding a third magnet at 62 m along the monopile might only be required for safety redundancy rather than for performance enhancement.

Further insight is provided by Fig. 4.10, which reports the control moments, magnetic dipole moments, and magnetic fields generated during the simulations. In both Cases 5 and 6, the control moment reaches values on the order of 10^7 Nm, corresponding to forces of about 10^5 N. This outcome is consistent with expectations, as the control must counteract wave loads of similar magnitude (see Chapter 3.3). The dipole moment $m_{t,x}$ reaches values up to 10^{10} Am^2, producing maximum magnetic fields of around 500 mT. The control related results for both submersion lengths are largely overlapping, except at the peaks, where the -40 m configuration exhibits slightly higher values, particularly for the control moment and dipole moment, where the large axis range highlights the significance of even relatively small changes.

Plateau regions appear in the magnetic and dipole moment curves near their peaks, suggesting numerical issues likely linked to non-linearities in the magnetic interaction. Nevertheless, the overall waveforms maintain a sinusoidal character, providing a representative picture of the magnitudes involved.

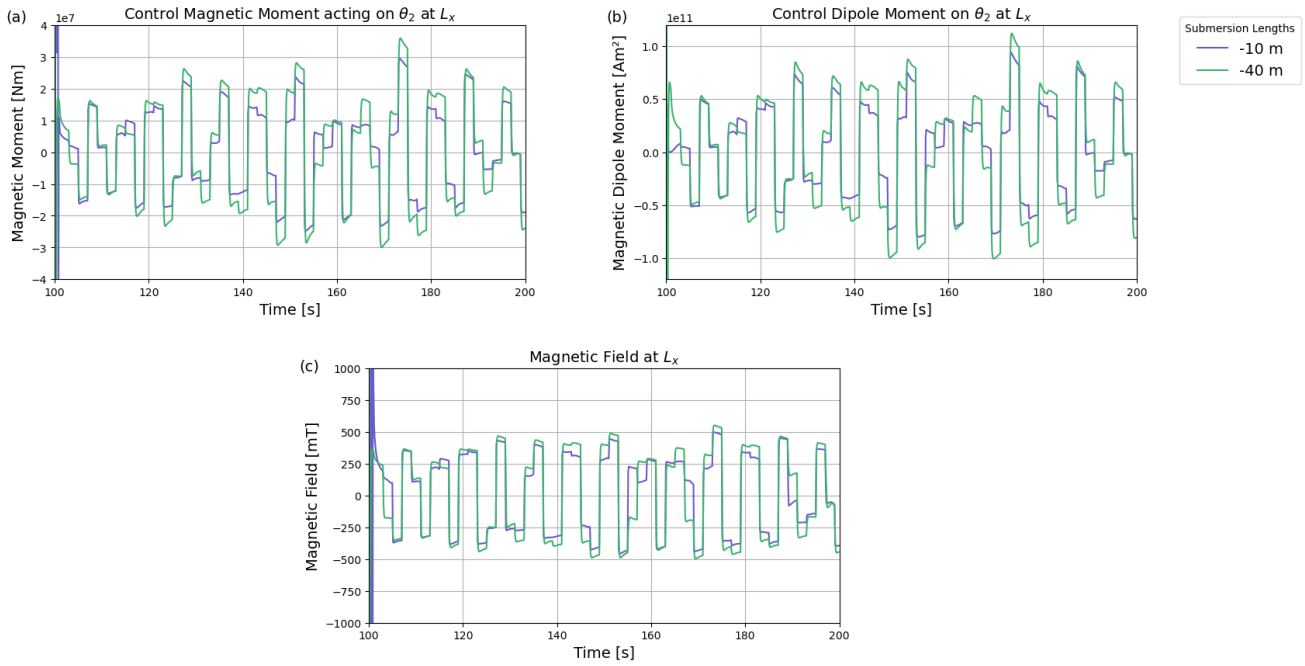

Figure 4.10: Magnetic control strategy for submersion lengths $\mathscr{L} = -10$ m and $\mathscr{L} = -40$ m: a) magnetic moment generated by the control; b) dipole moment generated by the control; c) magnetic field required for generating $m_{t,x}$.

Although the magnetic fields required to generate such high forcing are relatively large, they remain reasonable in light of the system scale and the necessity of fully counteracting wave loads. Similar magnitudes are also encountered in practice: Domingos et al. [5] reports that tugger line stiffness for highly restrained wind turbine components can reach 10^6 N/m, resulting in moments of a similar order depending on lever arm and displacement. Likewise, Ren et al. [31] shows that forces of around 65 kN are typical for tugger lines, lower than the simulated values but of comparable scale. It should be noted, however, that these studies consider lighter components, such as blades of about 200 tons, whereas the present system involves a 1000 ton monopile. Thus, the use of large magnetic fields through non-contact actuation remains feasible and acceptable.

In summary, the results demonstrate that the proposed double-magnet control strategy is robust to changes in submersion length, and that effective control can be achieved without additional magnets or reconfiguration. Moreover, the similarities in early-time response between depths suggest that a more complex magnet setup may not be required, especially if the control is initiated promptly.

4.3.2. Effect of Magnet Positioning on Control Performance

Following the observation that the magnet positioning at $(L_{x2}, L_x) = [2, 32]$ m is sufficient for controlling the system across different submersion lengths, this subsection investigates whether higher placements could offer performance advantages. The analysis focuses on a fixed submersion depth of $\mathscr{L} = -10$ m and compares the control response for two configurations with the same horizontal offset $d = 0.5$ m: $(L_{x2}, L_x) = (2, 32)$ m and $(2, 62)$ m, corresponding to Cases 4 and 5 in Table 4.3.

The idea behind testing the higher placement $(2, 62)$ m stems from earlier findings in Chapter 3, where the first 10 m of the pendulum length submerged contributed most significantly to system dynamics. A longer lever arm, as provided by the lower magnet, could potentially enhance control.

Fig. 4.11 show that both magnet configurations effectively stabilize the system, with angular and horizontal displacements converging closely to the desired equilibrium ($\xi = 0$). At $(L_{x2}, L_x) = (2, 32)$ m higher oscillations are present compared to the other case. However, the differences in response magnitude between the two setups are minimal, confirming that both magnet pairs are capable of achieving the control objective.

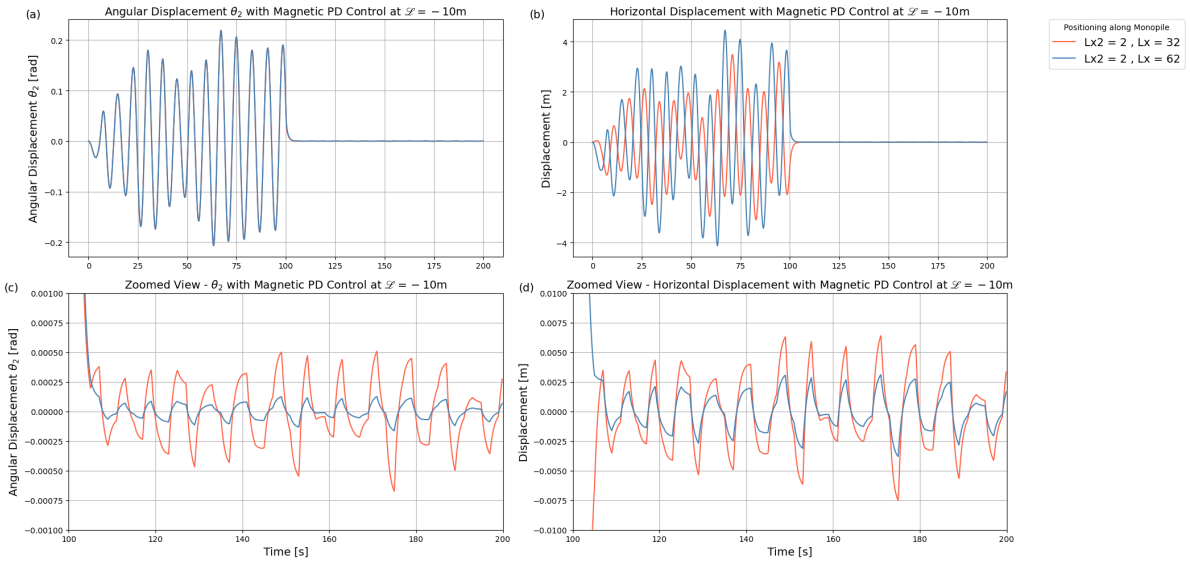

Figure 4.11: Responses of the controlled double pendulum for $(L_{x2}, L_x) = [2, 32]$ m and $[2, 62]$ m: a) angular displacement θ_2; b) horizontal displacement at L_x; c) zoomed-in angular displacement θ_2 controlled response; d) zoomed-in horizontal displacement at L_x controlled response.

A clearer distinction emerges in the actuation effort required. As shown in Fig. 4.12, the dipole moment generated by the $(2, 62)$ m configuration has lower peaks than that of the $(2, 32)$ m setup, remaining in the order of 10^{10} Am^2 but toward its lower range. In contrast, the control moments essentially coincide, indicating that magnet positioning has little influence on this response. The magnetic field also shows similar trends for both configurations, with the $(2, 62)$ m case requiring a lower field due to its reduced dipole moment. These findings imply that equivalent control performance can be achieved with reduced magnetic effort when the magnets are placed closer to the bottom edge of the monopile. This highlights the advantage of a longer couple arm, which decreases the magnetic strength needed for effective control.

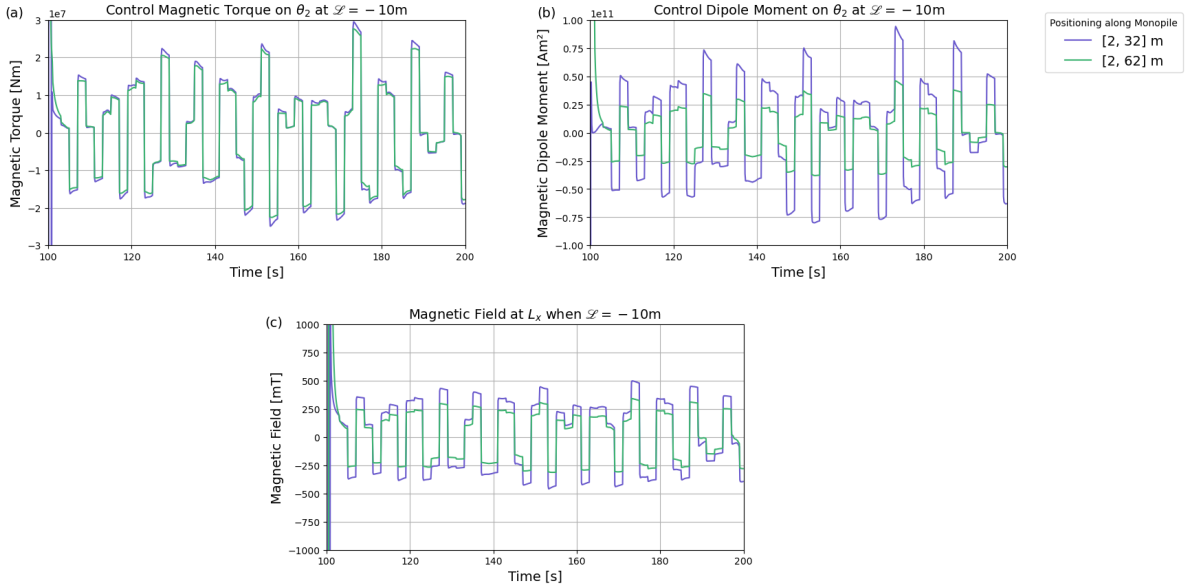

Figure 4.12: Magnetic control strategy for positioning $(L_{x2}, L_x) = (2, 32)$ m and $(2, 62)$ m: a) magnetic moment generated by the control; b) dipole moment generated by the control; c) magnetic field required for generating $m_{t,x}$.

These findings align with the brute force analysis presented earlier in Fig. 4.7, where the $(2, 62)$ m

configuration was identified as one of the most effective setups for magnetic control. Although the system responses are nearly identical between the two cases, the reduced actuation effort makes the lower positioning a more efficient and preferable choice. In particular, placing the magnets at $(2, 62)$ m achieves the same level of control with lower dipole moment and magnetic field requirements, thereby enhancing the overall energy efficiency of the control strategy.

4.3.3. Effect of Horizontal Distance d on Control Performance

This subsection investigates the influence of the horizontal distance d between the external and the monopile-mounted dipole magnets on the control performance. There are two possible approaches to understand the influence of this parameter: varying the submersion length $\mathscr{L}$ and varying the magnet positions along the monopile (L_{x2}, L_x).

For different submersion lengths, using the positioning of $(L_{x2}, L_x) = (2, 32)$ m, the Cases examined from Tab. 4.3 correspond to Configurations 2, 5, and 8 for $\mathscr{L} = -10$ m and to Configurations 3, 6, and 9 for $\mathscr{L} = -40$ m. For different positioning of the magnets, specifically at a submersion length of $\mathscr{L} = -10$ m, the configurations considered include Cases 1, 4, and 7 for $(L_{x2}, L_x) = (2, 62)$ m, and Cases 2, 5, and 8 for $(L_{x2}, L_x) = (2, 32)$ m, according to Table 4.3.

Fig. 4.13 and Fig. 4.14 illustrate the angular displacement of the second body (θ_2) and the horizontal displacement of the system at $L_x = 32$ m, respectively. From these plots, it is evident that increasing the distance d results in reduced control performance for both submersion depths. Nonetheless, even at the largest distance of $d = 1$ m, the horizontal displacement remains within 0.5 m and within the small angle approximation, indicating that the control strategy remains effective across the distances tested.

Comparing the two submersion levels, the shallower configuration at 10 m generally exhibits slightly lower angular displacement and overall movement, consistent with earlier findings in Chapter 4.3.1. Hence, the submersion levels, also in the case where the horizontal distance between the magnets is increased, have negligible effect in the responses of the system.

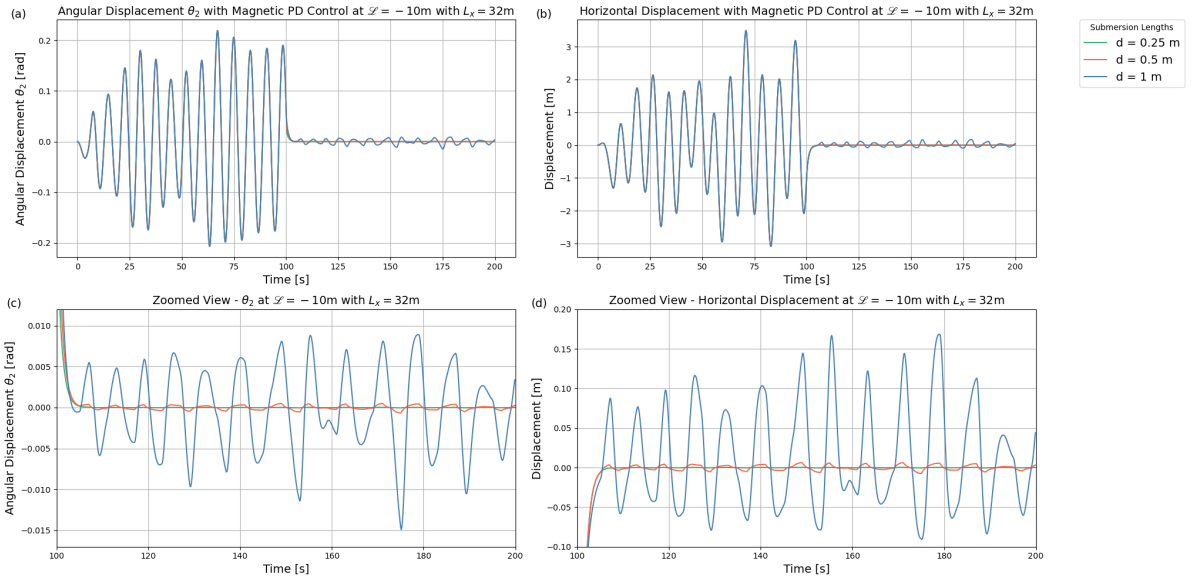

Figure 4.13: Responses of the controlled double pendulum for $d = [\ 0.25\ ,\ 0.5\ ,\ 1\ ]$ m at submersion length $\mathscr{L} = -10$ m: a) angular displacement θ_2; b) horizontal displacement at $L_x = 32$ m; c) zoomed-in angular displacement θ_2 controlled response; d) zoomed-in horizontal displacement at $L_x = 32$ m controlled response.

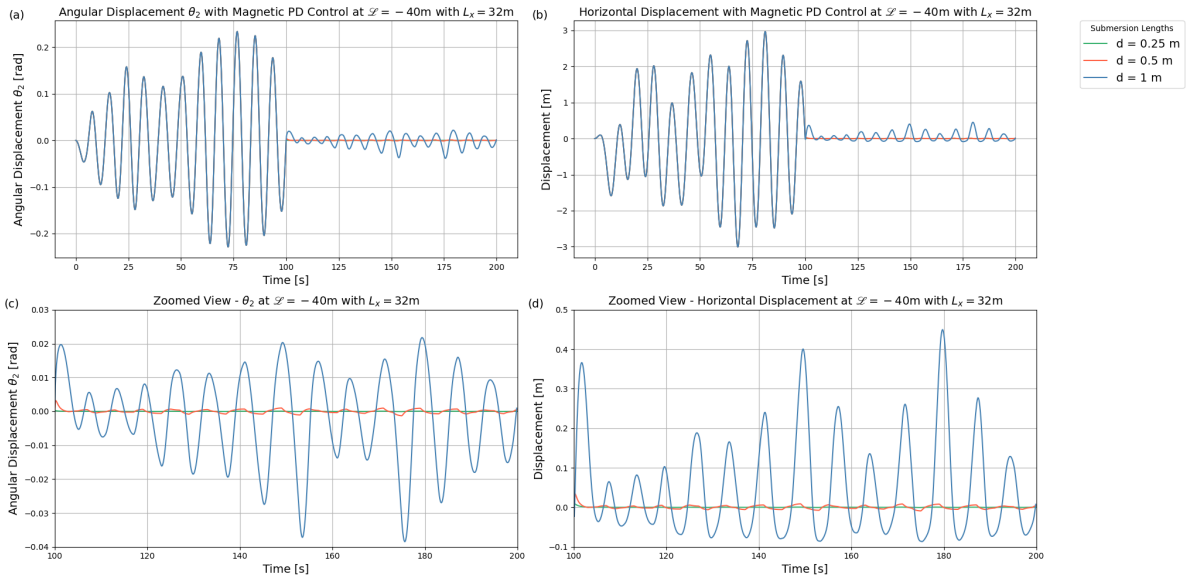

Figure 4.14: Responses of the controlled double pendulum for $d = [\ 0.25\ ,\ 0.5\ ,\ 1\ ]$ m at submersion length $\mathscr{L} = -40$ m: a) angular displacement θ_2; b) horizontal displacement at $L_x = 32$ m; c) zoomed-in angular displacement θ_2 controlled response; d) zoomed-in horizontal displacement at $L_x = 32$ m controlled response.

Similarly, when comparing the positioning effect on the displacement responses (see Fig. 4.13 and 4.15), effective control is achieved across all configurations, regardless of the values of d and (L_{x2}, L_x). Nevertheless, increasing d makes the system response more oscillatory and leads to larger deviations from the desired equilibrium position $\xi = 0$. This trend is particularly evident in the displacement plots, where stronger fluctuations appear for larger horizontal distances, such as $d = 1$ m.

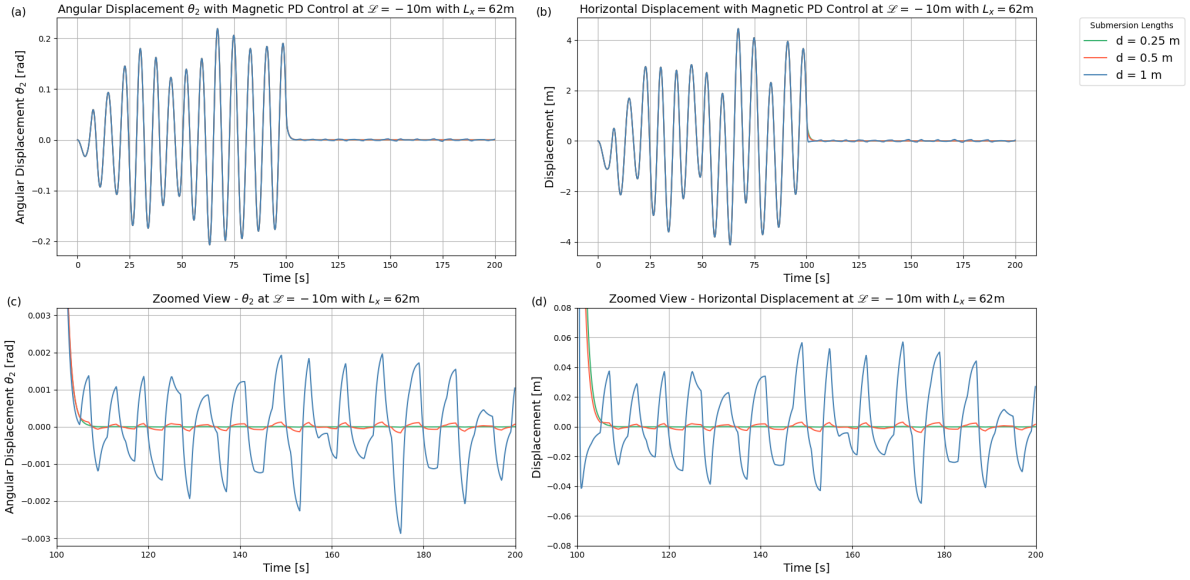

Figure 4.15: Responses of the controlled double pendulum for $d = [\ 0.25\ ,\ 0.5\ ,\ 1\ ]$ m at submersion length $\mathscr{L} = -10$ m: a) angular displacement θ_2; b) horizontal displacement at $L_x = 62$ m; c) zoomed-in angular displacement θ_2 controlled response; d) zoomed-in horizontal displacement at $L_x = 62$ m controlled response.

A direct comparison of the two magnet placements highlights a performance advantage for the configuration with $L_{x2} = 62$ m. The interaction between magnet positioning and the horizontal distance d indicates that control accuracy decreases with larger d values and smaller L_x. For instance, at $d = 1$ m, the displacement for $L_x = 62$ m is nearly half that observed with $L_x = 32$m. This finding is consistent

with the conclusions of Chapter 4.3.2, where lower magnet placements in the monopile were shown to improve control effectiveness through the longer lever arm effect. Moreover, the negative impact of a large d is partially mitigated when the magnets are placed at higher L_x values (i.e., lower down the monopile).

Further insight is gained by examining the magnetic actuation requirements. Fig. 4.16 and Fig. 4.17 show the time histories of the magnetic dipole moment $m_{t,x}$ and the resulting moment for each distance d at the two submersion lengths. The effect of submersion length becomes more pronounced at larger d. For example, at $d = 1$ m, the required dipole moment at -40 m is nearly double that at -10 m. In contrast, when magnets are placed closer together, the difference in magnetic effort between submersion depths becomes smaller and smaller.

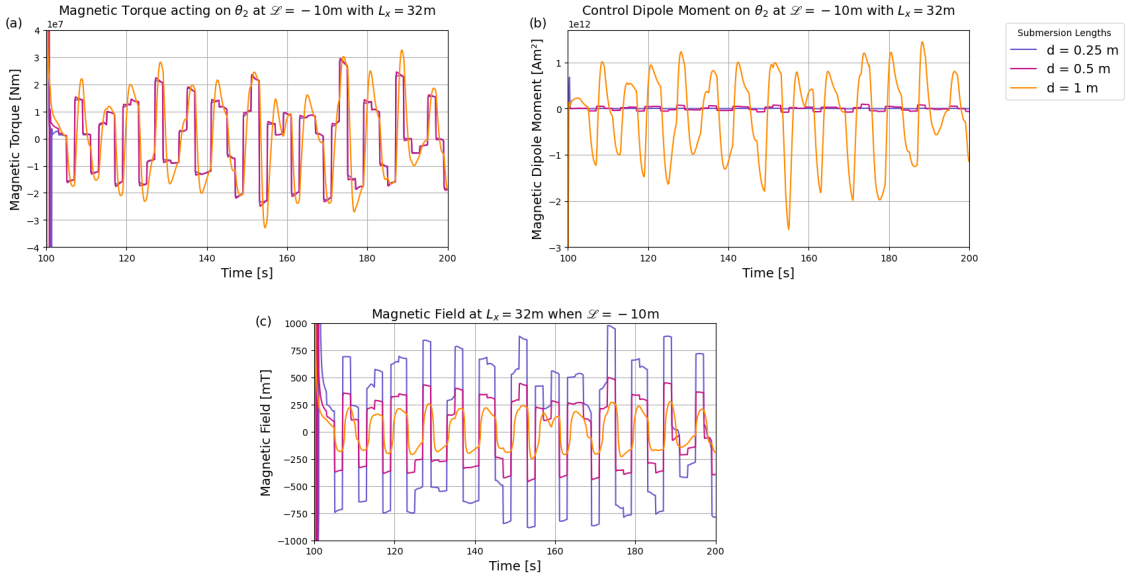

Figure 4.16: Magnetic control strategy for $d = [\ 0.25\ ,\ 0.5\ ,\ 1\ ]$m at $L_x = 32$ m for submersion length $\mathscr{L} = -10$ m: a) magnetic moment generated by the control; b) dipole moment generated by the control; c) magnetic field required for generating $m_{t,x}$.

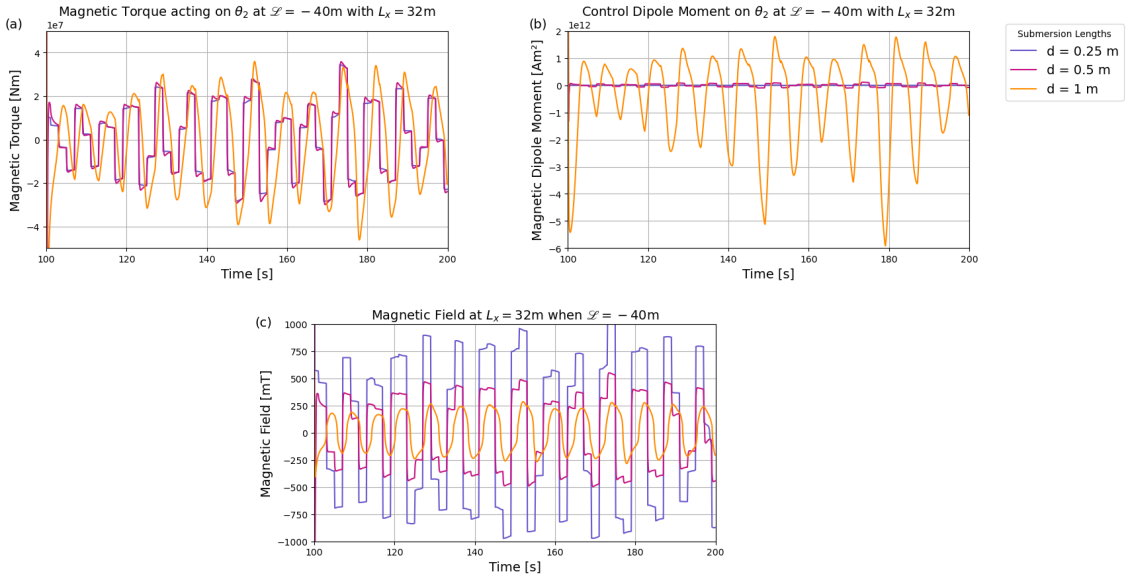

Figure 4.17: Magnetic control strategy for $d = [\ 0.25\ ,\ 0.5\ ,\ 1\ ]$m at $L_x = 32$ m for submersion length $\mathscr{L} = -40$ m: a) magnetic moment generated by the control; b) dipole moment generated by the control; c) magnetic field required for generating $m_{t,x}$.

Changing the magnet positioning produces effects similar to those observed for different submersion lengths, as shown by comparing Fig. 4.16 and Fig. 4.18. Since the external load remains constant, the magnitude of the generated moments is largely unaffected by variations in d or by the magnet placement. However, maintaining this same moment magnitude requires progressively larger dipole moments as d increases, consistent with the trends identified for varying submersion lengths.

Both variations in positioning (L_{x2}, L_x) and in submersion length $\mathscr{L}$ show a clear trend: as the horizontal distance d increases, the required magnetic dipole moment rises sharply. Specifically, values are on the order of 10^9 A·m^2 for $d = 0.25$ m, increase to 10^{10} A·m^2 at $d = 0.5$ m, and reach up to 10^{12} A·m^2 for $d = 1$ m. This escalation occurs because a larger d increases the effective separation r between dipoles, forcing the controller to compensate by amplifying the dipole moment. Given that the magnetic moment scales with $1/r^4$, even modest increases in d lead to a steep, exponential rise in the required $m_{t,x}$ to sustain the same moment, as illustrated in Fig. 4.8.

Additionally, the increase of L_x generally leads to lower dipole moment requirements. However, as d becomes smaller, the difference in performance between the two positioning configurations diminishes.

Overall, this implies that smaller values of d enable the same control moment to be generated with substantially smaller dipole moments, highlighting the higher efficiency of closer magnet placements. However, these benefits come with trade-offs: high magnetic field, lower accuracy and lower safety.

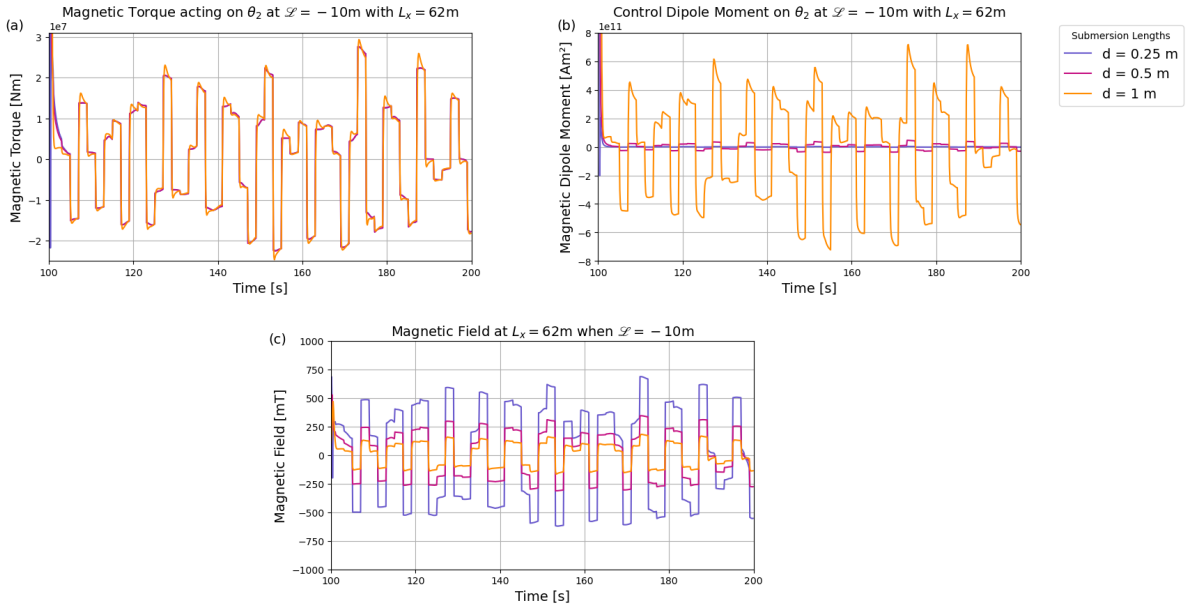

Figure 4.18: Magnetic control strategy for $d = [\ 0.25\ ,\ 0.5\ ,\ 1\ ]$m at $L_x = 62$ m for submersion length $\mathscr{L} = -10$ m: a) magnetic moment generated by the control; b) dipole moment generated by the control; c) magnetic field required for generating $m_{t,x}$.

Having a low dipole moment $m_{t,x}$ is essential to ensure that the non-contact control strategy remains feasible. However, this requirement must be balanced against the magnetic field strength, which also needs to remain within the limits of what existing magnets can generate. As shown in Equation 2.21, the field $B_{t,x}$ is highly sensitive to the dipole separation r. From the magnetic field plots (see Fig. 4.16 c), 4.17 c) and 4.18 c)), it becomes clear that small values of d result in low dipole moments but extremely high magnetic fields, which exceed the capabilities of magnets with such dipole strengths. Conversely, at larger distances such as $d = 1$ m, the magnetic field falls within more realistic limits, but the required dipole moment becomes excessively large, demanding magnets of impractical strength or size. This trade-off highlights the need to find an appropriate balance between dipole moment and magnetic field to achieve both efficiency and feasibility in practice.

Furthermore, the forcing moment time histories at smaller d values, particularly $d = 0.25$ m and $d = 0.5$ m, display irregular, plateau-like shapes due to the strong nonlinear dependence on the separation

distance r in the magnetic moment expression (Equation 2.25). These plateaus generally indicate numerical issues, making the response less accurate. In contrast, the $d = 1$ m case produces a smoother, more sinusoidal response, which is also more reliable. A similar trend appears with magnet positioning: while increasing L_x does not significantly change the overall moment magnitude, higher placements (e.g., $L_x = 62$ m) tend to produce less smooth profiles and stronger nonlinearities. This is evident when comparing the $d = 1$ m cases, where $L_x = 32$ m yields a more accurate sinusoidal moment curve than $L_x = 62$ m.

It is also important to mention that, in real-world applications, smaller distances between magnets increase the risk of physical interaction or instability which can increase danger during installation operations. Moreover, while this is not reflected in the idealized dipole-dipole interaction model used in this research, such stability constraints could limit the practical use of very low d values which could lead the magnets to be too close to each other or to the vessel.

In summary, reducing the horizontal distance d between the magnets enhances control efficiency by lowering the required magnetic dipole moment. However, this advantage comes with drawbacks such as stronger nonlinear effects, potential instability, and safety concerns when magnets are placed too close. At larger distances, the system requires higher dipole moments. However, the moment responses become smoother and more reliable, and the sensitivity to submersion depth is reduced. This makes the configuration more robust in practice. Magnet positioning also plays a key role: while higher placements can improve displacement control, particularly at larger d, they tend to introduce numerical nonlinearities. The magnetic field behavior further complicates this balance: at high d, the field drops to more realistic levels but would require impractically large dipole moments to generate, while at low d the dipole moment is feasible but the resulting field becomes unrealistically high. Thus, achieving effective magnetic actuation requires carefully balancing d and L_x to minimize dipole effort and field demands while avoiding excessive nonlinearity or impractical operating conditions.

4.4. Best Configuration for Non-Contact Control of the System subjected to Wave Loads

Based on the outcomes of the simulation of the different Cases from Tab. 4.3, the best parameters for achieving efficient magnetic control of the double pendulum system, among the one considered, have been identified. These parameters are summarized in Tab. 4.4. The configuration includes two strategically positioned magnets along the monopile, with a horizontal spacing of $d = 0.5$ m. The magnets are placed at $L_{x2} = 2$ m and $L_x = 32$ m, while the PD controller gains are set to $K_p = 1 \times 10^{13}$ Nm/rad and $K_d = 1 \times 10^{13}$ Nm·s/rad.

Table 4.4: Control strategy parameters for double pendulum system subjected to wave loads.

Parameter	Symbol	Value	Units
Horizontal distance between magnets	d	0.5	m
Magnet position 1	L_x	32	m
Magnet position 2	L_{x2}	2	m
Proportional gain	K_p	1×10^{13}	[-]
Derivative gain	K_d	1×10^{13}	[-]

To validate the effectiveness of this configuration, a final time-domain simulation was carried out. In this simulation, the monopile undergoes a staged lowering process: starting at $t = 100$ s, it is submerged in increments of 5 meters every 10 seconds, progressing from a submersion depth of $\mathscr{L} = -5$ m to $\mathscr{L} = -40$ m. This configuration is similar to the response showed in Fig. 3.24 at the end of Chapter 3.5.2. The control is activated after 100 sec when the monopile is already partially submerged with $\mathscr{L} = -5$ m.

Fig. 4.19 shows the angular displacements of θ_1 and θ_2, as well as the corresponding displacements measured at the cable end and at L_x, respectively. The results confirm that the control strategy performs well across all submersion depths. The angular displacements remain small, demonstrating stable and precise control even under increasing hydrodynamic loading.

It is also evident from the plots that as the monopile is lowered and submersion depth increases, the dynamic response becomes more pronounced. This is expected, as a greater submerged length leads to higher actuation from the control system as seen in Chapter 4. Despite this, the PD controller maintains effective performance, highlighting the robustness of the selected configuration.

An interesting observation is that, before control, the displacement associated with θ_1 exceeds that of θ_2. This difference arises from the location at which the displacements are measured. Since the response is dominated by the second mode, θ_1 and θ_2 are out of phase, causing the region near L_x to remain closer to its desired position due to the monopile's inclination. For reference, see Fig. **??**.

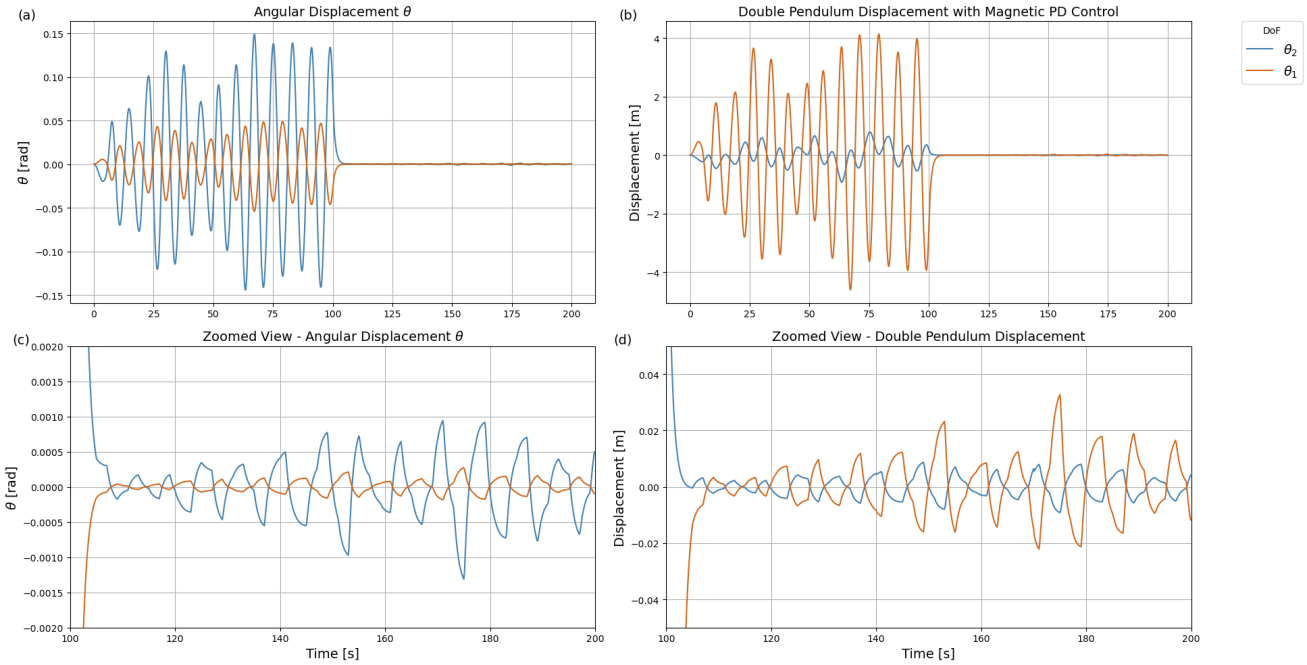

Figure 4.19: Responses of the controlled double pendulum for θ_1 and θ_2 with varying submersion length: a) angular displacements ; b) horizontal displacements at $L_x = 32$ m; c) zoomed-in angular displacements controlled response; d) zoomed-in horizontal displacement at $L_x = 32$ m controlled response.

The control efforts at both magnet locations (L_x and L_{x2}) are shown in Fig. **??**, including the generated moments, dipole moments, and magnetic fields for θ_2.

The results confirm that the control strategy remains effective across all submersion depths. The peak moment for θ_2 is around 10^7 Nm, while at L_{x2} it is approximately 10^6 Nm. This difference reflects the shorter lever arm and proximity of the second magnet to the rotation axis, which naturally limits its contribution. These values are consistent with the moments that must be counteracted from the wave loading. The plots also reveal that the two moments are always opposite, forming a couple as expected.

Both the dipole moment and magnetic field plots follow the system's beating pattern. Interestingly, despite the lower torque at L_{x2}, the required dipole moments and magnetic fields are higher. This highlights the critical role of lever arm length in the efficiency of the control strategy.

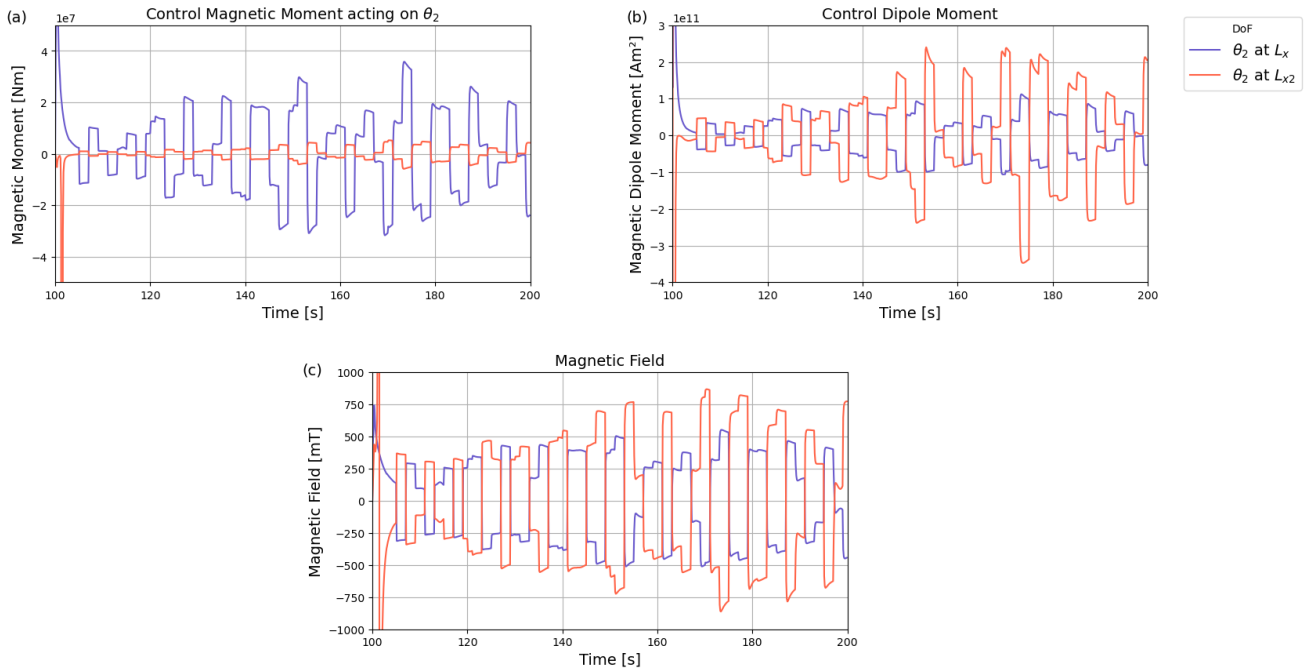

Figure 4.20: Magnetic control moment and magnetic dipole moment for θ_2 at positions L_x and L_{x2}.

Overall, the magnetic fields and dipole moments required at both magnet positions remain very high, highlighting the physical challenges of achieving full control during monopile installation. The results show that such control strategies can indeed mitigate wave-induced responses, but with current technology, a full-control approach may not be practical. A mitigation-oriented strategy is therefore more realistic. This research offers a valuable starting point for developing magnetic control systems for offshore structural components and exploring more efficient implementations.

5

Conclusion and Discussion

This thesis investigated the use of magnetic, non-contact control strategies to stabilize a monopile during offshore installation. A dynamic model of the crane–monopile system was developed using a double-pendulum representation, capturing wave loading, progressive submersion, and nonlinear magnetic effects. The system's behavior was analyzed in both the frequency and time domains to understand its response under realistic installation conditions.

A proportional–derivative (PD) controller was then designed to generate dipole–dipole forces that counteract wave-induced motion. Time-domain simulations were carried out for multiple magnet positions, spacings, and dipole moments to identify configurations that achieve effective stabilization while minimizing actuation effort.

The following sections present and discuss the main findings of this work, explicitly addressing the main research question and sub-questions introduced in Chapter 1.6. The conclusions are drawn from the results of Chapter 3, which analyzed the behavior of the partially submerged monopile, and from Chapter 4, which evaluated the magnetic control strategy.

5.1. Research Conclusions

The central research question of this thesis is the follwoing:

What is an efficient non-contact magnetic control strategy of a partially submerged monopile subjected to wave loads?

To address this question, the investigation was structured around two key themes: the influence of submersion on the system's dynamic behavior and the development of a magnetic control strategy. Each area was explored through specific sub-questions, helping to build a clearer picture of the key factors that influence the effectiveness and feasibility of using magnetic forces for non-contact control.

How does partial submersion affect the dynamic properties of a monopile during installation?

The system considered in this study models the monopile installation process using a planar double pendulum. This consists of a rigid rod representing the crane cable and a rigid hollow cylinder representing the monopile. Assuming rigidity and applying the small-angle approximation allows for linearization of the equations of motion, focusing solely on the system's two rotational degrees of freedom and how they are influenced by wave loading and submersion effects.

Chapter 3 details the construction of the dynamic model. Wave loads are introduced using Airy wave theory, and hydrodynamic forces due to submersion are modeled using Morison's equation. In this formulation, two main variables drive the hydrodynamic load: the horizontal water particle velocity and the structural oscillation of the submerged monopile. Both variables vary with time and submersion depth, which introduces submersion effects into the system's dynamics. It is important to mention that,

Morison's equation is best suited for slender structures, whereas monopiles generally have a relatively large diameter. However, a parameter sensitivity analysis shows that variations in the assumed radius do not produce significant changes in the system's dynamic response. Thus, although the assumption of a small radius is not entirely precise, it remains justified and sufficiently accurate for the objectives of this study.

One key feature of Morison's equation is its dependency on structural velocity, meaning that the monopile's motion influences the hydrodynamic load it experiences. This results in two dynamic effects: an added mass term that modifies the system's inertia and affects the mass matrix, and a quadratic drag term that provides a natural damping effect during submersion. As a result, the system's dynamic behavior changes continuously with submersion length.

To investigate how submersion alters the system's inherent dynamics, an eigenvalue analysis was conducted in the absence of flow. This allowed for the study of how natural frequencies and mode shapes vary with increasing submersion. The results showed that the added mass, representing the surrounding water particles carried along with the structure, causes both natural frequencies to decrease with submersion length. This effect is particularly significant for the second natural frequency, as the monopile (second body) is directly in contact with water. More in detail, it drops from an initial frequency of 0.174 Hz to approximately 0.114 Hz, with a steep reduction observed in the first $-10 \sim -15$ meters, followed by stabilization around -40 meters depth. This rapid frequency shift near the surface is important, as real offshore conditions are characterized by irregular wave spectra that can excite resonant modes.

The corresponding mode shapes exhibit expected behavior: the first mode shows in-phase rotation of both bodies, and the second mode shows out-of-phase motion. While submersion does introduce minor shape changes, the overall mode characteristics remain consistent.

To simulate realistic environmental forcing, irregular waves were introduced using the JONSWAP spectrum. These irregular waves produce time varying forces converted into moments in the model, accounting for both drag (proportional to horizontal water particle velocity) and inertia (proportional to acceleration). Since both are depth dependent, the magnitude of excitation varies with submersion. Near the surface (first -10 meters below water line), acceleration and velocity peaks are highest. The resulting cumulative moment initially increases due to higher surface-level accelerations and longer moment arms, then plateaus as contributions from deeper layers diminish. Inertial forces dominate the loading, reaching magnitudes around 10^7 Nm compared to 10^6 Nm from drag.

Due to the nonlinear drag term, time-domain simulations are required. Without drag, the system's response exhibits unrealistic, unbounded growth due to resonance. Including drag leads to stable oscillations, with angular displacements of both bodies remaining below approximately 0.2 rad, validating the small-angle approximation. As expected, the monopile's displacement is generally larger than that of the cable, given the direct application of wave loads on the former and only indirect excitation of the latter via coupling.

The simulation confirms that the system's response is weakest at deeper submersion levels (-40 m) and strongest near the surface (-10 m). It is worth noting that the added mass coefficient undergoes its largest variation in the first -5 meters of submersion, a critical zone during installation.

Additionally, all time-domain responses display beating phenomena, indicating the presence of closely spaced frequencies excited by the wave spectrum. A Fast Fourier Transform (FFT) analysis confirms that the response is primarily governed by frequency components near the system's second natural frequency, making this the most likely resonance region during real operations.

In conclusion, both the eigenvalue and time-domain analyses demonstrate that the monopile's dynamic response is sensitive to submersion depth. The most critical zone appears near the surface, where natural frequencies shift rapidly, excitation forces are strongest, and added mass effects are most variable. Interestingly, the system's initial response remains similar across different submersion levels, with significant differences becoming apparent only when the responses approach the transient phase of motion. This observation has important implications for the timing and control of the installation process.

How does variation in submersion level influence the control of the monopile throughout the installation stage?

This research implements a control strategy based on dipole-dipole magnetic interactions regulated by a PD controller, which generates counteracting moments to mitigate the effects of wave loads and submersion forces acting on the monopile. The controller operates by measuring the displacement error from the equilibrium position (defined at $x = 0$) and modulates the external dipole moment $m_{t,x}$ accordingly. Since the monopile's magnet dipole moment $m_{c,x}$ is fixed at 1 Am^2, controlling $m_{t,x}$ effectively controls the product $m_{t,x} \cdot m_{c,x}$, which contributes substantially to the overall magnetic interaction. This approach allows the PD controller to generate both repulsive and attractive magnetic forces depending on the monopile's displacement, enabling the application of the necessary magnetic moments to counteract wave-induced motion. These magnetic forces affect both rotation directions of the system, causing one moment that couples the two motions and another that acts directly on the second part of the system.

Controller gains K_p and K_d were calibrated using a simplified harmonic moment input to reduce computational cost and facilitate parameter tuning. Both gains were set at 10^{13}, a configuration that proved effective for both single and double magnet arrangements. Time-domain simulations demonstrated that a double magnet configuration offers superior control, particularly in managing angular displacements. This improvement arises because a single magnet's effect is localized, whereas multiple magnets distributed along the monopile enable more comprehensive control of both displacement and rotation. This advantage of non-contact magnetic control contrasts with traditional installation methods, which typically apply control forces at a single point, similar to the single magnet scenario.

Time-domain simulations with the wave load were conducted at two representative submersion depths, $\mathscr{L} = -10$ m and -40 m, corresponding to early and later installation stages identified as critical through earlier analyses. As the monopile is progressively lowered, the cable length l increases correspondingly, modeling the actual installation dynamics.

Despite the disparity in submersion depth, system responses under control were notably consistent across both cases. In each scenario, the monopile's motion converged toward the desired equilibrium position, demonstrating the controller's robust performance. While the response at -10 m showed a slight increase in displacement beyond 100 seconds, the overall effectiveness of the control was only marginally reduced at the deeper submersion of -40 m.

Analysis of control moments and magnetic dipole moments revealed similar magnitudes between the two submersion depths: moments reached on the order of 10^7 Nm, and dipole moments hovered near 10^{10} A m^2. The corresponding magnetic field also remained comparable across submersion lengths, with peak values around 500 mT. The temporal profiles of these quantities exhibited plateau regions near their peaks, reflecting the nonlinear nature of magnetic moment generation, while still preserving the characteristic sinusoidal waveform.

The comparable initial responses at both submersion lenghts explain the similarity in control efforts observed early in the simulation. However, considering that actual installation procedures may extend up to thirty minutes, it is reasonable to expect that differences in system response will grow over time, with deeper submersion increasingly impacting control performance. This aligns with physical intuition, as greater submersion entails stronger interactions between the monopile and the surrounding water, influencing the hydrodynamic forces acting on the structure.

What magnitude of magnetic forces is necessary to enhance the control of the monopile during installation offshore?

To determine the magnitude of magnetic forces necessary for effective monopile control during offshore installation, Chapter 4 explored various control scenarios and configurations, including changes in submersion length, the horizontal distance between dipoles, and the positioning of double magnets along the monopile. Despite these variations, the magnitude of the control moment consistently remained on the order of 10^7 Nm. Due to the inherent nonlinearity of magnetic forces, the moment time histories generally display sinusoidal patterns with plateau-like peaks, which limit the precision of the moment definition. Nonetheless, the consistent magnitude across different scenarios indicates that approxi-

mately 10^7 Nm represents the ideal level of control effort for effective system regulation. This finding aligns with the external wave load moment, which is of the same order, confirming that the control is appropriately scaled to fully counteract the applied loads during the simulation.

Although these moment values are relatively large, they remain reasonable given the scale of the system. Domingos et al. [5] and Ren et al. [31] report that the stiffness of tugger lines used to restrain wind turbine components can generate forces on the order of 10^5 N, potentially producing comparable moment magnitudes depending on the lever arm length and structural displacement. It should be noted that those references pertain to wind turbine blades, whereas this study focuses on a significantly heavier monopile. Taking this scale difference into account, and considering that the proposed control strategy relies exclusively on non-contact magnetic actuation, moments on the order of 10^7 Nm can be considered realistic to mitigate wave loads.

To assess the practical feasibility of the non-contact control strategy, it is essential to consider both the magnetic dipole moment and the resulting magnetic field, as these are the quantities directly manipulated by the PD controller to generate the control moment counteracting the wave forcing.

As previously noted, by assuming a reference dipole moment $m_{c,x} = 1$ Am^2, the controller effectively regulates the product $m_{t,x} \cdot m_{c,x}$, rather than solely acting on the external dipole $m_{t,x}$. This approach allows the magnetic effort to be distributed between the two dipoles, which are considered equivalent in all relevant aspects. Simulations consistently show that the magnetic field varies sinusoidally with the angular displacements θ_1 and θ_2, reaching peak values between 250 mT and 500 mT regardless of submersion depth or magnet positioning along the monopile.

While such field strengths are theoretically achievable with certain magnet types, they would require magnets of extremely large size and special design considerations. Consequently, implementing full control of a heavy monopile in a real-world setting using this approach would be impractical and likely infeasible.

A potential way to reduce the required moments is by selecting an appropriate horizontal distance d that balances the magnetic field and the dipole moment. The results indicate that a larger d lowers the magnetic field, as expected from the inverse cubic relationship between $B_{t,x}$ and the separation r. However, this comes at the cost of requiring excessively high dipole moments, which are impractical to achieve in reality. Therefore, an optimal equilibrium must be identified to maintain reasonably low magnetic fields while keeping the dipole moments within feasible limits.

Furthermore, the magnetic field values observed in this study can be considered as an upper bound, since the simulations were conducted under moderate to high ocean conditions. In the context of offshore monopile installation, operations are typically performed under optimal sea states with low significant wave heights and low wind velocities, which primarily generate short-period waves. Under such milder conditions, the external forcing moment would be smaller, requiring lower magnetic moments to achieve control. Consequently, both the resulting magnetic fields and the required dipole moments would also decrease.

Given that the goal of the installation is precise placement on the seabed—which represents the final stages of the process—full active control is not strictly necessary. Instead, the objective can be to mitigate excessive motion, allowing smaller magnetic fields and dipole moments. In practice, the control system is designed to return the monopile to $x = 0$ m, but a tolerance margin is always allowed. This margin permits the monopile to oscillate during installation as long as it ultimately reaches the correct position on the seabed. Consequently, the magnets do not need to generate maximum moments continuously, enabling intermittent activation and reduced magnetic effort.

This mitigation strategy can exploit the beating phenomenon observed in the time-domain simulations. By activating control when the response is approaching a peak, the system can reduce the amplitude of the oscillation preemptively, minimizing the required magnetic moment. The exact timing could be determined based on a reference oscillation magnitude, chosen according to safety considerations and the capabilities of the magnets.

The main drawback of this approach is that the monopile's oscillations must be carefully monitored and predicted to avoid collisions with the installation vessel. Additionally, the distance between the magnets must always be maintained to prevent excessive interaction, which could induce instability. Overall, this

strategy reduces the required magnetic effort and increases the feasibility of non-contact control while maintaining safe installation conditions.

What number and spatial arrangement of magnets ensure reliable and efficient control performance?

The effectiveness of the magnetic control strategy depends not only on the number of magnets but also on their spatial configuration relative to the monopile. Several key parameters were investigated to determine optimal performance: submersion depth $\mathscr{L}$, the horizontal distance between the external and monopile-mounted dipoles d, and the positioning of magnets along the monopile (L_{x2}, L_x).

The initial performance evaluation to identify the control gains was based on simplified harmonic moment simulations, which quickly revealed the advantages of using two magnets instead of one. The dual-magnet configuration provided superior control over both displacement and angular motions (θ_1 and θ_2), highlighting the limitations of the single-magnet setup, which only acts effectively at one location.

To find the best performing placement, a brute-force parameter sweep was conducted over the monopile length. The first magnet L_x was restricted to the lower half of the monopile ($L_x \in [37\,\text{m}, 62\,\text{m}]$), while the second magnet L_{x2} was placed in the upper half, above the centroid ($L_{x2} \in [2\,\text{m}, 37\,\text{m}]$). Due to the design constraint that magnets must remain above the waterline.

Among all the tested configurations, the setup $(L_{x2}, L_x) = (2, 62)$ m delivered the highest performance. This is attributed to the large moment arm, which allowed for effective control with a lower magnetic dipole moment. However, as this configuration is no longer feasible beyond 10 m submersion, an alternative configuration of $(2, 32)$ m was also evaluated, enabling full control throughout deeper stages of installation, down to $\mathscr{L} = -40$ m.

While both configurations showed similar moment outputs, the $(2, 62)$ m setup required lower magnetic effort, with dipole moments in the order of 10^{10} Am^2 and nearly reaching 10^9 Am^2, compared to higher requirements for the $(2, 32)$ m case. This indicates that the same control performance is achieved with reduced magnetic effort when the magnets are placed closer to the bottom edge along the monopile. Nevertheless, the relatively small performance gap between the two suggests that the $(2, 32)$ m configuration is suitable for complete installation control without requiring a third magnet. That said, the addition of a third magnet could still enhance redundancy and improve response efficiency in early stages.

Another important design variable examined was the horizontal distance d between the external magnets and the monopile mounted ones. Two complementary approaches were used to study its effect: evaluating different values of d for a fixed configuration $(2, 32)$ m across various submersion depths, and analyzing the response across multiple L_x values at a fixed submersion depth of $\mathscr{L} = -10$ m.

In both cases, increasing d led to a decrease in control performance. However, the overall effectiveness of the controller was maintained across all tested distances, with maximum horizontal displacements remaining around 0.5 m even at $d = 1$ m. Despite d not being an explicit parameter in the PD control law, the dipole moment required by the controller increased sharply with distance. This is explained by the strong dependence of the magnetic moment on the dipole separation r, which grows with d. Since magnetic moment scales with $1/r^4$, the controller compensates for larger separations by substantially increasing $m_{t,x}$. This reveals a key trade-off: small d values yield low dipole moments but produce extremely strong magnetic fields, often beyond what magnets of such size can realistically generate. Conversely, at larger d, the magnetic field strength becomes more realistic, but the required dipole moments reach impractically high levels. Thus, an optimal intermediate d must be chosen to keep both the dipole moment and magnetic field within feasible limits.

Moment magnitudes remained nearly constant across different d values, indicating that variations in d primarily affect actuation effort rather than force output. However, moment time histories revealed that lower d values (0.25 m and 0.5 m) result in more irregular, plateau-like behaviors, reflecting nonlinearities in the magnetic interaction. In contrast, higher distances yield smoother moment curves but at the cost of greater actuation effort.

Interestingly, the influence of submersion depth becomes more pronounced at larger d. At $d = 1$ m, the required dipole moment nearly doubles when comparing $\mathscr{L} = -10$ m and $\mathscr{L} = -40$ m. Conversely, when magnets are closer together, the required magnetic effort becomes less sensitive to submersion depth, although nonlinearity issues become more prominent.

Practical considerations also play a crucial role in determining an appropriate value of d. In real-world applications, smaller distances between magnets can increase the risk of physical interference or unstable magnetic interactions, effects that are not captured by the idealized dipole-dipole model. In addition, d must be selected with safety in mind to prevent collisions with the installation vessel or other components during the process.

In conclusion, the tested configurations show that reliable and efficient magnetic control is possible. The best-performing setup uses two strategically placed magnets at $(L_{x2}, L_x) = (2, 32)$ m with a horizontal spacing of $d = 0.5$ m. This arrangement achieves strong performance across all submersion stages while providing the best compromise between magnetic field intensity and dipole moment requirements, reducing the risk of excessive nonlinearity or magnetic instabilities compared to other tested configurations. While the required magnetic fields and dipole moments exceed the capabilities of current magnetic actuation technologies, they provide a valuable benchmark for understanding the scale of effort needed to stabilize such a highly dynamic system. Therefore, the results of this work should be regarded as an idealized performance reference for PD-based non-contact control, rather than a directly implementable solution.

5.2. Discussion and Recommendations

This research introduced a non-contact magnetic control strategy for a double pendulum system representing the progressive submersion of a monopile during offshore installation. A simplified PD controller was implemented using fixed permanent magnets, offering a practical approach that avoids reliance on active electromagnets.

Several improvements are recommended to enhance the model's realism and control performance. First, the hydrodynamic loading could be more accurately modeled by incorporating diffraction theory instead of relying solely on the Morison equation, especially for larger-diameter monopiles. Moreover, the use of electromagnets would allow for active control of the magnetic force by varying the input voltage. This would require formulating a new control equation and considering the physical limitations of electromagnets, such as saturation effects, which could significantly influence the control response and feasibility.

Further development should also focus on the dynamic analysis of the control system. Linearizing the equations of motion could help identify regions of potential instability, particularly as functions of the controller gains K_p and K_d. Moreover, introducing vessel motion through the monopile tip or vessel coupling could reveal additional challenges. Adding a third rotational degree of freedom to the system would provide a more complete representation of the dynamics involved during installation or operation in rough sea states.

Another promising future extension of this work would be to investigate ferromagnetic interaction with the steel monopile. This would eliminate the need to pre-install permanent magnets on the monopile, a process that is costly, time-consuming, and may complicate logistics during offshore preparation. A ferromagnetic approach could therefore offer a simpler, more scalable, and cost-effective solution.

It is acknowledged that validation of the results was not possible within this work, as no physical experiments were conducted. Experimental testing will be essential in future studies to assess the feasibility and effectiveness of the proposed control strategies under real environmental conditions. Furthermore, the present results focus on full control, which leads to magnetic requirements that exceed the capabilities of current magnet technologies but can serve as valuable reference results. Building on these insights, future research could explore mitigation strategies that activate only during critical events, reducing magnetic demands and making practical implementation more achievable.

Despite these limitations, the study presents a comprehensive framework for exploring non-contact control in offshore applications. The results demonstrate that such control strategies can be effective

even in dynamically complex scenarios involving wave loading and submersion effects. Overall, this research provides a promising starting point for the development of a magnetic control systems for offshore structural components.

References

[1] M. Bilgili and H. Alphan. *Global growth in ofshore wind turbine technology*. 2021. URL: https://doi.org/10.1007/s10098-022-02314-0.

[2] Wind Europe. *Wind energy today*. 2025. URL: https://windeurope.org/about-wind/wind-energy-today/.

[3] David Fidalgo Domingos, Peter Wellens, and Jan-Willem van Wingerden. "Frequency-domain framework for floating installation of wind-turbine towers". In: *Ocean Engineering* 297 (2024). ISSN: 0029-8018. DOI: https://doi.org/10.1016/j.oceaneng.2024.116952. URL: https://www.sciencedirect.com/science/article/pii/S0029801824002890.

[4] European Commission. *The European Green Deal - A growth strategy that protects the climate*. 2025. URL: https://ec.europa.eu/stories/european-green-deal/.

[5] D. F. Domingos et al. *Full-scale measurements and analysis of the floating installation of an offshore wind turbine tower*. 2024. URL: https://www.sciencedirect.com/science/article/pii/S0029801824020080?ref=pdf_download&fr=RR-2&rr=8f0e377a391e28af.

[6] Zhiyu Jiang. *Installation of offshore wind turbines: A technical review*. 2021. URL: https://www.sciencedirect.com/science/article/pii/S1364032120308601?ref=pdf_download&fr=RR-2&rr=8f296aaa8bf0b7b2.

[7] Lin Li. *Dynamic Analysis of the Installation of Monopiles for Offshore Wind Turbines*. 2016. URL: https://ntnuopen.ntnu.no/ntnu-xmlui/handle/11250/2391743.

[8] Zhiqiang Ren et al. "Active tugger line force control for single blade installation". In: *Wind Energy* 21.12 (2018), pp. 1344–1358. DOI: 10.1002/we.2258.

[9] Shenghai Wang et al. "Dynamic modelling and analysis of 3-axis motion compensated offshore cranes". In: *Ships and Offshore Structures* 13.3 (2018). URL: https://doi.org/10.1080/17445302.2017.1360981.

[10] Dong-Hyun Lee et al. "A study on load position control and vibration attenuation in crane operation using sub-actuator". In: *Measurement and Control* 52.7-8 (2019). DOI: 10.1177/0020294019847703.

[11] P. Atzampou et al. *Contactless control of suspended loads for offshore installations: Proof of concept using magnetic interaction*. 2024. URL: https://pure.tudelft.nl/ws/portalfiles/portal/176504441/1-s2.0-S0022460X24000105-main.pdf.

[12] H. Hersbach et al. *ERA5 hourly data on single levels from 1940 to present*. Accessed on 05-2025. 2023. DOI: 10.24381/cds.adbb2d47. URL: https://doi.org/10.24381/cds.adbb2d47.

[13] Ju-Hwan Cha, Myung-Il Roh, and Kyu-Yeul Lee. "Dynamic response simulation of a heavy cargo suspended by a floating crane based on multibody system dynamics". In: *Ocean Engineering* 37.14 (2010), pp. 1273–1291. ISSN: 0029-8018. DOI: https://doi.org/10.1016/j.oceaneng.2010.06.008. URL: https://www.sciencedirect.com/science/article/pii/S0029801810001423.

[14] Kenneth S. Krane. "The Pendulum: A Case Study in Physics". In: *Physics Today* 59.7 (July 2006), pp. 52–53. ISSN: 0031-9228. DOI: 10.1063/1.2337835. URL: https://doi.org/10.1063/1.2337835.

[15] P. van der Male and P.C. Meijers. *TU Delft Course CIEM 5220- Dynamics of structures subjected to wind and waves*. 2024.

[16] J.M.J. Journée and W.W. Massie. *Offshore Hydromechanics*. TU Delft, 2001.

[17] Klaus Hasselmann et al. "Measurements of wind-wave growth and swell decay during the Joint North Sea Wave Project (JONSWAP)". In: *Deut. Hydrogr. Z.* 8 (Jan. 1973).

[18] L. Li, Z. Gao, and T. Moan. *Numerical simulations for installation of offshore wind turbine monopiles using floating vessels*. 2013. URL: https://doi.org/10.1115/OMAE2013-11200.

[19] John Morison et al. “The Force Exerted by Surface Waves on Piles”. In: *Journal of Petroleum Technology* 2 (1950), pp. 149–154. URL: https://api.semanticscholar.org/CorpusID:110216127.

[20] J. N. Newman. *Marine Hydrodynamics*. The MIT Press, Aug. 1977. ISBN: 9780262280617. DOI: 10.7551/mitpress/4443.001.0001. URL: https://doi.org/10.7551/mitpress/4443.001.0001.

[21] L.B. Zhang et al. “Design and experimental analysis of broadband energy harvesting from vortex-induced vibrations”. In: *Journal of Sound and Vibration* 408 (2017), pp. 210–219. ISSN: 0022-460X. DOI: https://doi.org/10.1016/j.jsv.2017.07.029. URL: https://www.sciencedirect.com/science/article/pii/S0022460X17305655.

[22] Tobias Greve Larsen, Zili Zhang, and Jan Høgsberg. “Vibration damping of an offshore wind turbine by optimally calibrated pendulum absorber with shunted electromagnetic transducer”. In: *Journal of Sound and Vibration* 505 (2021). ISSN: 0022-460X. DOI: https://doi.org/10.1016/j.jsv.2021.116144. URL: https://www.sciencedirect.com/science/article/pii/S0022460X21002169.

[23] B.P. Mann. “Energy criterion for potential well escapes in a bistable magnetic pendulum”. In: *Journal of Sound and Vibration* 323.3 (2009). ISSN: 0022-460X. DOI: https://doi.org/10.1016/j.jsv.2009.01.012. URL: https://www.sciencedirect.com/science/article/pii/S0022460X09000121.

[24] Kelly Austin and J. Wagner. “Development of an electromagnet excited mass-pendulum system modeling and control laboratory experiment — Theory and test”. In: July 2013. DOI: 10.23919/ECC.2013.6669112.

[25] Nathan Ida. “Design and control of a magnetic pendulum actuator”. In: *2012 13th International Conference on Optimization of Electrical and Electronic Equipment (OPTIM)*. 2012. DOI: 10.1109/OPTIM.2012.6231898.

[26] Peter B. Landecker, Daniel D. Villani, and Kar W. Yung. “An Analytic Solution for the Torque Between Two Magnetic Dipoles”. In: *Physical Separation in Science and Engineering* 10.1 (1999). DOI: https://doi.org/10.1155/1999/97902. URL: https://onlinelibrary.wiley.com/doi/abs/10.1155/1999/97902.

[27] D. j. Griffiths. *Introduction to Electrodynamics*. Prentice Hall, Sept. 1999. ISBN: 013805326X. URL: https://archive.org/details/davidgriffithselectrodynamics/page/n1/mode/2up?view=theater&ui=embed&wrapper=false.

[28] Åström et al. *Feedback Systems - An Introduction for Scientists and Engineers*. 2021. URL: https://app.knovel.com/hotlink/khtml/id:kt013MTPK1/feedback-systems-an-introduction/simple-controllers-complex.

[29] VM. Sandeep. *When and why to use P, PI, PD and PID Controller?* 2021. URL: https://medium.com/@svm161265/when-and-why-to-use-p-pi-pd-and-pid-controller-73729a708bb5.

[30] Linda Petzold. “Automatic Selection of Methods for Solving Stiff and Nonstiff Systems of Ordinary Differential Equations”. In: *SIAM Journal on Scientific and Statistical Computing* 4.1 (1983), pp. 136–148. DOI: 10.1137/0904010. URL: https://doi.org/10.1137/0904010.

[31] Zhengru Ren et al. “Active tugger line force control for single blade installation”. In: *Wind Energy* (Aug. 2018). DOI: 10.1002/we.2258.

A

Appendix A

A.1. Extended Energy Formulation

This section presents the complete derivation of the kinetic energy T and potential energy U introduced in Equations 3.8 and 3.9. The formulation builds upon the principles outlined in Chapter 3.1.1.

By substituting the relevant components, the expressions for both the rod and the hollow cylinder are derived in detail.

The kinetic energy of the rod is obtained as:

$$T_{rod} = \frac{1}{2}\left(\frac{ml^2}{3}\right)\dot{\theta_1}^2 = \frac{1}{6}ml^2\dot{\theta_1}^2 \tag{A.1}$$

The kinetic energy of the hollow cylinder is expressed as:

$$\begin{aligned} T_{cyl} &= \frac{1}{2}M\left(\frac{L^2}{4}\dot{\theta_2}^2\left(\cos^2(\theta_2)+\sin^2(\theta_2)\right) + l^2\dot{\theta_1}^2\left(\cos^2(\theta_1)+\sin^2(\theta_1)\right) + lL\dot{\theta}_1\dot{\theta}_2\left(\cos(\theta_1)\cos(\theta_2)+\sin(\theta_1)\sin(\theta_2)\right)\right) \\ &\quad + \frac{1}{2}\left(\frac{MR^2}{2}+\frac{ML^2}{12}\right)\dot{\theta_2}^2 \\ &= \frac{1}{2}M\left(\frac{L^2}{4}\dot{\theta_2}^2 + l^2\dot{\theta_1}^2 + lL\dot{\theta}_1\dot{\theta}_2\cos(\theta_1-\theta_2)\right) + \frac{1}{2}\left(\frac{MR^2}{2}+\frac{ML^2}{12}\right)\dot{\theta_2}^2 \\ &= \frac{1}{2}Ml^2\dot{\theta_1}^2 + \frac{1}{2}MlL\dot{\theta}_1\dot{\theta}_2\cos(\theta_1-\theta_2) + \frac{1}{2}M\left(\frac{R^2}{2}+\frac{L^2}{3}\right)\dot{\theta_2}^2 \end{aligned} \tag{A.2}$$

For simplifying T_{cyl} the trigonometric identities $\cos^2\alpha+\sin^2\alpha = 1$ and $\cos\alpha\cos\beta+\sin\alpha\sin\beta = \cos(\alpha-\beta)$ are used.

For the potential energy, the vertical displacement of the center of mass of each component is considered. For the rod:

$$U_{rod} = mg\left(-\frac{l}{2}\cos(\theta_1)\right)\ , \tag{A.3}$$

while for the hollow cylinder:

$$U_{cyl} = Mg\left(-\frac{L}{2}\cos(\theta_2) - l\cos(\theta_1)\right)\ . \tag{A.4}$$

By summing the contributions of the two components, the total kinetic energy T and potential energy U of the system are obtained, providing a complete energy formulation consistent with the dynamics of the double pendulum system under consideration.

A.2. Lagrange derivation of Non Linear Equations of Motion

Given the expressions for the kinetic and potential energy of the system, the equations of motion of the non-linear double pendulum can be derived by applying the Lagrangian formulation using Equations 3.16 and 3.17.

The Lagrangian L of the system resulted in:

$$\begin{aligned} L = &\left(\frac{1}{6}ml^2 + \frac{1}{2}Ml^2\right)\dot{\theta_1}^2 + \frac{1}{2}MlL\dot{\theta_1}\dot{\theta_2}\cos(\theta_1 - \theta_2) \\ &+ \frac{1}{2}M\left(\frac{R^2}{2} + \frac{L^2}{3}\right)\dot{\theta_2}^2 + \left(\frac{m}{2} + M\right)lg\cos(\theta_1) + \frac{M}{2}Lg\cos(\theta_2) \end{aligned} \tag{A.5}$$

Then, knowing L, the each term of the Euler-Lagrange equation can be derived for each of the generalized coordinates θ_1 and θ_2.

$$\frac{d}{dt}\left(\frac{\partial L}{\partial \dot{\theta_i}}\right) - \frac{\partial L}{\partial \theta_i} = 0 \quad \text{for } i = 1, 2\ . \tag{A.6}$$

Euler-Lagrange equation solved for θ_1

The Euler–Lagrange equation for the generalized coordinate θ_1 is derived by first computing the partial derivative of the Lagrangian with respect to $\dot{\theta_1}$, followed by taking its total time derivative. The first term is obtained as:

$$\frac{\partial L}{\partial \dot{\theta_1}} = \left(\frac{1}{3}ml^2 + Ml^2\right)\dot{\theta_1} + \frac{1}{2}MlL\dot{\theta_2}\cos(\theta_1 - \theta_2)$$

$$\frac{d}{dt}\left(\frac{\partial L}{\partial \dot{\theta_1}}\right) = \left(\frac{1}{3}ml^2 + Ml^2\right)\ddot{\theta_1} + \frac{1}{2}MlL\ddot{\theta_2}\cos(\theta_1 - \theta_2) - \frac{1}{2}MlL\dot{\theta_2}\sin(\theta_1 - \theta_2)(\dot{\theta_1} - \dot{\theta_2})$$

For the second term, the partial derivative with respect to θ_1 is computed:

$$\frac{\partial L}{\partial \theta_1} = -\frac{1}{2}MlL\dot{\theta_1}\dot{\theta_2}\sin(\theta_1 - \theta_2) - \left(\frac{m}{2} + M\right)lg\sin(\theta_1)$$

Substituting both the terms into the Euler–Lagrange equation leads to the first nonlinear equation of motion:

$$\left(\frac{1}{3}m + M\right)l^2\ddot{\theta_1} + \frac{1}{2}MlL\ddot{\theta_2}\cos(\theta_1 - \theta_2) + \frac{1}{2}MlL\dot{\theta_2}^2\sin(\theta_1 - \theta_2) + \left(\frac{m}{2} + M\right)lg\sin(\theta_1) = 0$$

Euler-Lagrange equation solved for θ_2

Similarly, the Euler–Lagrange equation for the generalized coordinate θ_2 is derived by first computing the partial derivative of the Lagrangian with respect to $\dot{\theta_2}$, followed by taking its total time derivative. Then, the first term reads:

$$\frac{\partial L}{\partial \dot{\theta_2}} = \frac{1}{2}MlL\dot{\theta_1}\cos(\theta_1 - \theta_2) + M\left(\frac{R^2}{2} + \frac{L^2}{3}\right)\dot{\theta_2}$$

$$\frac{d}{dt}\left(\frac{\partial L}{\partial \dot{\theta_2}}\right) = \frac{1}{2}MlL\ddot{\theta_1}\cos(\theta_1-\theta_2) - \frac{1}{2}MlL\dot{\theta_1}\sin(\theta_1-\theta_2)(\dot{\theta_1}-\dot{\theta_2}) + M\left(\frac{R^2}{2}+\frac{L^2}{3}\right)\ddot{\theta_2}$$

For the second term, the partial derivative with respect to θ_2 is computed:

$$\frac{\partial L}{\partial \theta_2} = \frac{1}{2}MlL\dot{\theta_1}\dot{\theta_2}\sin(\theta_1-\theta_2) - \frac{1}{2}MLg\sin(\theta_2)$$

Substituting the new derived terms into the Euler–Lagrange equation leads to the second nonlinear equation of motion:

$$\frac{1}{2}MlL\ddot{\theta_1}\cos(\theta_1-\theta_2) + M\left(\frac{R^2}{2}+\frac{L^2}{3}\right)\ddot{\theta_2} - \frac{1}{2}MlL\dot{\theta_1}^2\sin(\theta_1-\theta_2) + \frac{1}{2}MLg\sin(\theta_2) = 0$$

Final Form of the Non-linear Equations of Motion

Collecting both equations, the non-linear equations of motion of the double pendulum described in Chapter 3 are expressed as:

$$\begin{cases} \left(\frac{m}{3}+M\right)l^2\ddot{\theta_1} + \frac{1}{2}MlL\ddot{\theta_2}\cos(\theta_1-\theta_2) + \frac{1}{2}MlL\dot{\theta_2}^2\sin(\theta_1-\theta_2) + \left(\frac{m}{2}+M\right)lg\sin(\theta_1) = 0 \\ \frac{1}{2}MlL\ddot{\theta_1}\cos(\theta_1-\theta_2) + M\left(\frac{R^2}{2}+\frac{L^2}{3}\right)\ddot{\theta_2} - \frac{1}{2}MlL\dot{\theta_1}^2\sin(\theta_1-\theta_2) + \frac{1}{2}MLg\sin(\theta_2) = 0 \end{cases}$$

A.3. Lagrange derivation of Linear Equations of Motion

In order to linearize the equations of motion, as mentioned in Chapter 2.1, it is possible to exploit the small angle approximation.

$$\sin(\theta) \approx \theta \quad , \quad \cos(\theta) \approx 1 - \frac{\theta^2}{2} \tag{A.7}$$

The coordinates that describe the motion of the double pendulum can be simplified as follow:

$$P_m(t) = \begin{bmatrix} \frac{l}{2}\theta_1 \\ -\left(\frac{l}{2} - \frac{l}{4}\theta_1^2\right) \end{bmatrix}, \qquad P_M(t) = \begin{bmatrix} \frac{L}{2}\theta_2 + l\theta_1 \\ -\left(\frac{L}{2} + l - \frac{L}{4}\theta_2^2 - \frac{l}{2}\theta_1^2\right) \end{bmatrix}. \tag{A.8}$$

Resulting in the following velocities:

$$v_{G_1}(t) = \begin{bmatrix} \frac{l}{2}\dot{\theta}_1 \\ \frac{l}{2}\theta_1\dot{\theta}_1 \end{bmatrix}, \qquad v_{G_2}(t) = \begin{bmatrix} \frac{L}{2}\dot{\theta}_2 + l\dot{\theta}_1 \\ \frac{L}{2}\theta_2\dot{\theta}_2 + l\theta_1\dot{\theta}_1 \end{bmatrix}. \tag{A.9}$$

Since the kinetic energy of the cable do not include the velocity term, it remains unchanged. On the other hand the cylinder new kinetic energy is presented below:

$$T_{rod} = \frac{1}{2}\frac{ml^2}{3}\dot{\theta}_1^2 = \frac{m}{6}l^2\dot{\theta}_1^2 \tag{A.10}$$

$$
\begin{aligned}
T_{cyl} &= \frac{1}{2}M\Big(\frac{L^2}{4}\dot{\theta}_2^2 + l^2\dot{\theta}_1^2 + Ll\dot{\theta}_2\dot{\theta}_1 + \frac{L^2}{4}\theta_2^2\dot{\theta}_2^2 + l^2\theta_1^2\dot{\theta}_1^2 + Ll\theta_2\theta_1\dot{\theta}_2\dot{\theta}_1\Big) \\
&\quad + \frac{1}{2}\left(\frac{MR^2}{2} + \frac{ML^2}{12}\right)\dot{\theta}_2^2 \\
&= \frac{1}{2}M\left(\frac{L^2}{4} + \frac{L^2}{4}\theta_2^2\right)\dot{\theta}_2^2 + \frac{1}{2}M\left(l^2 + l^2\theta_1^2\right)\dot{\theta}_1^2 + \frac{1}{2}M\left(Ll + Ll\theta_1\theta_2\right)\dot{\theta}_1\dot{\theta}_2 \\
&\quad + \frac{1}{2}M\left(\frac{R^2}{2} + \frac{L^2}{12}\right)\dot{\theta}_2^2 \\
&\approx \frac{1}{2}M\left(\frac{R^2}{2} + \frac{L^2}{3}\right)\dot{\theta}_2^2 + \frac{1}{2}Ml^2\dot{\theta}_1^2 + \frac{1}{2}MLl\dot{\theta}_1\dot{\theta}_2
\end{aligned}
\tag{A.11}
$$

The terms $\theta_1^2\dot{\theta}_1^2$, $\theta_2^2\dot{\theta}_2^2$, and $\theta_1\dot{\theta}_1\theta_2\dot{\theta}_2$ are of fourth order. Hence, under the small-angle assumption, they can be neglected as they have a minimal effect on the system dynamics.

Thus, by summing the components, the total kinetic energy of the system is:

$$
T = \frac{ml^2}{6}\dot{\theta}_1^2 + \frac{1}{2}M\left(\frac{R^2}{2} + \frac{L^2}{3}\right)\dot{\theta}_2^2 + \frac{1}{2}Ml^2\dot{\theta}_1^2 + \frac{1}{2}MLl\dot{\theta}_1\dot{\theta}_2
$$

From $P_{m,z}$ and $P_{M,z}$ components of the moving vectors, the potential energy can be calculated:

$$
U_{rod} = -mg(\frac{l}{2} - \frac{l}{4}\theta_1^2)
$$

$$
U_{cyl} = -Mg(\frac{L}{2} + l - \frac{L}{4}\theta_2^2 - \frac{l}{2}\theta_1^2)
$$

Therefore, the resulting total potential energy is:

$$
U = mg\frac{l}{4}\theta_1^2 + Mg\frac{l}{2}\theta_1^2 + Mg\frac{L}{4}\theta_2^2 + constant
$$

Having derived the new equations for the energy in the linear case, the Lagrangian becomes:

$$
L = \left(\frac{ml^2}{6} + \frac{1}{2}Ml^2\right)\dot{\theta}_1^2 + \frac{1}{2}M\left(\frac{R^2}{2} + \frac{L^2}{3}\right)\dot{\theta}_2^2 + \frac{1}{2}MLl\dot{\theta}_1\dot{\theta}_2 - mg\frac{l}{4}\theta_1^2 - Mg\frac{l}{2}\theta_1^2 - Mg\frac{L}{4}\theta_2^2 + \text{constant}
\tag{A.12}
$$

Using the Euler-Lagrange equation for the generalized coordinates θ_i, the Linear equations of motion are obtained.

Euler-Lagrange equation solved for θ_1

The Euler–Lagrange equation for the generalized coordinate θ_1 is derived by first computing the partial derivative of the Lagrangian with respect to $\dot{\theta_1}$, followed by taking its total time derivative. The first term is obtained as:

$$
\frac{\partial L}{\partial \dot{\theta}_1} = \left(\frac{ml^2}{3} + Ml^2\right)\dot{\theta}_1 + \frac{1}{2}MLl\dot{\theta}_2
\tag{A.13}
$$

$$
\frac{d}{dt}\left(\frac{\partial L}{\partial \dot{\theta}_1}\right) = \left(\frac{ml^2}{3} + Ml^2\right)\ddot{\theta}_1 + \frac{1}{2}MLl\ddot{\theta}_2
\tag{A.14}
$$

For the second term, the partial derivative with respect to θ_1 is computed:

$$\frac{\partial L}{\partial \theta_1} = -\left(mg\frac{l}{2} + Mgl\right)\theta_1 \tag{A.15}$$

Substituting both the terms into the Euler–Lagrange equation leads to the first linear equation of motion:

$$\left(\frac{m}{3} + M\right) l^2\ddot{\theta}_1 + \frac{1}{2}MLl\ddot{\theta}_2 + \left(\frac{m}{2} + M\right) gl\theta_1 = 0 \tag{A.16}$$

Euler-Lagrange equation solved for θ_2

Similarly, the Euler–Lagrange equation for the generalized coordinate θ_2 is derived by first computing the partial derivative of the Lagrangian with respect to $\dot{\theta}_2$, followed by taking its total time derivative. Then, the first term reads:

$$\frac{\partial L}{\partial \dot{\theta}_2} = \frac{1}{2}MLl\dot{\theta}_1 + M\left(\frac{R^2}{2} + \frac{L^2}{3}\right)\dot{\theta}_2 \tag{A.17}$$

$$\frac{d}{dt}\left(\frac{\partial L}{\partial \dot{\theta}_2}\right) = \frac{1}{2}MLl\ddot{\theta}_1 + M\left(\frac{R^2}{2} + \frac{L^2}{3}\right)\ddot{\theta}_2 \tag{A.18}$$

For the second term, the partial derivative with respect to θ_2 is computed:

$$\frac{\partial L}{\partial \theta_2} = -Mg\frac{L}{2}\theta_2 \tag{A.19}$$

Substituting the new derived terms into the Euler–Lagrange equation leads to the second linear equation of motion:

$$\frac{1}{2}MLl\ddot{\theta}_1 + M\left(\frac{R^2}{2} + \frac{L^2}{3}\right)\ddot{\theta}_2 + Mg\frac{L}{2}\theta_2 = 0 \tag{A.20}$$

Final Form of the Linear Equations of Motion

Collecting both equations, the linear equations of motion of the double pendulum described in Chapter 3 are expressed as:

$$\begin{cases} \left(\frac{m}{3} + M\right) l^2\ddot{\theta}_1 + \frac{1}{2}MLl\ddot{\theta}_2 + \left(\frac{m}{2} + M\right) gl\theta_1 = 0 \\ \frac{1}{2}MLl\ddot{\theta}_1 + M\left(\frac{R^2}{2} + \frac{L^2}{2}\right)\ddot{\theta}_2 + Mg\frac{L}{2}\theta_2 = 0 \end{cases}$$

B

Appendix B

B.1. JONSWAP Spectrum Alternative Derivation

An alternative approach for determining the wave parameters relevant to the selected site, as presented in Tab.3.2, involves using the mean wave period T_s.

Similarly to the procedure followed in Chapter 3.2 for U_{10}, the monthly extreme values are extracted from the time series of the mean wave period, shown in Fig. B.1. The mean of these extreme values is then computed, yielding a representative estimate of the monthly maximum mean wave period:

$$T_s = 7.46\,\text{s} \tag{B.1}$$

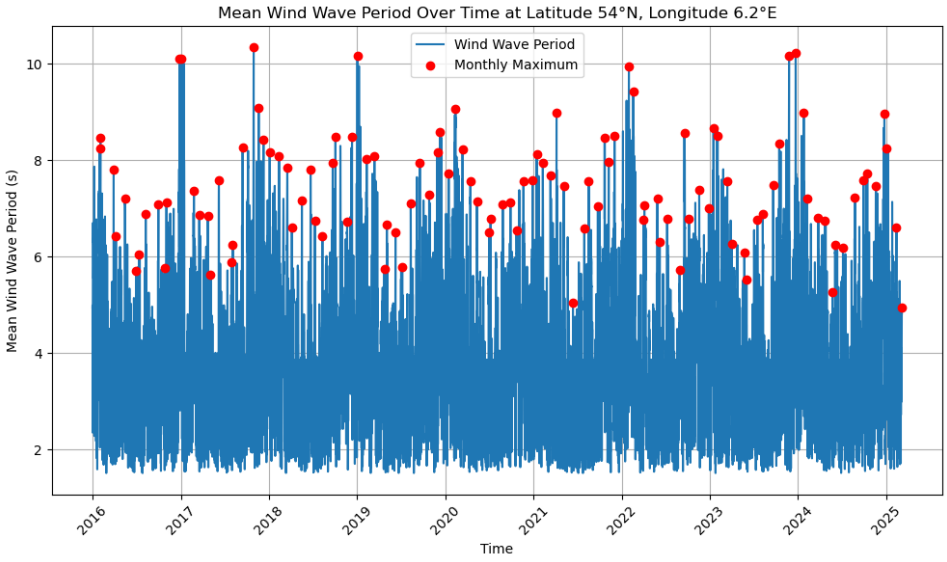

Figure B.1: Mean wave period time series in the North Sea

From this value, the peak frequency of the spectrum can be calculated using the relation $f_p = 1/T_s$. Once f_p is known, the wind speed at 10 meters height, U_{10}, can be determined via Equation 2.13. Subsequently, all other necessary parameters can be derived, as summarized in Table B.1.

H_s (m)	T_p (s)	f_p (Hz)	U_{10} (m/s)	F (km)
2.3	7.46	0.134	11.42	150

Table B.1: Input Parameter for JONSWAP spectrum based on T_s

The values presented in Table B.1 are consistent with those introduced in Chapter 3.2, confirming that the input parameters are representative for the conditions considered.

Appendix C

C.1. State-Space Formulation and Eigenvalue Analysis

The state-space from method is particularly useful when a damping term is added to the system introducing a first derivative of the unknowns in the equations making the modal analysis method not applicable.

To express the system in state-space form, we define the state vector as:

$$X = \begin{bmatrix} y_1 \\ y_2 \\ x_1 \\ x_2 \end{bmatrix}, \quad \text{where} \quad \begin{cases} y_1 &= \theta_1 \\ y_2 &= \theta_2 \\ x_1 &= \dot{\theta}_1 \\ x_2 &= \dot{\theta}_2 \end{cases}. \tag{C.1}$$

The system of equations governing the motion can then be formulated as:

$$\begin{cases} \dot{y}_1 = x_1 \\ \dot{y}_2 = x_2 \\ \left(\frac{m}{3} + M\right) l^2 \dot{x}_1 + \frac{1}{2} MLl\dot{x}_2 + \left(\frac{m}{2} + M\right) l\, g\, y_1 = 0 \\ M\left(\frac{R^2}{2} + \frac{L^2}{3}\right) \dot{x}_2 + \frac{1}{2} MLl\dot{x}_1 + \frac{1}{2} ML\, g\, y_2 = 0 \end{cases} \tag{C.2}$$

Rewriting the system in matrix form:

$$\dot{X} = AX \tag{C.3}$$

The state matrix A is defined as:

$$A = \begin{bmatrix} 0 & \mathbf{I} \\ -\mathbf{M}^{-1}\mathbf{K} & 0 \end{bmatrix} \tag{C.4}$$

where:

$$\mathbf{M} = \begin{bmatrix} \left(\frac{m}{3} + M\right) l & \frac{1}{2}MLl \\ \frac{1}{2}MLl & M\left(\frac{R^2}{2} + \frac{L^2}{3}\right) \end{bmatrix}, \quad \mathbf{K} \quad = \begin{bmatrix} \left(\frac{m}{2} + M\right) lg & 0 \\ 0 & \frac{1}{2}MLg \end{bmatrix}, \quad \mathbf{I} = \begin{bmatrix} 1 & 0 \\ 0 & 1 \end{bmatrix}. \tag{C.5}$$

By looking at determinant of the state matrix A it is possible to obtain the eigenvalues of the system.

$$\det(A - \lambda \mathbf{I}) = 0, \quad \text{where} \quad \lambda = \text{eigenvalues} \tag{C.6}$$

In undamped systems the eigenvalues λ of A are typically imaginary numbers and Equation C.7 represents the natural frequencies in Hz.

$$\omega = Im(\frac{\lambda}{2\pi}) \tag{C.7}$$

Using the values of Table 3.1, the following A matrix is obtained:

$$A = \begin{bmatrix} 0 & 0 & 1 & 0 \\ 0 & 0 & 0 & 1 \\ -0.48883984 & 0.36614277 & 0 & 0 \\ 0.79201033 & -0.79189357 & 0 & 0 \end{bmatrix}$$

Using Equation C.7, the eigenvalues can be calculated.

$$\lambda = \begin{bmatrix} -5.3283667 \times 10^{-18} + 0.17432991i \\ -5.3283667 \times 10^{-18} - 0.17432991i \\ 0 + 0.04528176i \\ 0 - 0.04528176i \end{bmatrix}$$

Since no damping is included in the system, the eigenvalues are expected to be purely imaginary, with zero real part Re. Although a small real component appears for two of the eigenvalues, it is negligibly close to zero, confirming that the solution is consistent with theoretical expectations. Looking at the Im part, the natural frequencies are obtained and reported in Table C.1. The results are consistent with those obtained in Chapter 3.4.1 with the Modal analysis method.

Table C.1: Natural frequencies of the double pendulum system using state-space form

Modes Natural Frequency	Hz	rad/s
Mode 1	0.045	0.284
Mode 2	0.174	1.095